UNIVERSITY OF CALIFORNIA, SAN DIEGO

Wind and tidal response of a semi-enclosed bay, Bahía Concepción, Baja California

A dissertation submitted in partial satisfaction of the
requirements for the degree Doctor of Philosophy
in
Oceanography

by

Aurélien L. S. Ponte

Committee in charge:

Professor Clinton D. Winant, Chair
Professor Myrl C. Hendershott, Co-chair
Professor Stefan G. Llewellyn Smith
Professor Mark D. Ohman
Professor Kraig B. Winters

2009

The dissertation of Aurélien L. S. Ponte is approved, and it is acceptable in quality and form for publication on microfilm:

Co-chair

Chair

University of California, San Diego

2009

For my love Delphine, my parents Karin and Claudio, my sister Jennifer and my brother Jonathan.

TEBALDEO. Les nations paisibles et heureuses ont quelquefois brillé d'une clarté pure, mais faible. Il y a plusieurs cordes à la harpe des anges ; le zéphyr peut murmurer sur les plus faibles, et tirer de leur accord une harmonie suave et délicieuse; mais la corde d'argent ne s'ébranle qu'au passage du vent du nord. C'est la plus belle et la plus noble et cependant le toucher d'une rude main lui est favorable. L'enthousiasme est frère de la souffrance.

LORENZO. C'est-à-dire qu'un peuple malheureux fait les grands artistes. Je me ferai volontiers l'alchimiste de ton alambic; les larmes des peuples y retombent en perles. Par la mort du diable, tu me plais. Les familles peuvent se désoler, les nations mourir de misère, cela échauffe la cervelle de monsieur. Admirable poète !

— Alfred de Musset, *Lorenzaccio*

TABLE OF CONTENTS

Signature Page . . . iii

Dedication . . . iv

Epigraph . . . v

Table of Contents . . . vi

List of Figures . . . ix

List of Tables . . . xi

Acknowledgments . . . xii

Vita, Publications, and Fields of Study . . . xiii

Abstract . . . xiv

1 **Introduction** . . . 1
- 1.1 Introduction . . . 1
- 1.2 Observations . . . 3
  - 1.2.1 Bahía Concepción . . . 3
  - 1.2.2 Instrumentation . . . 5
  - 1.2.3 Climatological conditions, forcings . . . 7
  - 1.2.4 Overview of observed current fluctuations . . . 11
- 1.3 Overview . . . 12

2 **Theoretical wind driven circulation in an elongated basin** . . . 16
- 2.1 Introduction . . . 16
- 2.2 The model . . . 19
  - 2.2.1 Formulation . . . 19
  - 2.2.2 Elongated basins . . . 23
  - 2.2.3 Parameters and basin choice . . . 24
- 2.3 Sea level and transports . . . 25
  - 2.3.1 Sub-inertial response: $\sigma < 1$ . . . 25
  - 2.3.2 Inertial and super-inertial response: $\sigma \geq 1$ . . . 28
  - 2.3.3 Asymptotic expansion in α . . . 30
- 2.4 Three-dimensional velocities . . . 30
  - 2.4.1 Frequency response . . . 30
  - 2.4.2 Selected frequencies . . . 33
- 2.5 Discussion . . . 36
  - 2.5.1 Higher friction: $\delta_E \geq 1$ . . . 36

2.5.2 $\delta_E \ll 1$, $\sigma \ll 1$: link to quasi-geostrophy 38
2.5.3 Spinup 39
2.5.4 Semi-enclosed versus closed basins 41
2.6 Summary and conclusions 42
2.7 Appendix: Velocity vertical profile functions and their vertical integrals 45
2.7.1 Vertical integrals of the profile functions 48

3 **Observations at sub-inertial frequencies** 49
3.1 Introduction 49
3.2 Along-bay pressure gradients and bottom pressure 53
3.3 EOF analysis for currents 56
3.3.1 Deployment 1 57
3.3.2 Deployment 3 61
3.4 Depth-averaged momentum balances 68
3.4.1 Deployment 1 70
3.4.2 Deployment 3 71
3.5 Thermal wind balance 74
3.6 Evolution of the density field 77
3.7 Summary and conclusions 80
3.8 Appendix 81

4 **Observed response to diurnal winds** 83
4.1 Introduction 83
4.2 Sea level response to wind 85
4.3 Current response to diurnal winds 89
4.3.1 Overview 89
4.3.2 Method 89
4.3.3 Theoretical model configuration 93
4.3.4 Diurnal wind driven currents 93
4.4 Dynamics 97
4.4.1 Depth-averaged momentum balances 97
4.4.2 3D momentum balances 99
4.4.3 Estimation of the turbulent stress 103
4.4.4 Role of the variations of density 104
4.5 Summary and conclusions 107

5 **Observed response to sea level fluctuations** 108
5.1 Introduction 108
5.2 Sea level response 110
5.2.1 Sea level forcing 110
5.3 Current response 114
5.3.1 Deployment 1 114

5.3.2 Deployment 3 121
5.4 Conclusions 126
5.5 Appendix: theoretical model 127

6 **Conclusion** 129

References 132

LIST OF FIGURES

Figure 1.1: Schematic of the wind driven theoretical circulation 2
Figure 1.2: Bathymetric map of Bahía Concepción 4
Figure 1.3: ADCP coverage, year long winds and stratification 8
Figure 1.4: Deployment 3, time series and spectra at ADCP location 3 13
Figure 1.5: Frequency response function of the filters used throughout the thesis 14

Figure 2.1: Bathymetry and sea level gradient response used by the theoretical model 26
Figure 2.2: Theoretical horizontal transport along the central cross section 29
Figure 2.3: Theoretical wind driven flow as a function of forcing frequency 31
Figure 2.4: Theoretical wind driven flow as a function of depth and time along the central cross section 34
Figure 2.5: Theoretical wind driven flow forced by a steady wind stress along the central section for $\delta_E = 1$ 36
Figure 2.6: Wind driven along-bay flow as a function of depth and frequency for $\delta_E = 1$ 37
Figure 2.7: Theoretical wind driven response to an onset of wind 40
Figure 2.8: Velocity vertical profile functions for $\delta_E = 1/6, 2$ and different forcing frequency σ 44

Figure 3.1: Schematic of the wind driven theoretical circulation 50
Figure 3.2: Observed low-passed pressure-wind relationship 54
Figure 3.3: Deployment 1, EOFs of the current at ADCP location C and E 57
Figure 3.4: Deployment 1, skill and p-values of a least squares regression between lagged wind stress (τ^x) and semi-diurnal tidal envelope (a^{12}) and the first three current EOFs 59
Figure 3.5: Deployment 1, observed sub-inertial wind driven currents . 60
Figure 3.6: Deployment 3, EOFs of the observed currents 63
Figure 3.7: Deployment 3, skill and p-values of a least squares regression between lagged wind stress (τ^x) and tidal envelopes (a^{12}) and the first three current EOFs 64
Figure 3.8: Deployment 3, observed sub-inertial wind driven current . . 66
Figure 3.9: Thermal wind balance, deployment 3 76
Figure 3.10: Deployment 1, Evolution of vertical stratification and the horizontal distribution of density 79

Figure 4.1: Observed sea level response to wind stress as a function of frequency 88
Figure 4.2: Depth-averaged and baroclinic current spectra, deployment 1 ADCP C and deployment 3 ADCP 4 90
Figure 4.3: Deployment 3, skill and p-values of a least squares between diurnal currents and wind stress and tides 92
Figure 4.4: Comparison between observed and theoretical hodographs of current forced by a 0.5m amplitude diurnal sea level oscillations and a 0.05Pa amplitude diurnal wind stress 96
Figure 4.5: Diurnal band, standard deviations of momentum balances at ADCP location 4 100
Figure 4.6: Diurnal band, correlation between residual and wind stress and between left hand side of the balance and pressure gradient 102
Figure 4.7: Diurnal band, regression between shear and turbulent stress ADCP 4 103
Figure 4.8: Diurnal and super-inertial band, comparison between current and horizontal density anomaly EOFs 106

Figure 5.1: Spectra of observed sea level and transfer function between closed end and mouth sea levels 113
Figure 5.2: Sea level forced depth-averaged currents, ADCP location C and E, deployment 1 116
Figure 5.3: Deployment 1, squared coherence between sea level and current fluctuations averaged over depth and ADCP locations C and E 117
Figure 5.4: Deployment 1, along-bay currents forced by a 1 m fluctuation of sea level at BC mouth as a function of depth 119
Figure 5.5: Deployment 1, across-bay currents forced by a 1 m fluctuation of sea level at BC mouth as a function of depth 120
Figure 5.6: Sea level forced depth-averaged currents, ADCP location 1 to 6, deployment 3 122
Figure 5.7: Deployment 3, along-bay current amplitude forced by a 1 m fluctuation of sea level at BC mouth as a function of depth 124
Figure 5.8: Deployment 3, across-bay current amplitude forced by a 1 m fluctuation of sea level at BC mouth as a function of depth 125
Figure 5.9: Bathymetry used for the interconnected basins configuration of the theoretical model 128

LIST OF TABLES

Table 1.1: Instrument location name conventions. 7
Table 1.2: Winter wind stress mean and principal axis statistics 9
Table 1.3: 15 largest tidal harmonic constituents of sea level inside BC 10

Table 3.1: Regression between the along-bay pressure gradient $h\partial_x P^s$, the pressure at the North and South station and the wind stress at the North and South station 56
Table 3.2: Deployment 1. Depth averaged momentum balance in the x direction 70
Table 3.3: Deployment 1. Depth averaged momentum balance in the y direction 70
Table 3.4: Deployment 3. Depth averaged momentum balance in the x direction 73
Table 3.5: Deployment 3. Depth averaged momentum balance in the y direction 73

Table 4.1: Kinetic energy partition during deployment 1 and 3 at ADCP location C and 4 91
Table 4.2: Diurnal band, standard deviations of terms in the along-bay depth-averaged momentum balance 98
Table 4.3: Diurnal band, standard deviations of terms in the across-bay depth-averaged momentum balance 99

ACKNOWLEDGMENTS

I wish to thank my advisor, Clinton D. Winant, who gave me the opportunity to carry on this thesis and explore a fascinating area of science, Coastal Oceanography. All along my thesis, Clinton wisely guided the management of my time which ultimately led to the completion of this work. I would also like to thank Kraig B. Winters who contributed to multiple scientific issues tackled by this thesis. Furthermore, the remainder of my committee members: Myrl C. Hendershott, Stefan G. Llewellyn Smith, Mark D. Ohman. Stefan G. Llewellyn Smith and Mark D. Ohman carefully reviewed the present thesis.

The experimental part of this study has been achieved thanks to the hard work of Guillermo Gutiérrez de Velasco from the CICESE in La Paz, Mexico, his technical team and Arnoldo Valle-Levinson from the University of Florida. I am deeply thankful to all of them.

I would like to thank IOD programmer analysts (Jerry Wanetick and Nate Huffnagle), the IOD administration (Christine Delmastro in particular) and the Hydraulics Laboratory at Scripps (Charles Coughran and John Lyons). They all contributed in various ways to the present work.

Last but by no means the least, I would like to thank my love Delphine whose support and joy for life made everyday of the last years ever sunnier.

The text of Chapter 2, in part or in full, is a reprint of the material submitted in Journal of Physical Oceanography. The dissertation author was the primary researcher and author of the submitted work.

VITA

2003	Diplôme de l'École Polytechnique École Polytechnique, Paris, France
2003–2009	Research Assistant Scripps Institution of Oceanography, University of California, San Diego
2009	Ph.D., Oceanography Scripps Institution of Oceanography, University of California, San Diego.

PUBLICATIONS

Ponte, A.L.S. (2009). Periodic Wind-Driven Circulation in an Elongated and Rotating Basin. *J. Phys. Oceanogr.*, in revision.

SELECTED PRESENTATIONS

Ponte, A.L.S., Guillermo Gutiérrez de Velasco, Arnoldo Valle-Levinson, Clinton D. Winant and Kraig B. Winters, 2008: Wind driven circulation in a semi-enclosed and well-mixed bay, Bahía Concepción, *Physics of Estuaries and Coastal Seas*, Liverpool, UK.

Ponte, A.L.S., 2008: Theoretical model of the time-dependent wind driven flow in a rotating basin, *Ocean Sciences meeting*, Orlando, Florida.

Ponte, A.L.S., Guillermo Gutiérrez de Velasco, Arnoldo Valle-Levinson, Clinton D. Winant and Kraig B. Winters, 2007: Circulation in a Semi-enclosed Bay Driven by Sea Level Variations and Wind, *Estuarine Research Federation*, Providence, Rhode Island.

Ponte, A.L.S., Guillermo Gutiérrez de Velasco, Arnoldo Valle-Levinson, Clinton D. Winant and Kraig B. Winters, 2006: Drifter observations in a bay driven by wind and tide: Bahía Concepción, *Ocean Sciences meeting*, Honolulu, Hawaii.

ABSTRACT OF THE DISSERTATION

Wind and tidal response of a semi-enclosed bay,
Bahía Concepción, Baja California

by

Aurélien L. S. Ponte
Doctor of Philosophy in Oceanography
University of California, San Diego, 2009
Professor Clinton D. Winant, Chair
Professor Myrl C. Hendershott, Co-chair

In this dissertation, I report on a field study that took place in Bahía Concepción (BC), Baja California, and related modeling. The principal goal of this thesis is to extract the winter wind driven response of the bay and compare it with recently developed theoretical models. The first results of this thesis are nevertheless theoretical and derived from an extension of previous models to the time-dependent case. This extension allows to quantify the spin up time scale of the steady response. A damped resonant response is predicted at the inertial frequency. This is a result of importance for BC, which is located at 26.7°N where the diurnal sea breeze oscillates at a near-inertial frequency. This theoretical development guides the analysis of observations inside BC. This analysis consists first in understanding the sub-inertial response. The along-bay sea level set-up predicted by theory is observed. Wind driven currents proved to be more difficult to extract and the comparison with theory is partially successful. Downwind currents are present over shallow areas and cross-wind currents are sometimes observed. An analysis of the dynamics suggests the importance of stratification and nonlinearities which are ignored in the theoretical models. In the diurnal/inertial band, the response is similar to the theoretical predictions developed in the early part of this

thesis. Two layer-like currents are present and rotate in the clockwise direction with time. When vertical stratification is present, baroclinic effects are shown to contribute to the dynamics. Finally, I extract the current and sea level response to sea level fluctuations at the mouth of BC. The sea level at the closed end of BC follows a theoretical model with two interconnected basins. There is a resonant response near 5 cycles per day, which is identified as the quarter wavelength of the bay. Along-bay currents are consistent with theoretical predictions. This is not the case for across-bay currents.

1

Introduction

1.1 Introduction

The ecological and societal importance of small coastal basins (bays, estuaries, lagoons) is out of proportion with their small size. Among many other important ecological functions, lagoons and estuaries serve as way stations for birds migrating from Canada and the US to Mexico and Central America, as nurseries for an immense variety of fauna and flora and as mating and calving grounds for marine mammals such as the Pacific gray whale. At the same time these water bodies have been deeply impacted by anthropogenic activities. Many, if not all, are used as pathways through which sewage and contaminated waters are introduced into the ocean. The impact of human activity on ecological function can be moderated by proper management and science-based engineering.

In general, the health of coastal wetlands and embayments and their ability to function, in an ecological sense, depends on the rate at which water circulates within the basin and is exchanged with the adjacent ocean. That circulation is the product of physical processes forced by a combination of winds, tides and buoyancy. The primary focus of this thesis is on the wind driven circulation.

In well-mixed coastal basins, theoretical models (Winant, 2004) and nu-

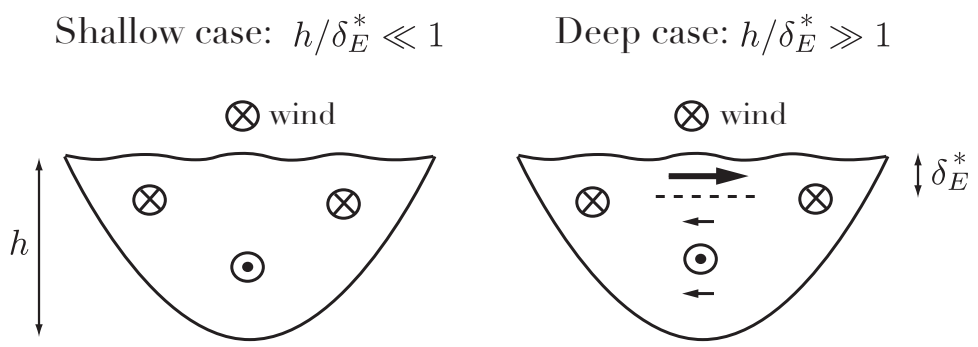

Figure 1.1: Schematic of the theoretical circulation (Winant, 2004) driven by an along basin wind stress blowing over shallow (left) and deep (right) basin. The Ekman depth is $\delta_E^* = \sqrt{K/f}$, where K is the turbulent eddy viscosity and f the Coriolis frequency.

merical experiments (Sanay and Valle-Levinson, 2005) have shown that the circulation driven by a steady wind stress critically depends on the ratio of the Ekman depth ($\delta_E^* = \sqrt{K/f}$, where K is the turbulent eddy viscosity and f the Coriolis frequency) to the basin depth h.

In a shallow coastal basin, i.e. shallower than an Ekman depth, the Coriolis acceleration is small compared to the large vertical divergence of turbulent stress imposed by the proximity of the surface and bottom. The dynamics is thus nonrotating. The wind stress drives a downwind current at the surface balanced by a pressure gradient driven upwind flow at depth. This pressure gradient is a set up of the sea level in the downwind direction and is required by the bounded nature of the basin and mass conservation. If there are bathymetric variations, shallow areas are dominated by the wind with a net downwind depth-averaged flow (Figure 1.1). Deeper areas are dominated by the counterbalancing pressure gradient with net upwind vertically averaged flow. Csanady (1973), Wong (1994) and Mathieu et al. (2002) present theoretical models of the wind driven circulation in shallow basins. Such circulations were observed by Weisberg and Sturges (1976), Weisberg (1976), and more recently by Gutiérrez de Velasco and Winant (2004) and Narváez and

Valle-Levinson (2008).

In a deep coastal basin, i.e. deeper than an Ekman depth, the Coriolis acceleration is comparable to other terms involved in the momentum balance and fundamentally modifies the wind driven circulation. The direct effect of the wind is confined to the surface in a surface Ekman layer with a net transport to the right of the wind, as in the classical Ekman layer. Sea level slopes produce currents to their left through geostrophy. A circulation therefore develops in the direction perpendicular to the wind (Figure 1.1). The residence times within the basin are increased and exchanges with the adjacent ocean reduced. Winant (2004) and Sanay and Valle-Levinson (2005) investigated theoretically and numerically the case of deep wind driven basins. No direct observations of this type of response have been made yet. The Asymmetric Circulation in Wind-Driven Bays project (2004-2009), which funded this thesis, was designed to remedy this lack of observations.

This thesis reports on the fall and winter observations collected during the experimental phase of the project as well as on advances made in the theoretical modeling of wind driven circulations in coastal basins. The next section describes the experimental site, Bahía Concepción (BC), as well as the instrumentation and the observed climatological cycle. Section 1.3 presents an overview of the thesis and explains its structure.

1.2 Observations

1.2.1 Bahía Concepción

BC is located on the east shore of Baja California, México (Figure 1.2), connected to the Gulf of California (GC). The bay owes its elongated shape, 40 km long by 5 to 10km wide, to its half-graben structure, i.e. the result of land down-throw near a geological fault zone (McFall, 1968; Johnson and Ledesma-Vásquez, 2001). There are counterbalancing land upthrows on the west along the El Reyque-

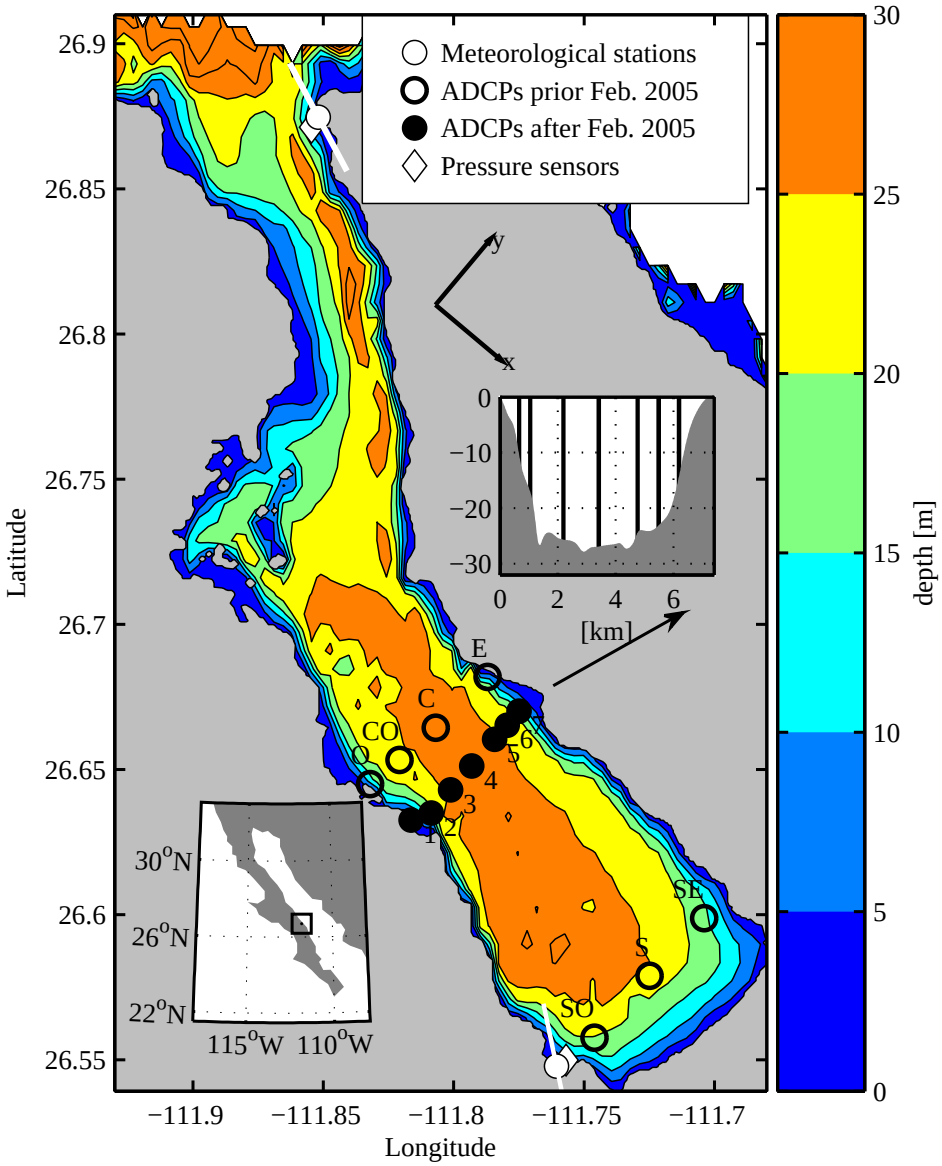

Figure 1.2: Bathymetric map of Bahía Concepción. Depth is indicated by the color shading and contours, instruments by the large symbols. The vertical section in the middle is along the ADCP line. The position of Bahía Concepción with respect to the Baja Peninsula is represented by the black square on the bottom left map. The arrows represent the chosen along-(x) and across-(y) bay directions.

son fault zone with steep escarpments, and the east along the Concepción fault zone with a long bajada reaching 600 m high. The presence of these topographical features is believed to steer the wind in the along-bay direction. BC was chosen among other reasons for its relatively simple bathymetry. At its mouth, there is a 15 m deep sill followed just south of it by a narrow V-shaped channel. The sea floor is a nearly flat bottom surrounded by steep walls (1 to 10% slopes) from the middle of the bay up to the closed end. The sea floor surfaces at the closed end along a mild slope (less than 1%). The maximum and average depth of the bay are around 35 m and 20 m respectively. This depth range is larger than the expected Ekman depth, 7 m for a typical turbulent eddy viscosity of 2×10^{-3} m^2/s, which is the reason why BC was selected. The system of coordinates used throughout this manuscript has the x axis running in the along-bay direction, positive toward the closed end, and the y axis in the across-bay direction (Figure 1.2).

1.2.2 Instrumentation

The experiment inside BC lasted from November 2004 to October 2005. This thesis is focuses on the Fall and Winter observations (November 2004 to March 2005), i.e. when the bay is the least vertically stratified. Instrument deployment locations are indicated in Table 1.1.

Wind velocities were recorded using Aanderaa anemometers sampling at a 1 Hz. The anemometers were deployed on land at a height of 10 m above mean sea level at the mouth (MET2) and the head (MET1) of the bay (Figure 1.2). While the time series at the north meteorological station are nearly continuous, the south station cables were disconnected several times. The time coverage is thus poor at the south, in particular during the summer period. The wind stress was computed according to standard formulas (Large and Pond, 1981). The meteorological station additionally recorded air temperature, humidity but *not* atmospheric pressure.

Less than 1 km away from the meteorological stations, SeaBird SBE26

wave and tide recorders equipped with 45 psi Paroscientific pressure sensors were moored in 5m depth. Burst of pressure measurements provided wave averaged sea level as well as wave period and height every 15 min. These pressure observations led to an estimate of the wind driven sea level set up in the along-bay direction.

Currents measurements are central to this study and were collected with Acoustic Doppler Current Profilers (ADCPs). The ADCPs were RDI Workhorse (1200kHz and 600kHz) averaging 60 pings over 2.5 min time intervals. Moored on the sea floor and looking upward, the ADCPs measured the current averaged in 1 m bins over most of the water column above. The first bin is located 50 cm (1200 kHz) or 1 m (600 kHz) above the head of the ADCP, limited by transducer ringing. The distance between the transducer and the last bin is limited by the reflection of the acoustic side lobes on the sea surface. For transducers pointing at a 20° angle from the vertical, this distance is approximately 95% of the transducer to sea surface spacing.

The first two ADCP deployments (Fall and Winter up to end of January 2005) consisted of two sections of three ADCPs, located at the center and at the closed end of BC (Figure 1.3). The second deployment was short, around 17 days long, and aimed at measurements of turbulent quantities. The ADCP locations are labelled with letters until February 2005 (O,CO,C,E,SO,S,SE). This deployment strategy lead to a poor resolution in the across-bay direction and was abandoned later on. The second strategy gathered all ADCPs along one single cross-section, increasing thereby the resolution in the across-bay direction (Figure 1.2). The ADCP locations were then labelled 1 to 7, from west to east. This deployment strategy was maintained until the end of the experiment.

Starting in February 2005, 6 chains equipped with temperature loggers spaced vertically every 5 meters were moored at ADCP positions 1 to 7 but not 4. The temperature was recorded every 4 min.

Other type of measurements, not discussed in the present thesis, were collected over the course of the experiment. In March 2005, an extensive survey

of the water properties and currents inside BC was conducted on board the R/V Sproul. Davis type drifters (Davis, 1985) with 0, 15 and 25 m deep drogues were released at various location inside BC. Their surface floats were equipped with a GPS that recorded the position every minute.

Table 1.1: Instrument location name conventions.

Location name	Longitude [°]	Latitude [°]	Depth [m]	Instrument type
MET1	-111.7569	26.5499	-10	Meteorological station
MET2	-111.8545	26.8712	-10	Meteorological station
PS1	-111.7606	26.5478	5.5	Pressure gauge, CTD (SBE26)
PS2	-111.8519	26.8747	5	Pressure gauge, CTD (SBE26)
SO	-111.7460	26.5576	16.5	ADCP
S	-111.7249	26.5789	25.8	ADCP
SE	-111.7040	26.5988	17.8	ADCP
O	-111.8321	26.6450	16.1	ADCP
CO	-111.8208	26.6533	25	ADCP
C	-111.8069	26.6644	28	ADCP
E	-111.7870	26.6819	16	ADCP
1	-111.8114	26.6326	16.2	ADCP, Tloggers (5,10,15m)
2	-111.8086	26.6350	20.8	ADCP, Tloggers (5,10,15m)
3	-111.8012	26.6430	26.8	ADCP, Tloggers (5,10,15,20,25m)
4	-111.7931	26.6512	27.8	ADCP
5	-111.7843	26.6604	24.8	ADCP, Tloggers (5,10,15,20,25m)
6	-111.7795	26.6653	25.5	ADCP, Tloggers (5,10,15m)
7	-111.7749	26.6701	16.1	ADCP, Tloggers (5,10,15m)

1.2.3 Climatological conditions, forcings

The wind climatology inside the Gulf of California is monsoonal, organized around a mid-latitude winter and a subtropical summer (Badan-Dangon et al., 1991). In winter, the prevailing winds are from the north with occasional 3-5 days bursts of cold southeastward winds ("Nortes"). In the summer, the climatic conditions are controlled by a low pressure located over the Sonoran Desert with mean winds from the south. Wind stress at the BC north and south meteorological stations as well as a QuickSCAT estimate of wind stress at the center of the GC reproduce this seasonal cycle (Figure 1.3). Winter time statistics at the meteorological stations are the most relevant to this manuscript and are summarized in Table 1.2. A low pass filter (33h cutoff) is applied to the wind stress time series to separate weather band winds from sea breeze and higher frequencies

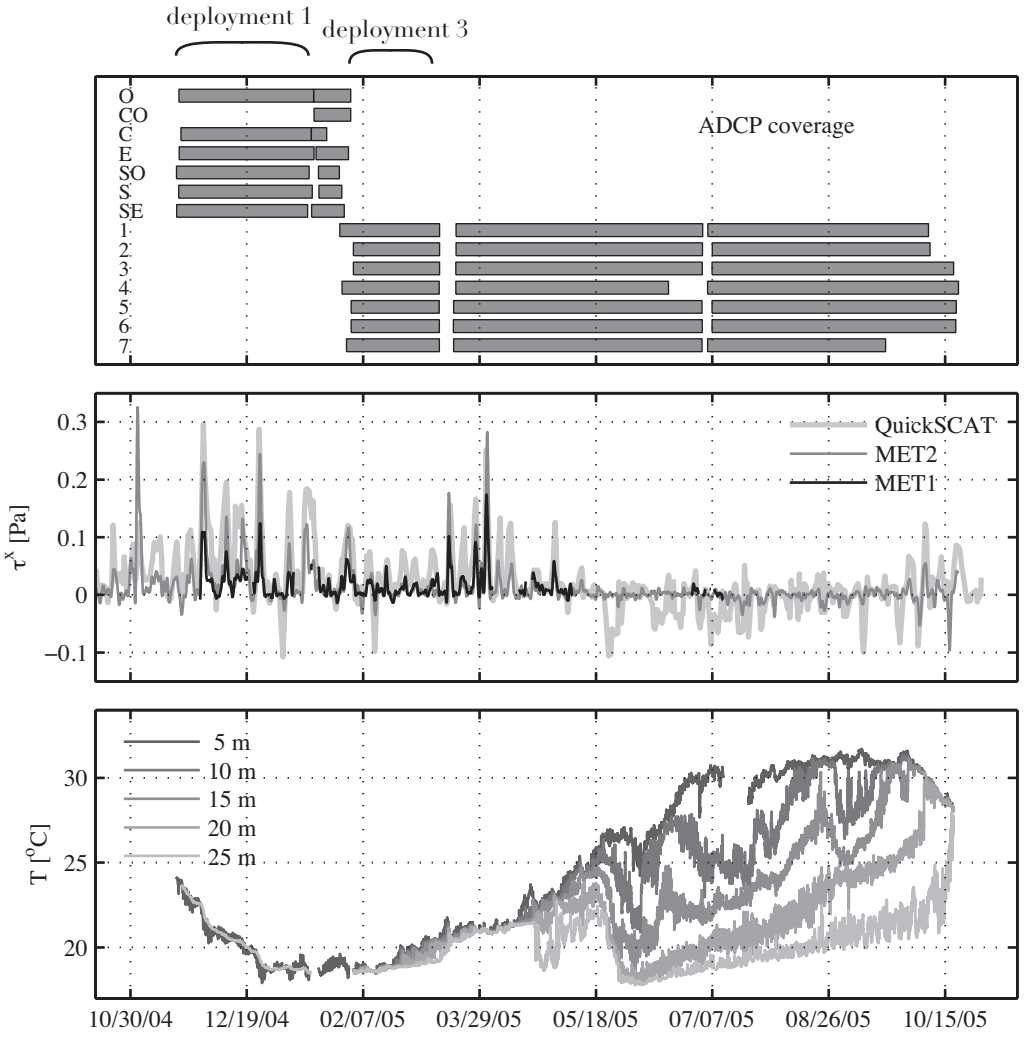

Figure 1.3: The top panel shows the time and location of all ADCP deployments. The central panel is the low-pass filtered along-bay wind stress at the MET1, MET2 as well as the along-GC axis wind stress from QuickSCAT. The QuickSCAT estimate is an average over a 30km wide square in the middle of the GC in front of the Bahía Concepción. The lower panel is the temperature at ADCP3 and at $5, 10, 15, 20, 25$ m depths from February 2005 to the end of the experiment. Before this time period, the temperature at 25 and 5 m depth are estimated from ADCP C and an average between PS1 and PS2 temperatures.

Table 1.2: Mean and principal axis statistics of the wind during winter (October 2004 to May 2005). Low-passed quantities are above high-passed quantities.

Mean magnitude 10^{-2}Pa	Major / Minor axis 10^{-2}Pa	Mean orientation °TN	Principal axis orientation °TN
	North meteorological station		
2.05	4.19 / 0.91	152.6	146.7
	2.18 / 1.23		168.2
	South meteorological station		
1.52	2.35 / 0.81	161.6	165.6
	2.45 / 1.07		174.1

winds. The Nortes episodes dominate the low frequency statistics. The ratio of low-passed wind stress major axes is around 1.8 indicating a decrease of the wind from the north to the south station during Nortes. Both are weaker than the QuickSCAT estimate of the wind stress at the center of the GC. The major and minor axis of the high-passed wind stress are, in contrast, similar at both stations, slightly larger at the south. The ratio of minor to major axes indicates the wind is quasi-unidirectional, roughly aligned with BC's orientation (Figure 1.2). This ratio is larger for high-passed wind stress and shows that the direction of the wind is more variable at higher frequencies. Overall, this suggests that the mouth of BC is more representative of open Gulf conditions but its closed end is more strongly influenced by land.

A tidal harmonic analysis (Pawlowicz et al., 2002) of the sea level inferred from the bottom pressure measurement is shown on Table 1.3. The tide is mixed dominant diurnal with a form number (K1 + O1)/(M2+S2) of 2.1 at the closed end and 2.4 at the mouth (Defant, 1961a). This is explained by the proximity of an amphidromic point of semi-diurnal tide inside the GC (Morales and Gutiérrez, 1989; Godin, 1993; Filloux, 1973; Hendershott and Speranza, 1971). The amplitudes of the major diurnal and semi-diurnal constituents are consistent with these previous studies. For each harmonic constituent, there is an increase of amplitude and phase from the open end to the closed end, related to the standing wave nature

Table 1.3: 15th largest tidal harmonic constituents of the sea level at the south (S) and north (N) stations. f refers to the frequency of the harmonics in cpd, A to its amplitude in cm, ϕ to its Greenwich phase in degrees.

	f	A_S	A_N	ϕ_S	ϕ_N
	cpd	cm	cm	°	°
K1	1.003	28.99	28.26	179.5	179.2
O1	0.9295	19.2	18.61	169.7	169.2
P1	0.9973	9.148	8.946	179	176
Q1	0.8932	3.777	3.679	160.1	160.5
J1	1.039	1.634	1.645	187.5	187.3
NO1	0.9664	1.479	1.44	165.8	163.7
S2	2	11.09	9.68	129	127.9
M2	1.932	10.06	8.486	151.5	150.3
K2	2.005	2.876	2.478	118.6	118.3
N2	1.896	2.825	2.386	174.6	174.5
MU2	1.865	1.312	1.169	176.8	177
M3	2.898	1.164	0.8189	212.9	208.2
M4	3.865	3.019	1.482	23.3	18.85
MS4	3.932	1.562	0.6808	54.53	45.95
MN4	3.828	1.122	0.5897	328.3	322.8

of the tidal wave inside BC and the short length of the bay compared to the tidal wavelength (see chapter 5).

The only reports on the hydrography of BC have been found in studies of plankton communities (Lopez-Cortes et al., 2003; Palomares-Garci et al., 2006; Canar et al., 2008). The hydrographic annual cycle is centered around a cold and well-mixed period in fall and winter, maintained by the cold and strong Nortes, and a warm and stratified period in spring and summer when winds are weaker. Intrusions of nutrient rich water from the GC have been observed at the spring transition in April-May (Palomares-Garci et al., 2006). During summer conditions, the bottom layer is anoxic (Lechuga-Deveze et al., 2001). A similar temperature cycle was observed over the course of our experiment (Figure 1.3, lower panel). The intrusions of cold water at the spring transitions are indicated by the two sudden temperature drops at depth (Cheng et al., 2010). As the climate is subtropical and arid, evaporation rates are expected to be high inside BC, most probably of the order of several meters per year (Mendoza-Salgado et al., 2006; Winant and Gutiérrez de Velasco, 2003). These evaporation rates could potentially drive a circulation typical of inverse estuaries in order to maintain the salt balance inside

BC (Winant and Gutiérrez de Velasco, 2003; Tragou and Garrett, 1997; Nunes-Vaz et al., 1990; Phillips, 1966). This issue has not been addressed yet, nor is it by the present manuscript. Average annual precipitation is reported to range between 100 and 200 mm in the BC area, 80% of it occurring during summer tropical rainstorms (Mendoza-Salgado et al., 2006). These rainstorms have been shown to modify nitrogen and phosphorus levels, but their impact on the physics of the bay is unknown.

1.2.4 Overview of observed current fluctuations

ADCP deployment 3 is the only available deployment with all ADCPs aligned along a single transect and vertical stratification reduced compared to summer time (Figure 1.3). This time period is thus subject to a thorough analysis in this manuscript. An overview of the current observed at the ADCP3's top most bin is given on Figure 1.4. Sea level and wind stress are also shown as they are the expected main drivers of the flow.

One of the most striking feature of the observed currents is that they are a superimposition of contributions with a broad range of frequencies. In the along-bay direction, there is a 8 cm/s mean current toward the closed end of BC. In both directions, there are fluctuations at sub-inertial and diurnal frequencies with typical amplitudes of 5 cm/s. Higher-frequency contributions are more difficult to isolate from the time series and an inspection of the spectra is necessary for this purpose. In the along-bay directions, well-defined spectral peaks are found at semi-diurnal and higher tidal harmonics frequencies (4 cpd and 5 cpd). Spectral peaks are observed up to 40 cpd. In the across-bay direction, the spectral density is different with little energy past the diurnal frequency. The spectral density of depth-averaged current agree well with the top-most bin current in the along-bay direction. The current is thus most likely depth uniform in the along-bay direction. In the lateral direction, the depth-averaged current is an order of magnitude smaller

than the top most bin current. The across-bay currents are vertically sheared and balanced, consistent with BC being elongated (see, e.g., chapter 2).

There is no clear relationship between the sea level and wind stress fluctuations and the currents fluctuations, based on an inspection of the time series. This is due to the large number of signals superimposed and suggests that filtering is required in order to relate forcing and current response. Spectral density estimates of sea level and along-BC current have similar peaks between 1 and 5 cpd and around 40 cpd, indicating there a relationship between them. While this turns out to be true at super-inertial frequencies (chapter 2), the case of the diurnal/inertial band is more complicated. There are, for example, times (12-13/02 and 27-28/02) when the diurnal sea level fluctuations are small while the diurnal oscillations of current are large. Chapter 3 explains how diurnal currents are driven both by the wind stress and sea level. This is possible because the wind stress is strongly modulated at the diurnal frequency due to a significant sea breeze and because the response to a diurnal wind is near resonant at the latitude of BC.

1.3 Overview

Chapter 2 presents a theoretical model of the circulation forced by a periodic wind in a well-mixed elongated basin. It is an extension of Winant (2004) to the time periodic case. This problem depends on three non-dimensional variables: the ratio of the Ekman depth to the basin depth; the ratio of the wind forcing to the Coriolis frequency; and the product of the gravity wave number and the basin length, i.e. a measure of the horizontal dimensions of the basin. Solutions are discussed as a function of the forcing frequency for the case of a basin deeper than an Ekman depth with small horizontal dimensions, similar to BC. A resonance is observed when the wind oscillates at the inertial frequency. The current is then sheared vertically and rotates in the clockwise direction with time. The spin up of the steady circulation (Winant, 2004) is shown to be controlled by the slower

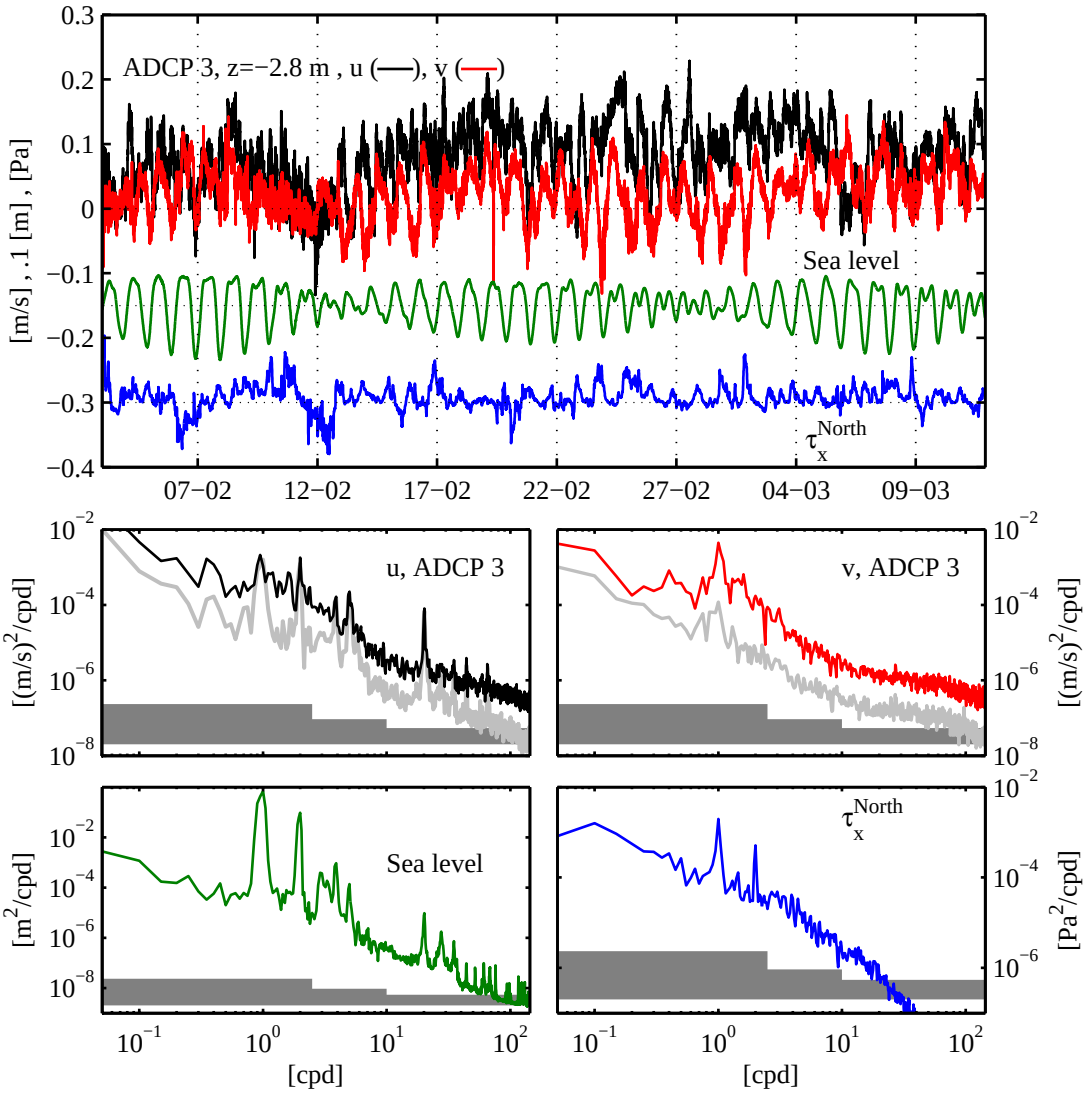

Figure 1.4: ADCP deployment 3 time series of sea level and wind stress at the mouth and along-(u) and across-(v) bay current at the ADCP3's top most bin (upper panel). Currents are *not* offset vertically. Spectral densities of the same time series are shown below. Spectral densities of depth-averaged current are shown in light gray. The gray shadings are 95% confidence intervals.

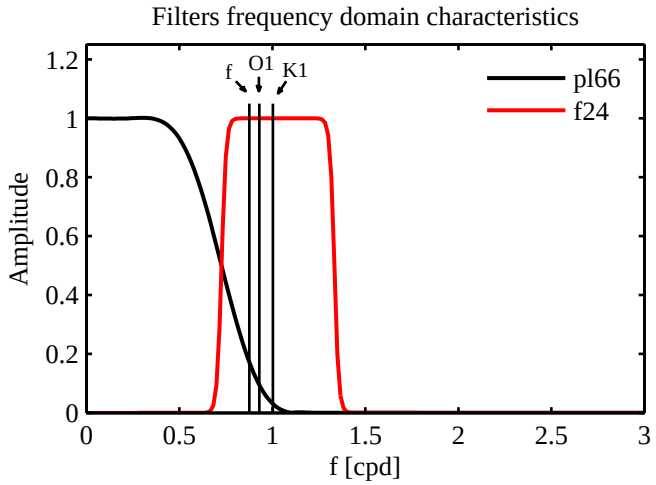

Figure 1.5: Amplitude of the frequency response function of pl66 and f24. pl66 is a time domain low-pass filter. f24 is a frequency domain band-pass filter.

spin up of the circulation in the along-bay direction. This chapter suggests that the response to sub-inertial and diurnal wind have to be investigated separately, hence the structure of the remaining of the manuscript.

Chapter 3 investigates sub-inertial currents inside BC (Figure 1.5). The ultimate goal is to extract the wind driven response and compare it with steady theoretical models (Winant, 2004), i.e. the principal motivation for the Asymmetric Circulation in Wind-Driven Bays project. The sea level response to wind appears clearly as a set up in the downwind direction, consistent with the models. As far as currents are concerned, the situation is complicated by the weakness of wind driven currents compared to the first-order currents. Deployment 3 seems to be the most successful at showing the expected wind driven lateral circulation. During deployment 2, the lateral circulation is weaker, indicating a larger turbulent mixing. Attempts are made to understand the dynamics of the first-order low-frequency currents, which could ultimately lead to a better understanding of the wind driven currents.

In chapter 4, an analysis of the currents in the diurnal band (Figure 1.5) separates wind driven and sea level driven currents. The wind driven current

response rotates in the clockwise direction with time, consistent with the theoretical prediction of chapter 2. An inspection of the dynamics using the momentum balance shows, however, that it is different than that expected from theoretical predictions, with a larger contribution of internal baroclinic pressure gradients.

The sea level response at BC's closed end, as well as the current driven by fluctuations of sea level at BC's mouth, are the subject of chapter 5. The sea level response is compared with an analytical model prediction. Properties of the current response are examined in separate frequency bands.

2

Theoretical wind driven circulation in an elongated basin

2.1 Introduction

Theoretical models of the response to steady winds inside non rotating and well-mixed basins have established how the lateral variability of the flow is controlled by bathymetry (Csanady, 1982; Hunter and Hearn, 1987; Wong, 1994; Mathieu et al., 2002; Winant, 2004). For flat basins, the vertically integrated flow is zero everywhere with a downwind flow at the surface. In order to conserve mass through any vertical section, the sea level rises in the downwind direction and drives an upwind current at depth. For basins with variable bathymetry, the wind stress dominates over shallow areas where the flow is downwind, while the upwind current is located over deeper areas (Mathieu et al., 2002). Observations confirm these theoretical results (Gutiérrez de Velasco and Winant, 2004).

Winant (2004) and Winant (2006) extended these results by including the effect of the rotation of the Earth. The nondimensional Ekman depth $\delta_E = \sqrt{2K/f^*H^{*2}}$, where K is the eddy viscosity, H^* the water depth, and f^* the Coriolis frequency, determines the importance of the rotation of the Earth. At low

δ_E, the wind stress drives a net transport to its right, in a surface Ekman layer of size δ_E. This transport is balanced by a flow in the opposite direction driven by the downwind increase of sea level, spread over the whole water column and thus weaker. Looking in the downwind direction, the resulting lateral circulation is anticyclonic. There is on top an axial circulation similar to the nonrotating case. For increasing values of δ_E the nonrotating picture is recovered. Numerical experiments confirm these results (Sanay and Valle-Levinson, 2005)

The issue of time dependance was first addressed by models solving for the vertically integrated flow (Csanady (1968a) and Csanady (1968b), corrected by Birchfield (1969)). These models describe the early response of a basin initially at rest to a sudden onset of wind. This response is the sum of a steady sea level increase in the downwind direction along with oscillations at discrete frequencies. The fastest of these oscillations are gravity waves of Poincaré type. If the basin is larger than the Rossby radius of deformation, the gravest are combinations of Kelvin waves traveling along the basin boundaries. These oscillations are excited at discrete frequencies because of the bounded nature of the domain and are called seiches. They are not damped because of the frictionless nature of the models and oscillate indefinitely inside the basin. These waves are filtered out by the commonly made rigid-lid approximation. If the basin has a variable bathymetry, topographic waves (also called second class waves, vortex modes or quasi-geostrophic waves) are also excited by an onset of wind stress. They have lower frequencies, typically a fraction of the inertial frequency. Their nature is different than gravity waves (first class waves) as they rely on rotation and variations of the basin bathymetry through conservation of potential vorticity. They have been studied theoretically in idealized cases (Lamb, 1932; Ball, 1965; Birchfield and Hickie, 1977), modelled (Rao, 1976; Huang and Saylor, 1982; Stocker and Hutter, 1987) and observed, mostly in lakes (Saylor et al., 1980). These waves do exist in basins of horizontal dimensions smaller than a Rossby radius of deformation. Their period increases with flatter bathymetries or smaller Coriolis frequencies (Stocker and Hutter, 1987).

None of these time-dependent models describes the three-dimensional structure of the wind driven response. Such a description requires consideration of the effect of the vertical diffusion of momentum, as with the steady models previously described. Mohammed-Zaki (1980), closely following Greenspan and Horward (1963), computed the response of a flat and deep ($\delta_E \ll 1$) basin to a sudden onset of wind under the rigid-lid assumption. The increase of sea level in the downwind direction is thus instantaneous and immediately accelerates the core of the water column. Vertical diffusion of momentum controls the flow near the bottom and the surface. After a few inertial periods, $t_i = 2\pi/f^{*-1}$, the effect of the Coriolis force is felt, the core becomes geostrophic and the bottom and surface boundary layers become Ekman layers. Superimposed inertial oscillations, intensified at the surface, decay over the diffusive time scale $t_d = H^{*2}/K \propto t_i/\delta_E^2$, the time it takes for the vertical diffusion of momentum from surface to bottom. If the wind stress curl is non-zero, a slow non-oscillatory mode is excited and controls the spinup of the flow over the so-called spinup time scale $t_s = t_i/\delta_E$. t_s is more commonly known as the spinup/down time scale of a geostrophic eddy.

The present chapter describes the three-dimensional response of an elongated and closed coastal basin of variable bathymetry to a time periodic but spatially uniform wind stress. The motivation is first to understand how the dynamics of the response changes with wind forcing frequency. At low frequencies, I determine when the response is similar to the steady one. This defines the quasi-steady frequency bands and provides an estimate of the spin up time scale of the bay. I describe in particular the damped resonant response to inertial winds which could be excited by a coastal sea breeze at 30° latitude (Sobarzo et al., 2007; Simpson, 2002). Second, the time periodicity provides some theoretical ground for future analysis in the frequency domain of current observations (Wong and Moses-Hall, 1998; Janzen and Wong, 2002). This model extends Mohammed-Zaki (1980) to the case of a variable bathymetry. It follows the tidal model of Winant (2007) but investigates a broader range of frequencies. This model describes sub-inertial,

inertial and super-inertial responses and therefore extends (Mitchum and Clarke, 1986) to higher forcing frequencies. The approach is also similar to Craig (1989a) and Craig (1989b), except that because the basin is closed the sea level response can be found. After a detailed description of the model in section 2.2, section 2.3 describes the sea level and transport responses. The three-dimensional velocities are described in section 2.4. In each sections, the response is investigated over the whole frequency domain as well as at selected frequencies of interest. The results are discussed in section 2.5.

2.2 The model

2.2.1 Formulation

Consider a closed basin on the f-plane, with Coriolis frequency f^*, and define L^* and H^* to be the length and maximum depth. A right-handed system of coordinates is chosen with the x^* and y^* axis in the horizontal plane and the z^* axis pointing up from the undisturbed surface. The basin bottom is located at $z^* = -h^*(x, y)$ and the sea surface at $z^* = \eta^*(x^*, y^*, t^*)$, where t^* is the time. The water velocity components in the x^*, y^* and z^* directions are u^*, v^* and w^* respectively. The basin is completely mixed, and the water density is ρ, a constant. The constant vertical eddy diffusivity is K and the horizontal diffusion of momentum is neglected ($K_h H^{*2}/KL^{*2} \ll 1$, where K_h is a typical horizontal eddy viscosity). A wind stress $\tau^* = (\tau^{*x}, \tau^{*y})$ forces the circulation inside the basin.

Dimensional (asterisk) variables are made nondimensional according to

the following scalings:

$$\begin{aligned} t = \omega^* t^*, \;\; \sigma = \omega^*/f^*, \\ (x,y) = (x^*,y^*)/L^*, \;\; (z,h) = (z^*,h^*)/H^*, \\ (u,v) = (u^*,v^*) \times \rho K/\tau_0 H^*, \\ w = w^* \times \rho K L/\tau_0 H^{*2}, \\ \eta = \eta^* \times \rho g H^*/\tau_0 L, \;\; \tau = (\tau^x,\tau^y) = \tau^*/\tau_0, \end{aligned} \tag{2.1}$$

where ω^* is the frequency of the wind forcing, and τ_0 is the maximum amplitude of the wind stress. The current velocities have been scaled consistently with the imposed surface stress boundary condition whereas the sea level scaling follows the horizontal momentum equations 2.3 and 2.4.

The linear and hydrostatic assumptions are valid if $\tau_0 H^{*3}/\rho K^2 L^* \ll 1$ and $g/\omega^{*2} H^* \gg 1$ respectively. Under both assumptions, the nondimensional equations of motion are:

$$\partial_x u + \partial_y v + \partial_z w = 0, \tag{2.2}$$

$$\partial_{zz} u - \frac{2}{\delta^2}\partial_t u + \frac{2}{\delta_E^2} v = \partial_x \eta, \tag{2.3}$$

$$\partial_{zz} v - \frac{2}{\delta^2}\partial_t v - \frac{2}{\delta_E^2} u = \partial_y \eta, \tag{2.4}$$

where $\delta = \sqrt{\frac{2K}{\omega^* H^{*2}}}$ is the thickness of the oscillating boundary layer where the vertical diffusion of momentum balances the oscillations of the flow. The thickness of an Ekman boundary layer, where the vertical diffusion of momentum balances the Coriolis acceleration, is $\delta_E = \delta \times \sqrt{\sigma}$. The Ekman number is $\sqrt{\delta_E}$ (Pedlosky, 1987). The nondimensional forcing frequency $\sigma = \sqrt{\delta_E/\delta}$ is then a measure of the relative size of these boundary layers and determines the vertical profiles of currents (Appendix 2.7).

At the surface the vertical momentum stress equals the wind stress and the kinematic boundary condition is linearized. At the bottom a no-slip condition

is used which leads to the following vertical boundary conditions:

$$\partial_z u = \tau_s^x,\ \partial_z v = \tau_s^y \text{ and } w = \kappa^2\delta^2\partial_t\eta \text{ at } z = 0 \tag{2.5}$$

$$u = v = w = 0 \text{ at } z = -h, \tag{2.6}$$

where $\kappa = \sqrt{\frac{L^{*2}\omega^{*2}}{2gH^*}}$ is the nondimensional surface gravity wavenumber (differ from Winant (2007) by $1/\sqrt{2}$).

The solution depends on the bathymetry $h(x, y)$ along with the geometry of the basin, the surface stress distributions τ_s^x and τ_s^y; and three independent nondimensional variables, for example $(\delta_E, \sigma, R = \sigma/\kappa\sqrt{2})$. Other combinations of these three nondimensional variables may be more appropriate in some situations. For example, (δ_E, σ, R) is used in this chapter because it enables, at a fixed Coriolis frequency, the description of the effect of friction (nondimensional Ekman depth δ_E), of the horizontal dimension of the basin (nondimensional Rossby radius R) and of the forcing frequency (σ). In certain cases however, variables such as δ and κ, which are combinations of the former, will be used for convenience.

The method employed to solve the preceding set of equations involves three steps. First the assumption of time periodicity is made. Second, the three-dimensional velocities are computed analytically as function of sea level slopes and local wind stress. The last step is a numerical computation of the sea level response.

The time dependence in the equations of motion (Eq. 2.3- 2.4) is handled by assuming the wind forcing to be periodic, with frequency ω^*. Because the system of equations is linear, the problem is reduced to solving for the complex amplitudes (capitalized variables) of the currents and sea level:

$$\begin{aligned} u = \Re(Ue^{-it}),\ v = \Re(Ve^{-it}), \\ w = \Re(We^{-it}),\ \eta = \Re(Ne^{-it}), \\ \tau_s^x = \Re(T^x e^{-it}),\ \tau_s^y = \Re(T^y e^{-it}). \end{aligned} \tag{2.7}$$

With this convention, a positive phase is a delay with respect to the wind forcing.

The amplitudes satisfy:

$$\partial_x U + \partial_y V + \partial_z W = 0, \tag{2.8}$$

$$\partial_{zz} U + \frac{2i}{\delta^2} U + \frac{2}{\delta_E^2} V = \partial_x N, \tag{2.9}$$

$$\partial_{zz} V + \frac{2i}{\delta^2} V - \frac{2}{\delta_E^2} U = \partial_y N, \tag{2.10}$$

with boundary condition:

$$\partial_z U = T^x,\ \partial_z V = T^y \ \text{ and } \ W = -i\kappa^2 \delta^2 N \ \text{ at } z = 0, \tag{2.11}$$

$$U = V = W = 0 \ \text{ at } z = -h. \tag{2.12}$$

Equations 2.9- 2.10 are combined in order to produce an equation for U:

$$\begin{aligned} \partial_{zzzz} U + \frac{4i}{\delta^2} \partial_{zz} U + \frac{4}{\delta^4} (\sigma^{-2} - 1) U \\ = \frac{2}{\delta^2} (i \partial_x N - \sigma^{-1} \partial_y N) \end{aligned} \tag{2.13}$$

with boundary condition:

$$\partial_z U = T^x,\ \partial_{zzz} U = -\frac{2i}{\delta^2} T^x - \frac{2}{\delta_E^2} T^y \text{ at } z = 0, \tag{2.14}$$

$$U = 0,\ \partial_{zz} U = \partial_x N \text{ at } z = -h. \tag{2.15}$$

This step leads to the following expression of the horizontal component of the velocity:

$$U = q^N \partial_x N + r^N \partial_y N + q^T T^x + r^T T^y, \tag{2.16}$$

$$V = -r^N \partial_x N + q^N \partial_y N - r^T T^x + q^T T^y, \tag{2.17}$$

where q^N, r^N , q^T and r^T are vertical profile functions described in appendix 2.7. The flow depends on the local wind stress but also on its overall effect over the whole basin surface through the sea level slope. The vertical velocity is evaluated by vertically integrating the continuity equation (Equation 2.8).

The only remaining unknown is now the sea level. It is solved for in the last step, where the continuity equation (Equation 2.8) is integrated vertically and

combined with the boundary conditions on the vertical velocity:

$$-i\kappa^2\delta^2 N + \partial_x[U] + \partial_y[V] = 0, \tag{2.18}$$

where the brackets are used for vertically integrated quantities. Equation 2.16 and 2.17 are integrated vertically:

$$[U] = Q^N \partial_x N + R^N \partial_y N + Q^T T^x + R^T T^y, \tag{2.19}$$

$$[V] = -R^N \partial_x N + Q^N \partial_y N - R^T T^x + Q^T T^y, \tag{2.20}$$

where Q^N, R^N , Q^T, R^T are the vertical integrals of the corresponding vertical profile functions and are given in appendix 2.7. Substitution of Equation 2.19-2.20 in Equation 2.18 leads to a complex elliptic equation for the sea level:

$$\begin{aligned} Q^N(\partial_{xx} + \partial_{yy})N + (\partial_x Q^N - \partial_y R^N)\partial_x N \\ +(\partial_y Q^N + \partial_x R^N)\partial_y N - i\kappa^2\delta^2 N \\ = -\partial_x(Q^T T^x) - \partial_x(R^T T^y) \\ +\partial_y(R^T T^x) - \partial_y(Q^T T^y). \end{aligned} \tag{2.21}$$

The no-normal flow condition for $[U]$ and $[V]$, leads to boundary conditions for Equtaion 2.21 at the boundaries:

$$\begin{aligned} &\begin{pmatrix} [U] \\ [V] \end{pmatrix} .\mathbf{n} = \\ &\begin{pmatrix} Q^N \partial_x N + R^N \partial_y N + Q^T T^x + R^T T^y \\ -R^N \partial_x N + Q^N \partial_y N - R^T T^x + Q^T T^y \end{pmatrix} .\mathbf{n} = 0 \end{aligned} \tag{2.22}$$

Equation 2.21- 2.22 are solved numerically with a standard second order finite difference scheme on a stretched grid in order to increase resolution close to the boundaries.

2.2.2 Elongated basins

If the domain is elongated with an horizontal aspect ratio $\alpha = L_y/L_x \ll 1$, an asymptotic expansion of the solution is possible. The expansion consists

in several uses of the vertically integrated continuity equation (Eq. 2.18), the vertically integrated horizontal velocities (Eq. 2.19- 2.20) and the condition of no transport through the boundaries. The details are not repeated here because the development follows closely Winant (2007), except for the present inclusion of the wind. If the bathymetry is assumed to be uniform in the x direction, the result of the expansion is

$$\partial_x N = A^N \times \frac{\cos\left(\kappa\mu(x-1/2)\right)}{\cos(\kappa\mu/2)}, \tag{2.23}$$

$$\partial_y N = (R^T T^x - Q^T T^y + R^N \partial_x N)/Q^N, \tag{2.24}$$

at lowest order in α. A^N is given by:

$$A^N = -\frac{\langle M^{Tx}\rangle T^x + \langle M^{Ty}\rangle T^y}{\langle M^N\rangle}, \tag{2.25}$$

where $\langle\cdot\rangle$ is used for the average over the width of the basin and:

$$\mu = \delta \times \left(i\langle M^N\rangle\right)^{-1/2} \tag{2.26}$$

$$M^N = (R^N)^2/Q^N + Q^N \tag{2.27}$$

$$M^{Tx} = R^T R^N/Q^N + Q^T \tag{2.28}$$

$$M^{Ty} = -Q^T R^N/Q^N + R^T \tag{2.29}$$

Equations 2.23- 2.24 shows that $\partial_{xy} N$ is one order in α smaller than $\partial_{yy} N$, i.e. the axial sea level slope varies weakly along the width of the basin compared to the lateral sea level slope. Equation 2.24 is equivalent to imposing $[V] = 0$ at order 1 in α. The lateral transport $[V]$ is thus one order in α smaller than the axial transport $[U]$. These two facts will be routinely used throughout this chapter after a successful validation of the expansion against the 2D computation.

2.2.3 Parameters and basin choice

The goal is here to understand the response of a chosen type of basin (illustrated in the left panel of Figure 2.1) as a function of the wind stress frequency.

Following Winant (2004), a basin is selected with an Ekman depth $\delta_E = 1/6$ and a nondimensional Rossby radius of 5, i.e. a horizontally "small" basin. This is typical of a mid-latitude coastal basin of 25 km length, 25 m depth with an eddy viscosity of 10^{-3} $m^2.s^{-1}$. The basin geometry is rectangular with a horizontal aspect ratio of 1/4. The bathymetry is parabolic in the across-basin directions (Figure 2.1). The wind stress is spatially homogeneous, oscillates at the frequency σ in the along-basin/axial direction ($T^x = 1$, $T^y = 0$).

2.3 Sea level and transports

2.3.1 Sub-inertial response: $\sigma < 1$

An inspection of the sea level slopes and axial transport as a function of frequency enables assessment of the range of validity of the quasi-steady response (Figure 2.1). The latter is controlled by the decay of the lateral sea level slope and axial transport amplitude around $\sigma \sim \delta_E/4$ (indicated by the leftmost gray triangle on Figure 2.1). In contrast, the amplitude and phase of the axial sea level slope are constant over the whole subinertial frequency band. Both indicate a downwind sea level rise in phase with the wind, as in the quasi-steady case.

This departure from the quasi-steady response is best understood by first examining the mass balance involved in the quasi-steady response. The elongated basin shape requires weak lateral transport (section 2.2.2). Contributions from the local wind stress and sea level slopes have thus to balance each other in Equation 2.20. The transport driven by the local wind stress is to the right of the wind, as with a classical wind driven Ekman spiral (Figure 2.2, upper left panel). It is uniform along the central cross section over all depths larger than an Ekman depth and scales as $[V]_{T^x} = -\delta_E^2/2 \times T^x$. It is balanced in deep areas of the cross section by a lateral transport to the left of the wind induced by the downwind increase of sea level. The dynamics is geostrophic, i.e. a balance between the

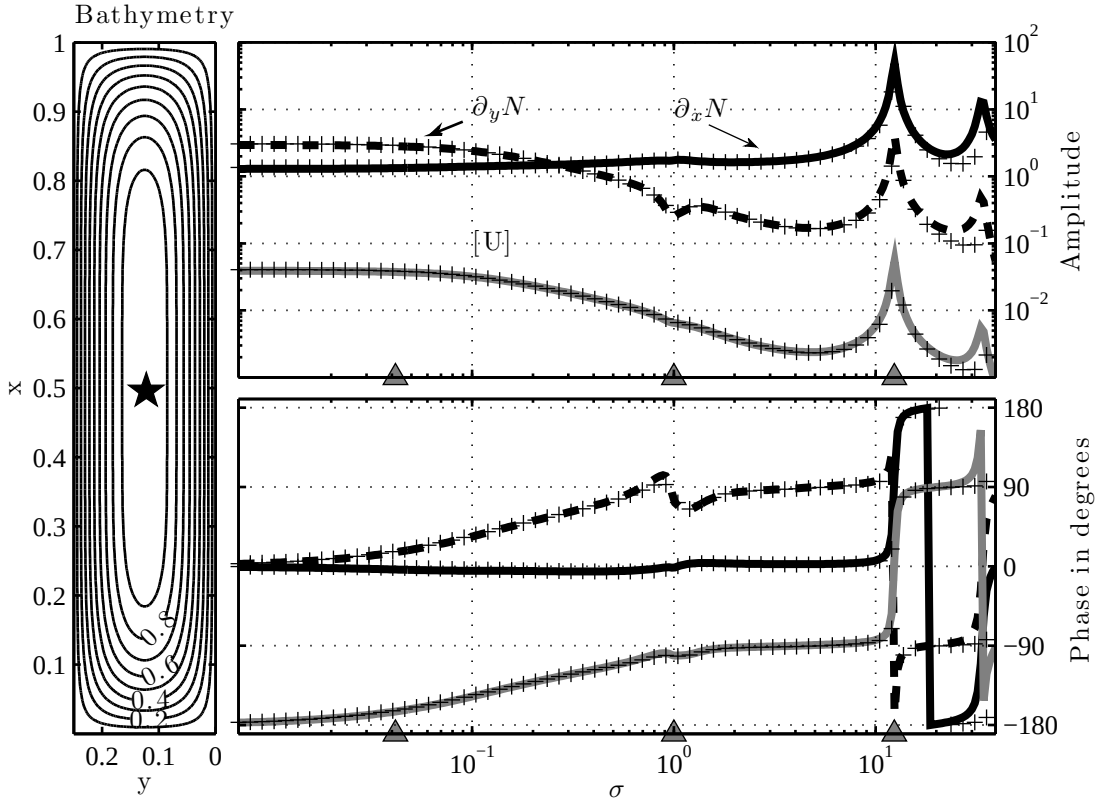

Figure 2.1: Left is the bathymetry used for the calculations. The star represents the location of the central station. The figures on the right show several variables estimated at the central location: the axial sea level slope $\partial_x N$ (full black line); the lateral sea level slope $\partial_y N$ (dashed black line); the axial transport $[U]$ (full gray line). The amplitude is on the top, and the phase at the bottom. The black crosses are the estimates of the same quantities after an asymptotic expansion in the basin horizontal aspect ration (section 2.2.2). The gray triangles mark the frequencies used in Figure 2.2: $\sigma = \delta_E/4$, 1 and $0.79\pi R$.

Coriolis force and pressure gradient, and the resulting transport scales as $[V]_{\partial_x N} = h\delta_E^2/2 \times \partial_x N$. The axial sea level required to balance the surface Ekman transport is thus of order 1. A second consequence of the elongated basin shape is that the downwind increase of sea level is nearly constant along the cross section. It is thus less effective over shallower depth because geostrophic transports are linear functions of depth. There, a lateral sea level slope helps balance the wind driven surface Ekman transport by driving a lateral transport in the bottom Ekman layer, $[V]_{\partial_y N} = -\delta_E^3/4 \times \partial_y N$.

This lateral sea level slope is the main driver of the axial circulation, downwind over shallow areas and upwind over deep ones (Figure 2.2, upper right panel). The dynamics is again geostrophic and explains the parallel evolution of lateral sea level slope and axial transport in Figure 2.1. Interestingly, the axial transport driven directly by the wind is significant only over depths shallower than an Ekman depth, where the decreased importance of the rotation of the earth allows a net downwind transport (Appendix 2.7).

For $\delta_E/4 < \sigma < 1$, the contributions of the wind stress and downwind sea level slopes to the lateral mass balance are nearly constant. The contribution of the lateral sea level slope thus also has to be constant on the shallow sides. This is possible, despite a decrease of the lateral sea level slope (Figure 2.1), because there is a spinup of the lateral flow driven by the lateral pressure gradient in the water column outside the bottom Ekman layer. The dynamical balance in the middle of the water column can be described by

$$i\sigma U + V = 0 \tag{2.30}$$

$$\frac{2i\sigma}{\delta_E^2} V - \frac{2}{\delta_E^2} U = \partial_y N \tag{2.31}$$

To first order in σ, $V \sim i\sigma\delta_E^2/2 \times \partial_y N$. If the effect of the axial sea level slope is neglected, a perfect balance between transports driven by lateral sea level slope

and wind stress leads to

$$\partial_y N = \frac{2\delta_E}{1 - 2ih\sigma/\delta_E} \times T^x \tag{2.32}$$

This explains the decrease, around $\sigma \sim \delta_E/4$, of the lateral sea level slope and the associated axial transport on Figure 2.1 and defines the range of validity of the quasi-steady response.

2.3.2 Inertial and super-inertial response: $\sigma \geq 1$

Close to the inertial frequency ($\sigma \sim 1$), there are amplitude and phase distortions of the sea level slopes and the axial transport (Figure 2.1). In depths greater than an Ekman depth, the flow driven by oscillations of sea level slope or wind stress are of order 0 in δ_E and much larger than in the quasi-steady case (see appendix 2.7):

$$([U],[V])_{\partial_{x/y}N} = \Big(-\frac{h^3}{6}(1,-i) + O(\delta_E^2)\Big) \times \partial_{x/y} N, \tag{2.33}$$

$$([U],[V])_{T^x} = \Big(\frac{h^2}{4}(1,-i) + O(\delta_E^2)\Big) \times T^x. \tag{2.34}$$

The distribution of sea level slopes which satisfies weak lateral transport $[V]$ and lateral variations of the axial slope $\partial_x N$ is such that there is a tight balance between the large transports driven by wind stress and the axial sea level slope (Figure 2.2, middle). As both contributions rotate in the cyclonic direction with time, the axial transport is weak, too. A zoom in on Figure 2.2 would show it is roughly four times weaker than in the quasi-steady case. The axial transport lags the wind stress by $\pi/2$ such that it is maximum when the wind is zero, downwind on the shallow sides and upwind at depth. The role of the lateral sea level slope is here again to maintain weak lateral transport despite the different depth dependence between the contributions driven by the axial sea level slope and the wind stress (Equation 2.33- 2.34).

For larger frequencies, $\sigma > 1$, the wavelength $2\pi/\kappa\sqrt{2}$ shortens and is eventually comparable to the size of the domain. As for the frictionless case, strong

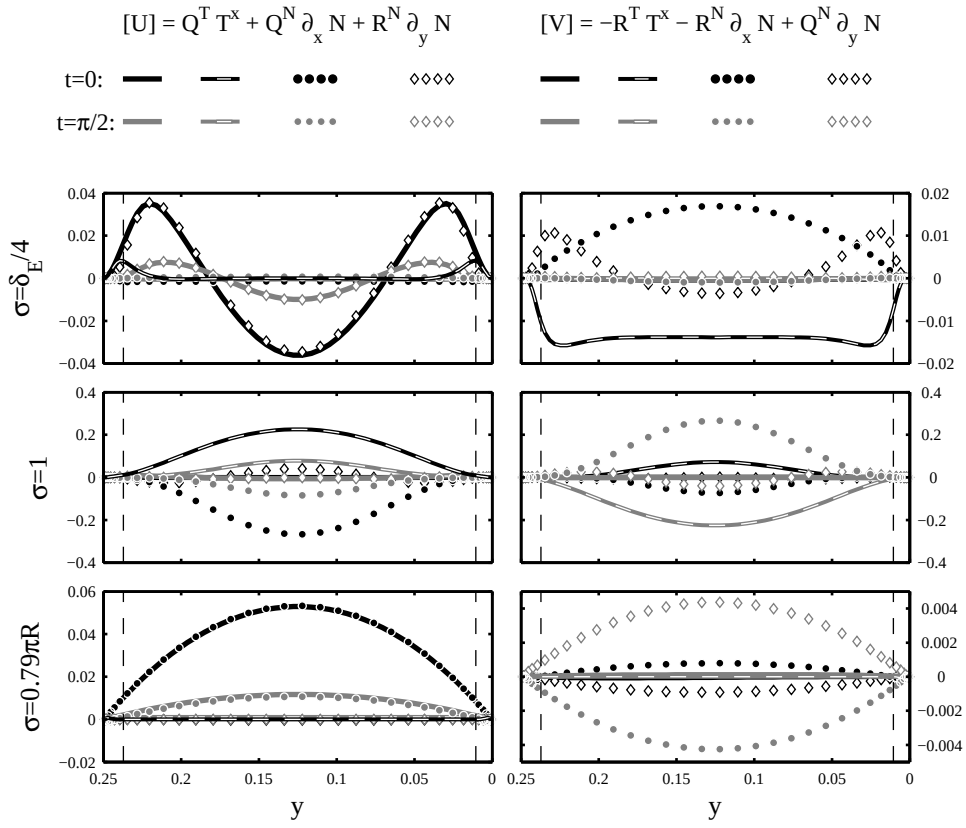

Figure 2.2: Horizontal transport ($[U]$ left, $[V]$ right) along the central cross section at selected frequencies ($\sigma = (\delta_E/4, 1, 0.79\pi R)$. Full line is the total transport, dashed, dots and diamonds are respectively local wind stress, axial and lateral sea level slope contributions (Equation 2.19 - 2.20). Black lines/symbols are at time $t = 0$, i.e. when the wind is maximum in the x direction, and gray at time $t = \pi/2$, i.e. at half period when the wind has died. The vertical dashed lines are when $h = \delta_E$.

and sharp resonances, the seiches, are then produced near $\sigma = n\pi R$, $n = 1, 2, \cdots$ (Figure 2.1). These resonances are associated with 180° change of phase of the sea level slopes and the axial transport. Their maximum amplitudes decay with increasing frequency. The axial transport is driven by the axial sea level slope oscillations and therefore mirrors the depth distribution along the cross section (Figure 2.2, bottom). The transport is roughly twice as strong as in the steady case and unidirectional. This major difference with lower frequencies is a hint that the transport is now divergent over the whole basin and that a rigid-lid approximation would no longer hold. As far as the lateral transport is concerned, contributions of the sea level slopes and wind are much weaker than for the axial transport because of the decreased effect of the rotation of the earth at super-inertial frequencies.

2.3.3 Asymptotic expansion in α

The sea level slopes and axial transport predicted by an asymptotic expansion on the basin horizontal aspect ratio (section 2.2.2) are compared with the 2D computations in Figure 2.1. Even though the aspect ratio used in the present case is 1/4, at the limit of what could be considered as a small parameter, the agreement is good up to frequencies comparable with the frequency of the second seiche. For larger frequencies, the variations of the bathymetric profiles near $x = 0$ and $x = 1$ produce shifts of the frequency of resonance. In the rest of this chapter, the 2D computations will be used even though these are more computationally expensive.

2.4 Three-dimensional velocities

2.4.1 Frequency response

The three-dimensional velocities are next examined at three locations located along the central cross section. The first one is at a side location, where

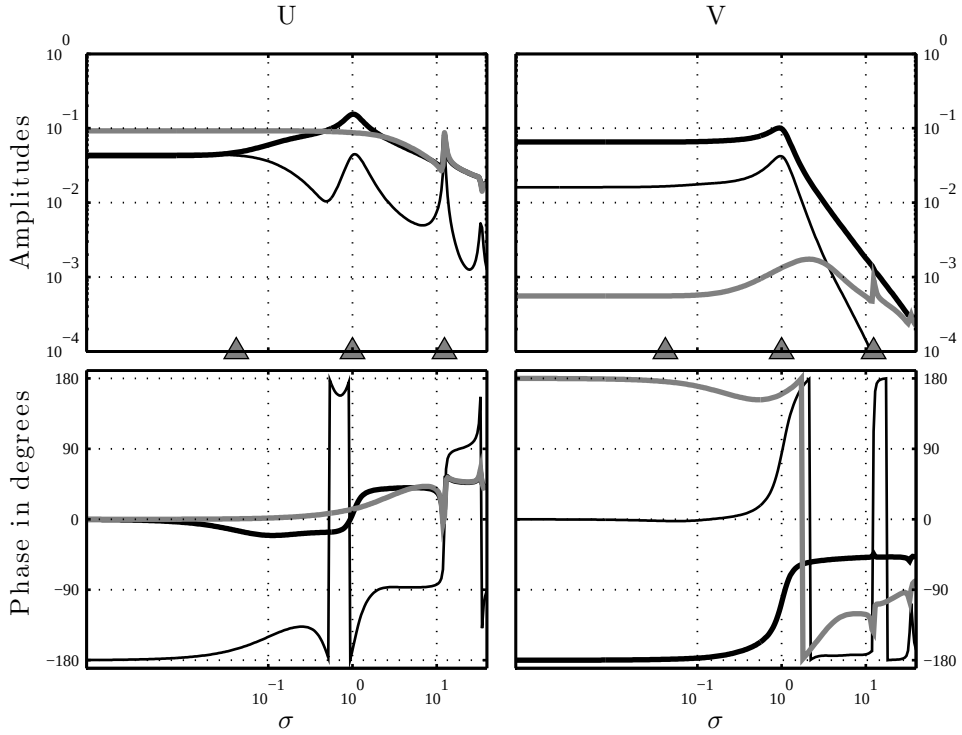

Figure 2.3: Local velocity frequency responses at three locations along the central cross section. Thick and thin black are in the center, at depth $z = 0$ and $z = -0.65$ respectively. Gray is on the side ($y = 1/8$), at $z = 0$. Amplitude is above, phase, below.

the depth $h_s = 0.1 < \delta_E$, and illustrates the response over a shallow location. The two other locations are at the surface and depth of the central location.

At the side location, the proximity of the bottom constrains the wind and sea level slopes to force currents only in their respective directions (Appendix 2.7). The wind driven current overwhelms the current driven by sea level slopes and drives a downwind current with a flat frequency response for $\sigma < \delta_E^2/h_s^2 \sim 3$, i.e. $\delta > h_s$ (Figure 2.3). At higher frequencies, the amplitude of the surface response decreases and is delayed with respect to the wind by 45°, following the high frequency approximation $u(z = 0) \sim \delta_E(1 + i)T^x/2\sigma^{1/2}$ (Eq. 2.46). At the seiche resonance, the current driven by the axial seal level slope is locally stronger than the wind driven current and produces amplifications of the surface current.

At the central location, the depth is $h_d = 1 > \delta_E$. Except for close to the inertial frequency, the direct effect of the wind stress is confined to the surface either by the effect of the rotation of the Earth at sub-inertial frequencies, or by the flow oscillations at super-inertial frequencies (Appendix 2.7). Within this surface layer, both wind stress and sea level slopes drive currents while in the rest of the water column the currents are driven by the sea level slopes only. At the surface, the low frequency response ($\sigma < \delta_E/4$) would be similar to the surface response of a classical Ekman spiral if it were not for the lateral sea level slope, which drives a current opposing the wind, as part of the overall axial circulation described in section 2.3.1. The surface flow is thus at an angle greater than $\pi/4$ to the right of the wind. With increasing frequency, the current response perpendicular to the wind is nearly flat while the axial current increases slightly, due to a weakening of the flow driven by the lateral sea level slope. At the inertial frequency, there is a damped resonance which produces maxima of the surface current in both axial and lateral directions. The axial surface current is in the downwind direction with a small phase delay (10°). The lateral current is weaker and in advance with respect to the wind stress by 105°. The current rotates in the cyclonic direction with time. As for the transport, this response is the sum of the two large and opposite

contributions of the wind and the axial sea level, the former being stronger at the surface. At superinertial frequencies, the axial current decays in the same way as at the surface current of the shallow location, whereas the lateral current decay is steeper with no seiche signature.

At the depth of the central location and at low frequency ($\sigma < \delta_E/4$), the axial current has an amplitude similar to the surface but flows in the opposite direction. It is driven by the lateral sea level slope and is part of the overall axial circulation. The lateral current is to the left of the wind driven by the axial sea level slope. With increasing frequency, the lateral response mimics the axial sea level slope and is nearly flat. In contrast, the amplitude of the axial flow decreases with a dip around $\sigma \sim 0.5$. This decrease reflects the decrease of the overall axial circulation. At the inertial frequency, the balance between the large wind and axial sea level contributions is in favor of the sea level and produces an upwind current in phase with the wind, which rotates in the cyclonic direction with time. At super-inertial frequency, the deep axial flow is driven by the axial sea level slope which has a constant amplitude but drives slower currents ($U \sim -i\delta_E^2 \partial_x N/2\sigma$). Close to the seiche resonances, however, the amplitude of the current is locally amplified and its phase undergoes 180° shifts. The lateral flow steeply decreases at subinertial frequencies, which is explained by a momentum balance between lateral momentum and Coriolis acceleration and a decrease of the axial flow amplitude ($V \sim -iU/\sigma$). There is no signature of the seiche resonances on the lateral flow.

2.4.2 Selected frequencies

The quasi-steady velocity field along the central cross section is in phase with the wind (Figure 2.4): the basin is at rest when the wind is null at $t = \pi/2$ and fully spun up when the wind is maximum. When the wind is positive in the x direction at $t = 0$, the flow is downwind on the shallow sides as described earlier. This net downwind transport is balanced by an upwind return flow in the center

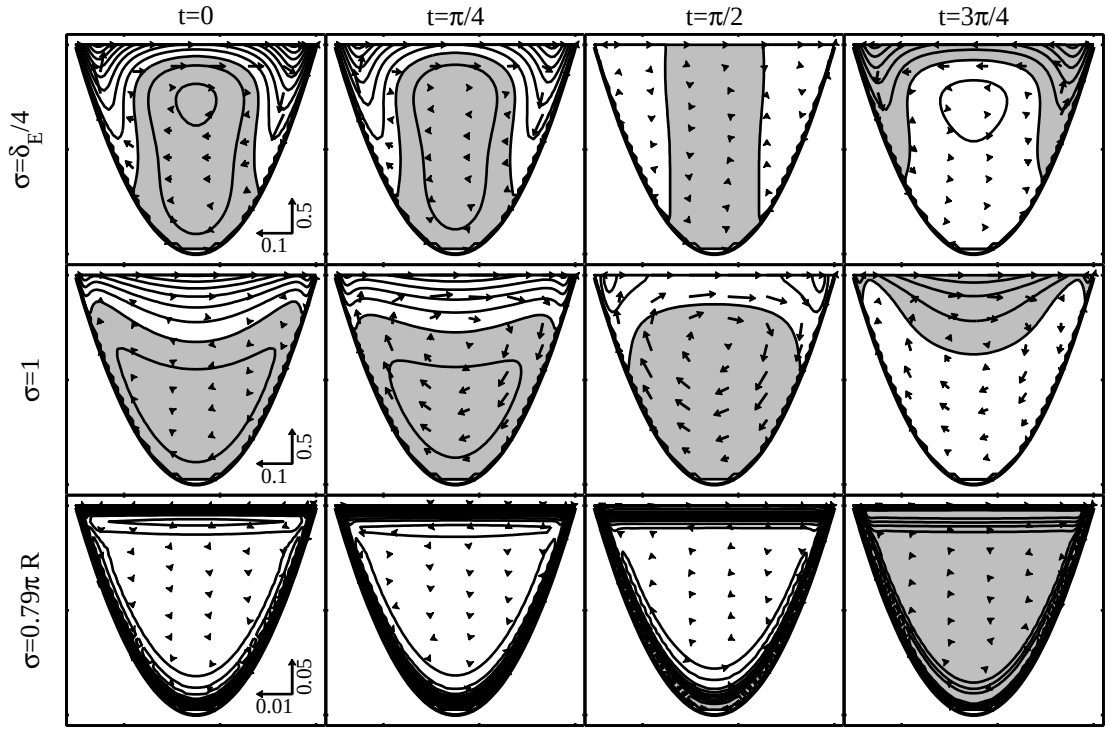

Figure 2.4: Local velocities along the central cross section as a function of depth and time. Positive x is into the page and the wind is maximum into the page when $t = 0$. Axial current is represented through the contours, spaced every 0.025 for $\sigma = (\delta_E/4, 1)$ and 0.005 for $\sigma = 0.79\pi R$. The shading is white for positive values and gray for negative values. Arrows represent lateral and vertical currents, note that the scaling changes with forcing frequency.

of the cross section driven by the lateral tilting of the sea level. There is an overall cyclonic lateral circulation which is to the right of, and driven by, the wind in the surface Ekman layer. At depth, the flow is weaker, in the opposite direction, and in geostrophic balance with the downwind increase of sea level.

At the inertial frequency and when the wind is maximum, a downwind axial flow is intensified and confined at the surface. In contrast with the quasi-steady case, it is maximum around the center of the cross section, where it penetrates deeper inside the water column. At depth, the flow is upwind and weaker than in the quasi-steady case. The vertical and lateral flow are weak. As the time increases and the wind decreases, the flow rotates in the cyclonic direction over most of the cross section. A cyclonic lateral circulation to the right of the wind at the surface and in the opposite direction at depth builds up. It is associated with downwelling on the right side of the wind and upwelling on its left side. At time $t = \pi/2$, when the wind has died, the axial flow is weak over most of the cross section except close to the shallow sides where it is in what used to be the downwind direction. The lateral cyclonic rotation is at its maximum and stronger than the lateral circulation of the quasi-steady case. Past $t = \pi/2$, the axial surface flow intensifies at the surface in the direction of the wind. The flow on the sides has however not reversed yet and is upwind compared to the current wind direction. At depth the axial flow has reversed and weakly builds up while the lateral cyclonic circulation dies out.

At the lowest seiche frequency, the flow is axial, uniform over the cross section, and in phase with the wind. Close to the surface and bottom, the flow adjusts over thin boundary layers of size δ in order to satisfy bottom and surface boundary conditions. The flow is much weaker than at lower frequencies.

2.5 Discussion

2.5.1 Higher friction: $\delta_E \geq 1$

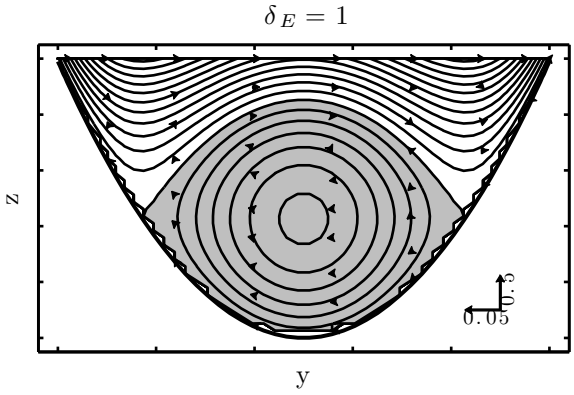

Figure 2.5: Local velocities forced by a steady wind stress along the central section for $\delta_E = 1$. Conventions are identical to Figure 2.4, with an axial velocity contours spaced every 0.025.

Higher values of the Ekman depth ($\delta_E > 1$) are typical of shallow coastal environments such as a lagoons. Values of $R = 5$ and $\delta_E = 1$ would represent, for example, a 5 m deep by 13 km long basin at mid-latitude for $K = 10^{-3}\mathrm{m}^2.\mathrm{s}^{-1}$. A more relevant set of parameters might then be the nondimensional oscillating boundary layer thickness δ and gravity wavenumber κ which do not depend on the rotation of the Earth which is unimportant in this case. For comparison and consistency purposes, (δ_E,σ,R) are kept in the following description.

At low frequencies ($\delta_E/\sqrt{\sigma} = \delta > 1$), the wind stress penetrates down to the bottom of the basin and drives a downwind current, linear with depth and maximum at the surface (Appendix 2.7). This is a major difference with the response of deeper basins, where the response is confined to the surface by the rotation of the earth. This downwind current is counterbalanced by an upwind current driven by a downwind increase of sea level. For basins with a variable bathymetry, the axial sea level slope is more effective in deep areas compared to

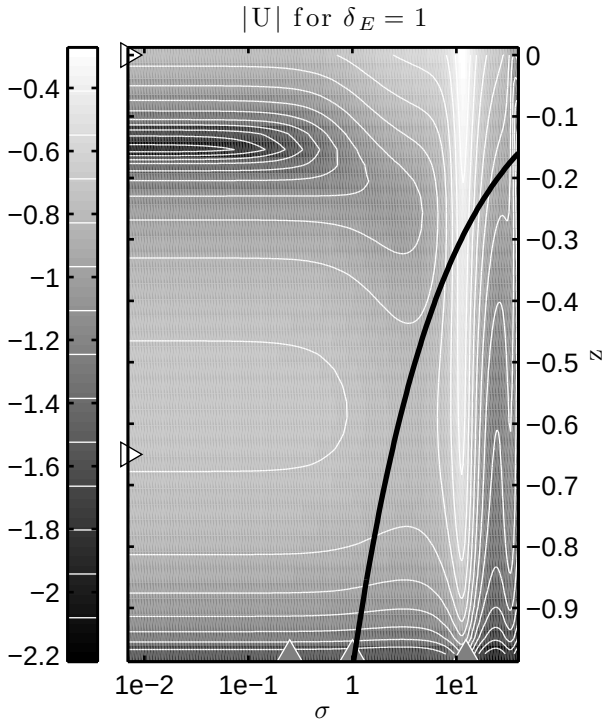

Figure 2.6: $\delta_E = 1$. Shadings and contours represent $\log_{10}$ of the amplitude of the axial flow at the central location as a function of forcing frequency (horizontal also $\log_{10}$) and depth (vertical). The full black line is $z = -\delta$. The gray diamonds indicates the usual reference frequencies and the white diamonds the reference depths used for Figure 2.3.

the wind stress because of its parabolic vertical profile. The lateral distribution of currents is thus downwind over shallow areas and upwind over deeper ones (Figure 2.5). This pattern of axial circulation is similar to the axial steady response of less frictional basins (Figure 2.4, upper left cross section). The dynamics is however different as in the less frictional case. It is the lateral sea level slope which drives the axial circulation (Section 2.3).

The frequency cutoff of this quasi-steady response is linked to the viscous time scale: $\sigma_d \sim \delta_E^2$ or equivalently $\delta \sim 1$. This is another major difference compared to the $\delta_E \ll 1$ case, for which the frequency cutoff of the quasi-steady response scales as δ_E. For $\delta_E \gg 1$, $\sigma_d \gg 1$ and the inertial frequency falls within

the quasi-steady frequency band. For $\delta_E = 1$, this cutoff frequency is also the inertial one and Figure 2.6 shows indeed a modification of the response near the inertial frequency. The friction is however already high enough to damp any inertial resonance. For frequencies larger than σ_c, the response is similar than in the less frictional case. The local wind response is confined to the surface and decreases with increasing frequency, except close to seiche resonances where it is amplified.

Shallow environments leads to larger δ_E but also smaller R (lower gravity wave speed). The propagation of the sea level signal through the basin becomes important at comparatively lower frequencies. This case was investigated by Wong and Moses-Hall (1998) and Janzen and Wong (2002) who demonstrated observationally and theoretically the propagation of low frequency sea level oscillations in long estuaries.

2.5.2 $\delta_E \ll 1$, $\sigma \ll 1$: link to quasi-geostrophy

At low forcing frequency ($\sigma \ll 1$) and low friction ($\delta_E \ll 1$), we adopt Pedlosky's (1987, Chapter 4) notation ($\epsilon_T = \sigma$,$r_T = \delta_E/\sigma$,$F = R^{-2}$) and compute a perturbation expansion of the vertically integrated profile functions assuming $\epsilon_T \ll 1$:

$$Q^N = r_T^2(ih/2 - r_T/4)\epsilon_T^3 + O(\epsilon_T^4), \tag{2.35}$$

$$R^N = -hr_T^2\epsilon_T^2/2 + O(\epsilon_T^3), \tag{2.36}$$

$$Q^T = -ir_T^2\epsilon_T^3/2 + O(\epsilon_T^5), \tag{2.37}$$

$$R^T = r_T^2\epsilon_T^2/2 + O(\epsilon_T^4). \tag{2.38}$$

The vertically integrated velocities are then at lowest order in ϵ_T

$$\begin{pmatrix} [U] \\ [V] \end{pmatrix} = h \begin{pmatrix} u_i \\ v_i \end{pmatrix} + r_T^2\epsilon_T^2/2 \begin{pmatrix} T^y \\ -T^x \end{pmatrix}, \tag{2.39}$$

where $(u_i, v_i) = r_T^2\epsilon_T^2/2(-\partial_y N, \partial_x N)$ is the velocity in the geostrophic core of the water column for which N is a scaled streamfunction. If $h = 1-\eta_b$ with $\eta_b = O(\epsilon_T)$,

Equation 2.21 becomes:

$$-i\big(\nabla^2 N - FN\big) + (\partial_x N \partial_y \eta_B - \partial_y N \partial_x \eta_B)/\epsilon_T = (\partial_y T^x - \partial_x T^y)/\epsilon_T - \frac{r_T}{2}\nabla^2 N \tag{2.40}$$

This is the linearized and time-periodic potential vorticity equation with vertical friction and variable bathymetry but in the absence of horizontal viscosity (Pedlosky (1987), Eq. (4.11.12)). This equation supports topographic Rossby waves, with the following dispersion relation:

$$\sigma = \frac{-k\gamma - i\delta_E(k^2+l^2)}{F + k^2 + l^2}, \tag{2.41}$$

with $\eta_B = \gamma \times y$ and (k, l) the nondimensional horizontal wavenumbers. The ratio of the decay rate to the wave frequency is: $\delta_E(k^2+l^2)/k\gamma$. γ is of the order of the horizontal aspect ratio of the basin, while k and l are at least of order 1. We conclude that the damping rate is significant for the ranges of δ_E we have used here, which explains that we do not observe any features which could be interpreted as topographic Rossby waves.

2.5.3 Spinup

While the results presented so far have focussed on periodic motions, they can be extended to more general transient solutions. Consider the spinup from rest of a basin forced by the onset of a spatially uniform and unidirectional wind: $\tau^x(\tilde{t}) = (1 + \tanh(10(\tilde{t}-1))/2\pi)/2$. It is convenient in this case to choose a new nondimensional time: $\tilde{t} = t^* f^* = t/\sigma$. The inertial period is then $\tilde{T}_i = 2\pi$. The solution for any variable a ($= u$, v or η) is written as:

$$a(t) = \frac{1}{\sqrt{2\pi}} \int_{-\infty}^{\infty} T^x(\omega) A^\dagger(\omega) e^{i\omega\tilde{t}} d\omega, \tag{2.42}$$

where † is the conjugate of a complex number, $A(\omega)$ is the solution found earlier for a periodic wind of unit amplitude ($e^{-i\omega\tilde{t}}$) oscillating along the x direction, and:

$$T^x(\omega) = \frac{1}{\sqrt{2\pi}} \int_{-\infty}^{\infty} e^{-i\omega\tilde{t}} \tau^x(\tilde{t}) d\tilde{t}. \tag{2.43}$$

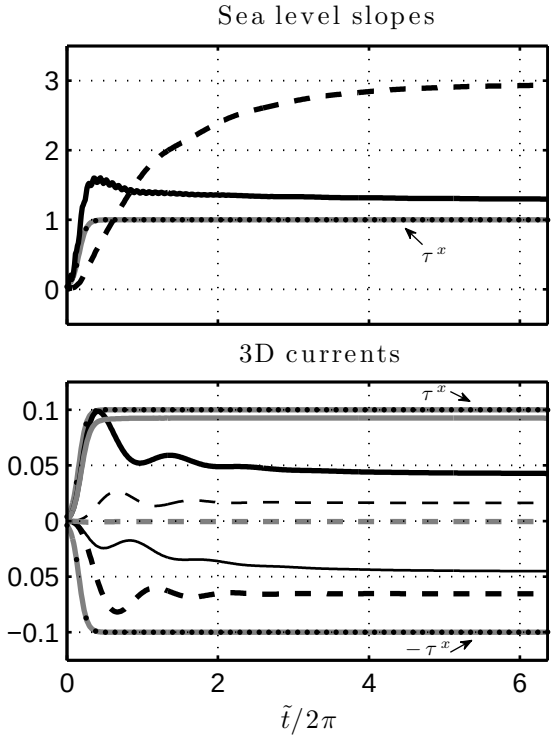

Figure 2.7: Top panel: sea level gradients $\partial_x\eta$ (full) and $\partial_y\eta$ (dashed) at the central location. The dotted line is $\tau^x(\tilde{t})$. Bottom panel: spinup of currents at the central locations and $z = (0, -0.65)$, and at the side location and $z = 0$. The line convention is similar to Figure 2.3, except that full lines are axial currents (u), and dashed lateral current (v). The dotted lines are $\pm\tau^x(\tilde{t})/10$.

The spinup of the axial sea level slope is fast and closely follows the wind stress (Figure 2.7). It is characterized by a slight overshoot of duration comparable to an inertial period and the signature of small amplitude seiche oscillations. The gravest seiche resonance has a period $\tilde{T}_{\text{seiche},0}/2\pi = 0.081$, which is too short compared to the wind stress ramp up time scale to be more significantly excited. The lateral sea level slope has a much slower spinup, of the order of several inertial periods ($\sim 1/\delta_E$). This slower spinup is associated with the early decay of the lateral sea level slope and the axial circulation described in section 2.3.1.

The spinup of the velocity at the shallow location is fast since the wind, which directly drives the flow at this location, penetrates easily to the bottom of the water column. At the central location, the spinup is characterized by inertial oscillations damped over few inertial periods. These are the superposition of nearly opposite contributions by the wind and the axial sea level slope, of larger amplitude and smaller decay rate. These oscillations are the only significant features of the lateral flow spinup. In the axial direction, these inertial oscillations also have a signature. The spinup of the axial current is however controlled by the slow setup of the axial circulation. This setup translates as a slowly building negative contribution to both surface and deep currents.

2.5.4 Semi-enclosed versus closed basins

The present model is valid inside a closed basin. When a basin is connected to the ocean, the response of the ocean needs to be included and the boundary condition at the mouth of the basin is changed. Garrett (1975) addressed a similar issue regarding tidal circulation and his ideas are adapted next in the case of the wind driven circulation. Assuming temporarily that the mouth of a semi-enclosed basin is closed, the wind stress produces separate responses inside the ocean and inside the basin. The response inside the closed basin is explained by the present chapter. The sea levels of the oceanic and basin responses differ at the

mouth. A mass flux through the mouth is required so as to balance this difference by driving secondary responses inside both domains. The secondary response inside the semi-enclosed basin is called the co-oscillating tide in the case of tidal forcing.

An illustrative example is taken by considering the effect of wind stress confined to a semi-enclosed basin. In this case, there is no direct response of the ocean. If the ocean is much deeper than the basin, as in most cases, the ocean imposes the constraint that there be no sea level oscillations at the mouth (Garrett, 1975). Inside the semi-enclosed basin, the circulation is thus the sum of the closed basin response and the circulation forced by sea level oscillations at the mouth. These sea level oscillations are such that, at the mouth, they exactly balance the sea level oscillations associated with the closed basin solution.

2.6 Summary and conclusions

The response of a closed coastal basin to a time periodic wind stress was computed with an idealized theoretical model. The selected basin was small compared to the barotropic Rossby radius of deformation, elongated in the wind direction and with a variable bathymetry. The maximum depth was chosen to be larger than an Ekman depth which allowed the influence of the rotation of the earth. Key features of the response were the weak vertically integrated velocity in the lateral direction and the weak variations of the axial sea level slope, both imposed by the basin elongated shape.

For low forcing frequencies, the direct effect of the wind stress is an Ekman layer at the surface with a net transport to the right of the wind. Over deep areas, it is balanced by the flow geostrophically driven by a downwind increase of sea level. In shallower areas, a lateral sea level slope drives in its bottom Ekman layer the transport necessary to maintain the lateral mass balance. This lateral sea level slope geostrophically forces an axial circulation, downwind on the shallow

sides and upwind in the deeper parts. This is similar to the response driven by a steady wind stress. For larger frequencies ($\sigma \sim \delta_E$), the lateral sea level slopes and associated axial circulation decrease.

Close to the inertial frequency, there is a damped resonance with a two layer flow, downwind at the surface and in the opposite direction at depth. This pattern rotates with time in the cyclonic direction. This resonance is the result of a tight balance between the direct effect of the wind stress and the axial sea level slope. Despite the large values of the three-dimensional flow, the vertically integrated velocities are small.

At super-inertial frequency, the effect of the rotation of the Earth decreases and the currents and sea level slopes are aligned with the wind direction and the basin shape. The flow is driven by the oscillations of the sea level, while the direct effect of the wind stress is confined to a thin boundary layer at the surface. There are seiche resonances where the current and sea level response are amplified.

For basins with higher friction ($\delta_E \geq 1$), there is no flow in the direction perpendicular to the wind. The quasi-steady axial circulation is similar to the case of a deeper basin but the dynamics is different. The upper frequency limit of the quasi-steady response is associated with the viscous scale: $\sigma \sim \delta_E^2$. In the low frequency - low friction limit, a QG type of dispersion relation was found governing friction damped topographic waves. By gathering a whole range of solutions in the frequency domain, it has been possible to compute the response to an onset of winds, showing how at the same time inertial and, to a lesser extent, seiche oscillations are excited. The set-up of the lateral sea level slopes and axial circulation is the slowest, consistent with the description of the response in the frequency domain. A method to extend these results to the case of a semi-enclosed basin was highlighted. This work does not address the issue of spatially uniform wind stress, realistic turbulence representation or perhaps more importantly, non-linearities.

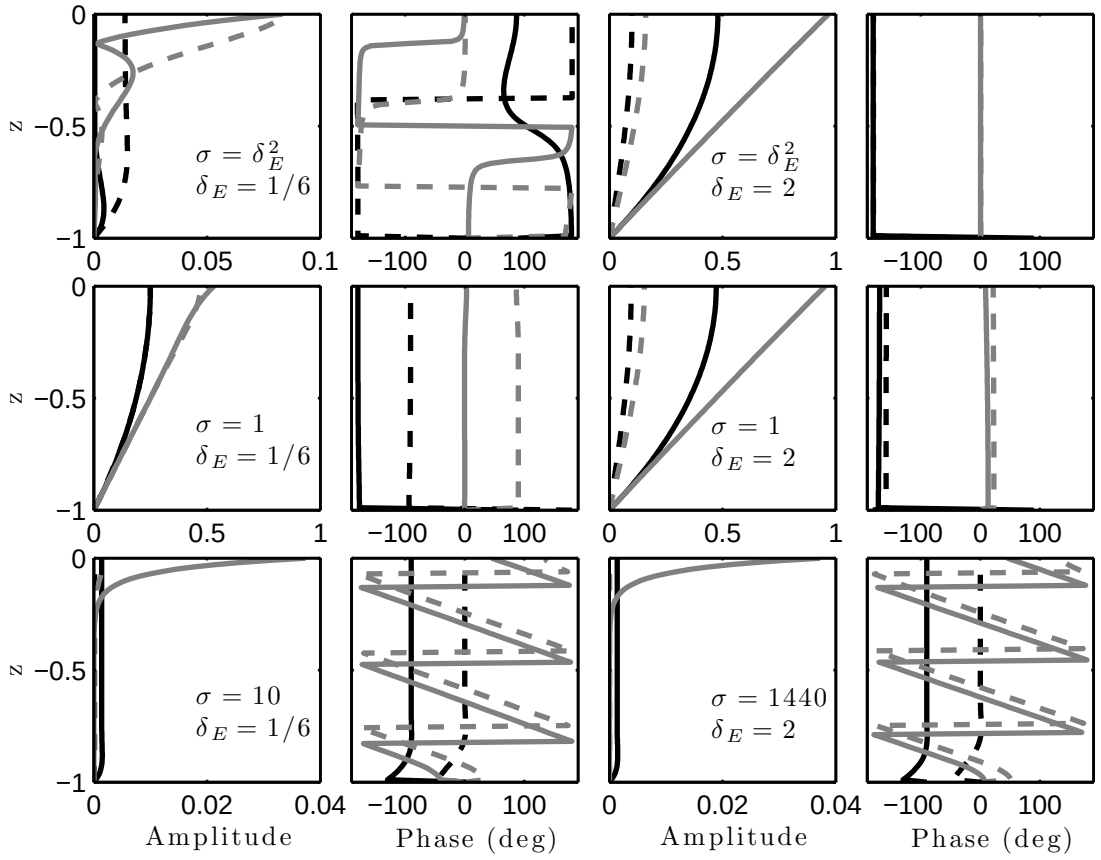

Figure 2.8: Velocity vertical profile functions for $\delta_E = 1/6$ (right) and $\delta_E = 2$ (left), and different forcing frequency σ increasing toward the bottom. The amplitude is shown on left of the phase. q^N and r^N are the full and dashed black lines. q^T and r^T are the full and dashed gray lines.

The present chapter is a reprint of the material submitted in Journal of Physical Oceanography. The dissertation author was the primary researcher and author of the published work.

2.7 Appendix: Velocity vertical profile functions and their vertical integrals

The vertical structure of the solution is fully described by the following vertical profile functions:

$$q^N = \frac{i\delta_E^2}{2}\Big(\frac{\sigma}{1-\sigma^2} + \frac{1}{2(1+\sigma)}p_+ - \frac{1}{2(1-\sigma)}p_-\Big), \tag{2.44}$$

$$r^N = \frac{\delta_E^2}{2}\Big(-\frac{1}{1-\sigma^2} + \frac{1}{2(1+\sigma)}p_+ + \frac{1}{2(1-\sigma)}p_-\Big), \tag{2.45}$$

$$q^T = \frac{1}{2}q_+ + \frac{1}{2}q_-, \tag{2.46}$$

$$r^T = -\frac{i}{2}q_+ + \frac{i}{2}q_-, \tag{2.47}$$

and,

$$p_\pm = \frac{\cos(1+i)\sqrt{\sigma \pm 1}z/\delta_E}{\cos(1+i)\sqrt{\sigma \pm 1}h/\delta_E}, \tag{2.48}$$

$$q_\pm = \frac{\delta_E}{(1+i)\sqrt{\sigma \pm 1}} \times \frac{\sin(1+i)\sqrt{\sigma \pm 1}(z+h)/\delta_E}{\cos(1+i)\sqrt{\sigma \pm 1}h/\delta_E}. \tag{2.49}$$

Similar vertical profiles have been described by Craig (1989a) and are sometimes called slope and drift current, as for example a unit sea level slope or wind stress oriented in the x direction drives a local current $(q^N, -r^N)$ or $(q^T, -r^T)$, respectively. These profiles are controlled by δ_E, the nondimensional Ekman depth, and $\sigma = \omega^*/f^* = \sqrt{\delta_E/\delta}$, the nondimensional wind forcing frequency. σ can also be interpreted as a measure of the Ekman compared to the oscillating boundary layer thickness and is a key parameter in this discussion, as the smallest of these two boundary layers governs the vertical structure of the flow. Characteristic profiles are shown in Figure 2.8 at a point of maximum depth ($h = 1$) for two values of δ_E corresponding to a deep ($\delta_E = 1/6$) and a shallow ($\delta_E = 2$) location, and three values of σ corresponding to quasi-steady, inertial and superinertial frequencies. The frequency which defines the viscous time scale ($\sigma = \delta_E^2$) is the lowest frequency chosen because it is an underestimate of the quasi-steady case inside deep and shallow basins.

In an areas deeper than the Ekman depth ($\delta_E = 1/6$, left column of Figure 2.8) and at quasi-steady frequency, the rotation of the Earth sets the structure of the vertical profiles. The sea level slope drives a current to its left quasi uniformly with depth: this is the geostrophic core of the flow. In the bottom Ekman layer the current rotates in the anticyclonic direction with depth while decreasing in strength. The current driven by the local wind is a classical Ekman layer: intensified close to the surface where it lies at a 45° angle to the right of the wind, it rotates and decays with depth over an Ekman depth. For $\delta_E \ll 1$, the net transport driven by wind stress and sea level slope are given at lowest order in δ_E by: $R^T \sim \delta_E^2/2$ and $(Q^N, R^N) \sim (-\delta_E^3/4, -h\delta_E^2/2)$. In all cases, the amplitude of the flow is maximum when the amplitude of either the wind or the sea level slope is maximum.

At the inertial frequency, the oscillations of the flow and the rotation of the Earth are resonant: both sea level slope and wind driven flow are amplified by one order of magnitude. For low values of the δ_E, the vertical profile expression is given by: $(q^N, r^N) = -(h^2 - z^2)/4 \times (1, i)$ and $(q^T, r^T) = (h + z)/2 \times (1, i)$. The no-slip condition at the bottom limits the amplitude of the resonance. The sea level slope drives a current in its opposite direction at time $t = 0$, which rotates cyclonically with time with constant strength. Its vertical profile is parabolic. The wind stress similarly drives a current in its direction at time $t = 0$, which rotates cyclonically with time and with constant strength. Its vertical profile is linear with depth. For both sea level slope and wind stress driven flow, the current is unidirectional over depth at all times. The net transport driven by wind stress and sea level slope are given at lowest order in δ_E by: $(Q^T, R^T) = h^2/4 \times (1, i)$ and $(Q^N, R^N) = -h^3/6 \times (1, i)$. This roughly scales as $1/\delta_E^2$ times more than the flow driven in the quasi-steady case.

At higher frequency ($\sigma = 10$), the oscillating boundary layer ($\delta \sim 0.05$) is now smaller than the Ekman one and controls the vertical profiles of velocity. The sea level slope drives a current in its opposite direction with a $\pi/2$ lag, constant

with depth and whose amplitude scales like $|q^N| \sim \delta^2/2$. The wind stress forces a current in its direction confined at the surface where its amplitude scales as $|q^T| \sim \delta/\sqrt{2}$ and with a lag increasing linearly with depth. No current is forced perpendicular to the sea slope or the wind stress as $r^N = O(1/\sigma)$ and $r^T = O(1/\sigma)$ for small δ_E.

In shallower waters ($\delta_E = 2$, right column of Figure 2.8), the quasi-steady vertical profiles are significantly modified by the larger value of the Ekman depth. The sea level slope drives a current roughly in its opposite direction with no lag. The vertical profile of the amplitude is parabolic and maximum at the surface. The wind stress drives a current approximatively in its direction, maximum at the surface and decaying linearly with depth. A smaller current is driven perpendicular to a sea level slope or wind stress. The following approximation holds for $|\sqrt{\sigma \pm 1}/\delta_E| \ll 1$: $(q^N, r^N) = (z^2 - h^2)/2 \times (1, 0) + O(1/\delta_E)$ and $(q^T, r^T) = (z+h)/\times(1,0)+O(1/\delta_E)$. At the inertial frequency, the vertical profiles are similar to the quasi-steady case and there is no inertial resonance. $\sigma = 10$ has been chosen because it leads to an oscillating boundary layer thickness δ similar to the bottom left corner of Figure 2.8. The velocity profiles are then identical to $\delta_E = 1/6$ and $\sigma = 10$ but the forcing frequency required to do so is much higher.

2.7.1 Vertical integrals of the profile functions

The vertical integral of the profile functions are given by:

$$\begin{aligned} Q^N =& \frac{i\delta_E^2}{2}\Big(\frac{h\sigma}{1-\sigma^2} + \frac{\delta_E \tan((1+i)\sqrt{\sigma+1}h/\delta_E)}{2(1+i)(\sigma+1)^{3/2}} \\ &+ \frac{\delta_E \tan((1+i)\sqrt{\sigma-1}h/\delta_E)}{2(1+i)(\sigma-1)^{3/2}}\Big), \end{aligned} \tag{2.50}$$

$$\begin{aligned} R^N =& \frac{\delta_E^2}{2}\Big(\frac{-h}{1-\sigma^2} + \frac{\delta_E \tan((1+i)\sqrt{\sigma+1}h/\delta_E)}{2(1+i)(\sigma+1)^{3/2}} \\ &- \frac{\delta_E \tan((1+i)\sqrt{\sigma-1}h/\delta_E)}{2(1+i)(\sigma-1)^{3/2}}\Big), \end{aligned} \tag{2.51}$$

$$\begin{aligned} Q^T =& \frac{-i\delta_E^2}{2}\Big(\frac{\sigma}{1-\sigma^2} + \frac{1/2}{(\sigma+1)\cos((1+i)\sqrt{\sigma+1}h/\delta_E)} \\ &+ \frac{1/2}{(\sigma-1)\cos((1+i)\sqrt{\sigma-1}h/\delta_E)}\Big), \end{aligned} \tag{2.52}$$

$$\begin{aligned} R^T =& \frac{\delta_E^2}{2}\Big(\frac{1}{1-\sigma^2} - \frac{1/2}{(\sigma+1)\cos((1+i)\sqrt{\sigma+1}h/\delta_E)} \\ &+ \frac{1/2}{(\sigma-1)\cos((1+i)\sqrt{\sigma-1}h/\delta_E)}\Big). \end{aligned} \tag{2.53}$$

3

Observations at sub-inertial frequencies

3.1 Introduction

This chapter investigates the observed low frequency (periods longer than one day) dynamics in BC during the well-mixed season (November 2004 to March 2005). The goal is to test results from steady theoretical and numerical models of the wind driven circulation in a coastal basin such as BC (Winant, 2004; Sanay and Valle-Levinson, 2005). These models explain how the wind driven circulation depends on the ratio of the Ekman depth to the water depth: $\delta_E = \sqrt{2K/fH}$, where K is the eddy viscosity, f is the Coriolis frequency and H is the depth of the coastal basin. For shallow basins ($\delta_E > 1$), the direct effect of the wind stress penetrates throughout the water column and drives a downwind Couette type flow ($u_{\text{surface}} = h\tau_{\text{wind}}/K$, h being the local depth and τ_{wind} the wind stress). The indirect effect of the wind stress is due to the development of sea level gradients required to maintain no flow through the basin boundaries. In the present case, an increase of sea level in the downwind direction drives an upwind flow. In a constant depth basin, the flow is downwind at the surface and upwind at depth, because the

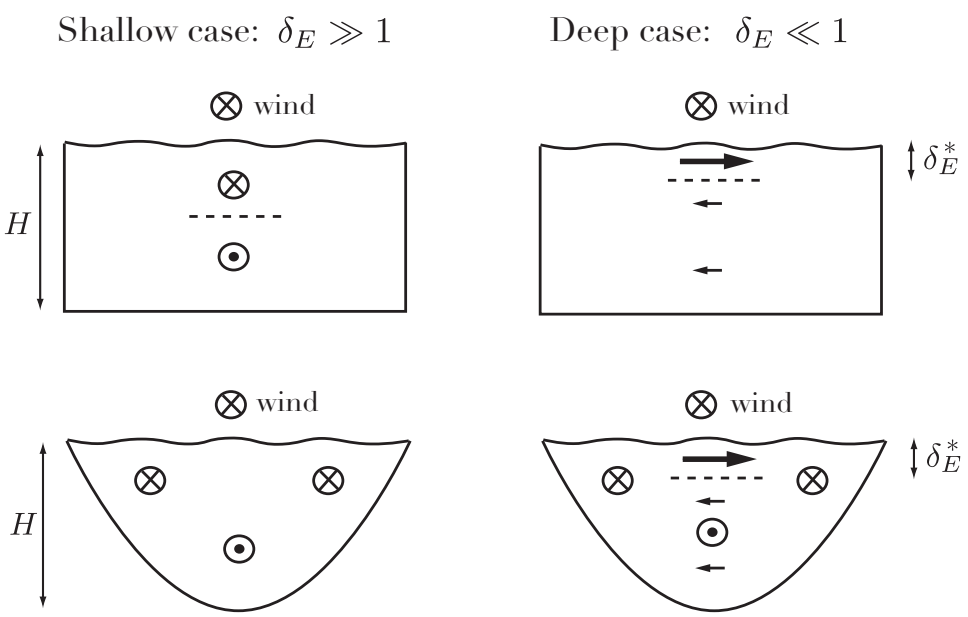

Figure 3.1: Schematic of the theoretical circulation (Winant, 2004) driven by an along basin wind stress blowing over shallow (left) and deep (right) basin, without (top) or with (bottom) bathymetric variations. The dimensional Ekman depth is $\delta_E^* = \sqrt{K/f} = \delta_E \times H$, where K is the turbulent eddy viscosity and f the Coriolis frequency.

direct effect of the wind stress dominates over the sea level at the surface (Figure 3.1). With variable bathymetry, the wind stress dominates over shallow areas with a net downwind transport. It is balanced by the sea level driven upwind flow over deeper areas.

For deep basins ($\delta_E < 1$), the direct effect of the wind stress is to produce a surface Ekman layer (Figure 3.1). It is confined to the surface and drives a transport to the right of the wind. An increase of the sea level in the downwind direction drives a depth uniform geostrophic flow to the left of the wind, balancing mass in the direction perpendicular to the wind stress. There is therefore a clockwise lateral circulation when looking at a vertical section in the downwind direction. With variable bathymetry, the situation is more complicated with development of lateral pressure gradients and an associated circulation downwind over shallow

areas and upwind over deep areas. Note that both models (Winant, 2004; Sanay and Valle-Levinson, 2005) consider well-mixed cases. The Asymmetric Circulation in Wind-Driven Bays project aimed at providing observational evidence for the case of a coastal basin deeper than an Ekman depth.

Observing the wind driven response inside a deep coastal basin consists partly in observing an Ekman layer structure. In deep water, observations of surface Ekman layers have only been possible in the last thirty years, when measurement problems and signal-to-noise issues were overcome (Rudnick, 2003). Deploying near surface instruments is technically difficult and current measurements have been made possible with the development of Vector Measuring Current Meter (VMCM) and, later on, of ADCPs. The current directly forced by the wind is often smaller than the ambient noise due to geostrophic flows at low frequencies or internal and inertial waves at higher frequencies. The first modern observations was obtained during the MILE experiment (Davis et al., 1981a;b). Subsequent experiments were the LOTUS (Price et al., 1987), FASINEX (Weller et al., 1991) and EBC experiments (Chereskin, 1995). All these observations were collected in deep areas, i.e. where surface and bottom boundary layers are well separated. The studies report on the difficulty of extracting the current forced directly by the wind, especially because large scale flows indirectly driven by the wind are correlated with the local response (Weller et al., 1991). Once this issues were overcome, the Ekman transport is found to be to the right of the wind, with an amplitude close to that given by classical Ekman theory. Ekman spirals are observed but they are usually flatter than in the constant eddy viscosity case, meaning that the current rotates faster than it decays with depth. Vertical stratification of density is most often believed to be responsible for these discrepancies, because it modulates vertical transfers of momentum (Price and Sundermeyer, 1999). Other mechanisms of possible importance are the decay of eddy viscosity close to the surface due to the presence of a physical boundary (Madsen, 1977), surface gravity waves (Polton et al., 2005), or the effect of the non-traditional components of the

Coriolis acceleration (proportional to the cosine of the latitude) (Zikanov et al., 2003; McWilliams and Huckle, 2006).

BC has a depth typical of inner shelves, that part of the continental shelf off-shore of the surf-zone, where the surface and bottom boundary layers interact, i.e. $\delta_E \sim 1$ (Lentz, 1994). Off shore of the inner shelf, generally with $H > 30$ m, the direct effect of the wind is confined to the surface Ekman layer, which is thin compared to the total depth as in the deep case just described. Because of the presence of a coastal boundary, this effect is balanced by a flow in the core of the water column or in a bottom Ekman layer (Hickey, 1998; Smith, 1995). Over the inner shelf the coupling of the bottom and surface layers produces a cross-shelf divergence of the Ekman transport. Lentz (2001); Kirincich et al. (2005) estimate that the cross-wind transport is 100% of the full Ekman transport at 50 m depth and 25% at 15 m depth. This divergence is responsible for upwelling or downwelling, making the inner shelf a key location for the whole shelf dynamics (Allen et al., 1995; Allen and Newberger, 1996; Austin and Lentz, 2002). It is still now the subject of active research (Lentz, 2001; Austin and Lentz, 2002; Tilburg, 2003; Garvine, 2004; Kirincich et al., 2005; Kirincich and Barth, 2009; Fewings et al., 2008).

An issue of major importance is the role played by vertical stratification. As in the deep case, vertical stratification of density modulates vertical turbulent transfers of momentum. Weak stratification enables larger vertical turbulent transfers of momentum (larger K), a deeper Ekman depth and dynamics similar to shallow areas with weaker transport in the direction perpendicular to the wind. Larger stratification separates bottom and surface boundary layers and the dynamics is then closer to those of deep domains, with Ekman type surface and bottom layers. The location of the inner shelf offshore boundary thus varies in time with the stratification. This has been observed by Lentz (2001), Kirincich et al. (2005), Kirincich and Barth (2009), and modeled by Austin and Lentz (2002). A second consequence of the presence of stratification is the possibility to develop horizon-

tal baroclinic density gradients as soon as vertical motions are present. This is a potential feedback on the evolution of momentum, which can be important.

In this chapter, the low frequency sea level is first compared to the low frequency wind stress. The analysis of the wind driven response is limited to the ADCPs deployed close to the BC central cross-section (ADCP E and C during deployment 1; ADCP 1 to 6 during deployment 3). Extraction of the wind driven response is achieved by first computing an EOF decomposition and then a regression between each EOF time series and the wind. The advantage of this method is that it enables one to search for a relationship between the dominant modes of variability coherent among all ADCP bins. A disadvantage is that the wind driven response is projected onto several EOFs. Momentum balances and thermal wind relationships are also discussed.

3.2 Along-bay pressure gradients and bottom pressure

In an elongated coastal basin, Winant (2004) theoretically predicts that the locally generated wind-driven flow is balanced by an increase of sea level in the downwind direction. This is expressed by the following depth-integrated along-bay / downwind momentum balance:

$$0 = -h\partial_x P^s + \tau_s^x \tag{3.1}$$

P^s is the pressure due to sea level and atmospheric variations, h is the water depth and τ_s^x is the along-bay wind stress. The horizontal gradient of P^s is estimated from observations at the south and north bottom pressure sensors. The distance between both instruments is approximated by 40 km and the depth by 20 m. A number of terms are ignored in Equation 3.1. The response is assumed steady. The depth-averaged flow in the cross-bay direction and the associated Coriolis acceleration are neglected. This is justified by the elongated nature of the domain (see chapter

2). The bottom stress is assumed to be small (Winant, 2004). Baroclinic pressure gradients (see section 3.4) and nonlinearities have also been ignored. The shoaling of surface waves at the south bottom pressure sensor is neglected as it is expected to produce a decrease of sea level of the order of 1 mm (Bowen et al., 1968) for typical wave conditions (50 cm wave height, 3 s period, Caliskan and Valle-Levinson (2008)).

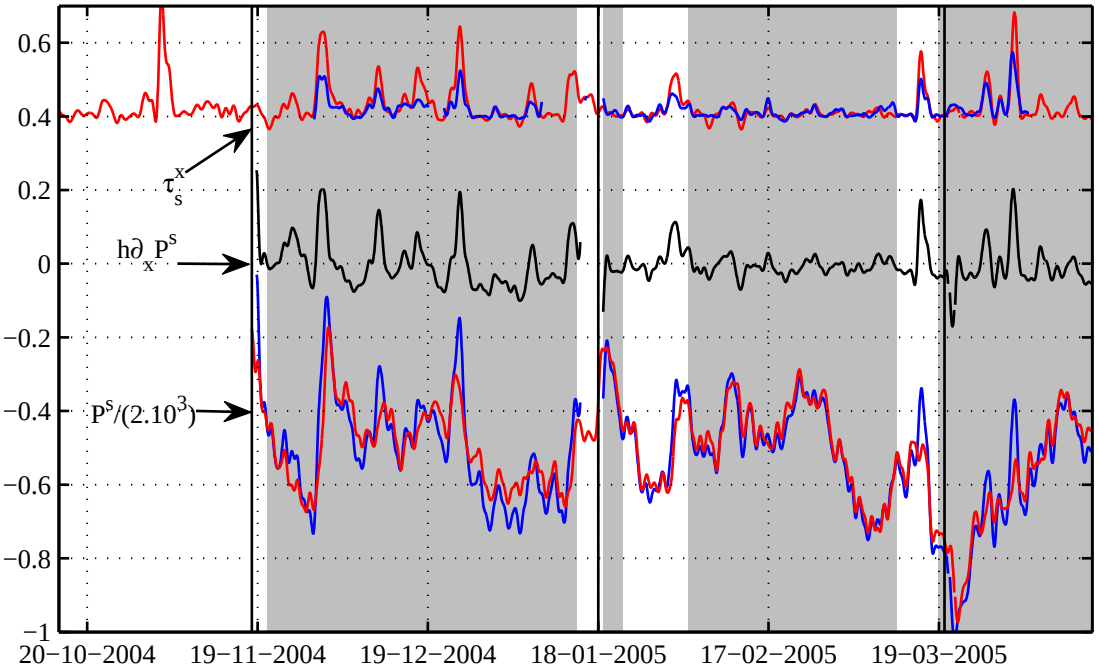

Figure 3.2: Low-passed pressure-wind stress relationship. The top two curves are the along-bay wind stress at the North (red) and South (blue) meteorological stations, offset by 0.4. The black line below is the difference of bottom pressure between South and North pressure sensors scaled by the depth $h = 20$ m. The lowest two curves are the scaled pressure measured at the North (red) and South (blue) pressure sensors, offset by -0.4. The vertical black lines indicate pressure sensor turnovers and the gray shading indicates time periods when all ADCPs were deployed.

The low-pass filtered along-bay difference of pressure between the South and North pressure sensors is well correlated with the wind stress at the North and South stations (Figure 3.2). This correlation is quantified in Table 3.1. The slope of a linear regression between both terms of Equation 3.1 shows that estimating BC bathymetry as 20 m deep and 40 km long is a reasonable choice. Note that any ratio of $h/L = 20$ m/40 km works as well. The slope is larger when the wind stress at the south station is used, which is explained by the weaker amplitude of the wind stress at the south during low frequency wind events (chapter 1).

Bottom pressure measurements are shown on Figure 3.2 and their relationship with the wind stress investigated in Table 3.1. The north bottom pressure is not significantly correlated with the wind at both meteorological stations. Merrifield and Winant (1989) similarly observed a lack of correlation between sea level and local winds. They found a 1% contribution of the local wind to the low frequency sea level variance, which is similar to what is found here. Most of the low frequency signal was attributed to propagating coastal-trapped waves or steric adjustments. The inability to eliminate the atmospheric contribution from bottom pressure time series also contributes to the low correlation. This atmospheric contribution is expected to be small in the difference of pressure between South and North pressure sensors. The larger correlation between the south bottom pressure and the local winds is explained by the local dynamics and is related to the correlation between the along-bay sea level pressure gradient and the winds. High-pass filtering the time series in order to remove long-term trends, which are probably of atmospheric origin, increases the correlation up to 0.22 for the north pressure sensor (which is barely significant), and up to 0.55 at the south station. The low frequency pressure signal could propagate inside BC and produce currents, but its amplitude turns out to be small. A 0.5 cpd pressure oscillation of 10^3 Pa, equivalent to a sea level change of 10 cm, produces for example a current weaker than 1 mm/s in a bay 40 km long by 30 m deep. This current decreases toward the closed end of the bay. This is much less than both instrument resolution and the

Table 3.1: Regression between the along-bay pressure gradient, the pressure at the North and South station and the wind stress at the North and South station. The regression is computed over the time period 20/11/2004 to 15/04/2005. A correlation r of 0.19 is significant at a 95% level.

	τ_s^x North			τ_s^x South		
	r	slope	intercept	r	slope	intercept
$h\partial_x P^s$	0.85	0.97	-2.77×10^{-2}	0.86	1.75	-3.65×10^{-2}
P^s North station	0.14	0.08	-4.55×10^{-3}	0.07	0.07	-5.57×10^{-3}
P^s South station	0.43	0.27	-1.10×10^{-2}	0.35	0.41	-1.29×10^{-2}

typical amplitudes of observed currents.

3.3 EOF analysis for currents

In this section, wind driven currents are extracted for ADCP deployments 1 and 3. A complex EOF calculation is first performed on the low frequency currents (Emery and Thomson, 2001). A description of the spatial structure of each EOF is given next. The complex time series ($\phi_j(t)$ for the jth EOF) quantify the EOF contributions to the observed flow as a function of time (Appendix 3.8). At any given time t, the jth EOF has its amplitude scaled by the absolute value of the time series, $|\phi_j(t)|$, and is rotated by the complex angle of the time series, $\arg(\phi_j(t))$. I then decompose the EOF time series into real and imaginary parts and relate each to the lagged wind stress and tidal envelope time series using a least squares regression (Appendix 3.8). For several lags when the wind stress contribution is significant at a 10% level, the wind driven currents predicted from this regression are compared with theoretical predictions. Several different EOFs can therefore contribute to the observed wind driven current.

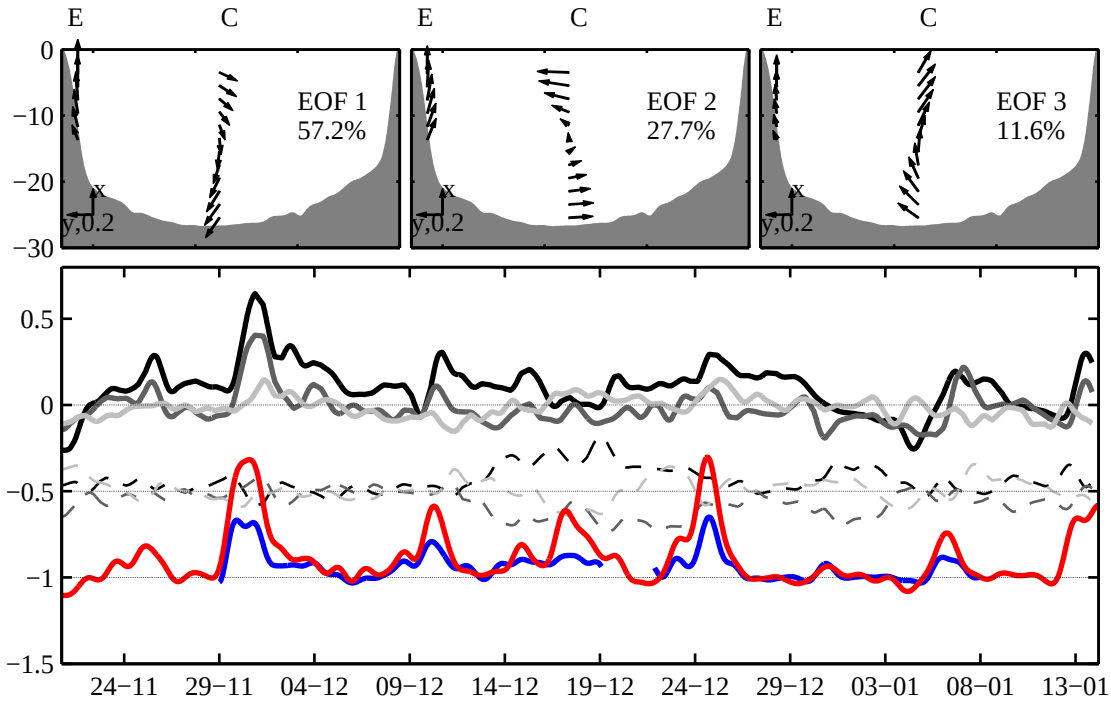

Figure 3.3: Deployment 1, ADCP location C and E. Top figures show the spatial structure of the low-passed currents' first three EOFs. The readers is looking toward the closed end of BC. Note that upward arrows are in the x direction, positive toward the closed end of BC. The bottom axis shows the associated time series: black is EOF1, dark gray EOF2, and light gray EOF3. The full thick line is the real part, the dashed lines the imaginary part centered around -0.5. Centered around -1 is the low-passed along-bay wind stress (times 4) at the north (red) and south (blue) meteorological stations.

3.3.1 Deployment 1

Only ADCP C and E are available for analysis. The EOF decomposition captures 96.5% of the variance in its first three EOFs (57.2%, 27.7%, and 11.6%, respectively). For the first two EOFs, the flow at location E is toward the closed end of the bay (Figure 3.3). It is intensified at the surface for EOF 1 and at depth for EOF 2. There is slight rotation with depth, counter-clockwise for EOF 1 and

clockwise for EOF 2. At location C, EOF 1 is toward the mouth of BC, opposite to the flow at location E, and rotates clockwise with depth, such that there is a cross-bay flow toward the western shore of BC in the upper 15 m and in the opposite direction at depth. EOF 2 is sheared at location C, toward the eastern shore in the upper 15 m and in the opposite direction at depth. EOF 3 is weak toward the closed end of BC at both ADCP locations with a counterclockwise rotation with depth at location E.

For EOF 1 and 2, the real parts of the time series' appear to be positively correlated with each other and with the wind stress (Figure 3.3). This is possible despite the normality of the complex time series because the imaginary parts of EOF 1 and 2 time series are negatively correlated. Given EOF 1 and 2 spatial structures, the correlation of the real parts cancels the cross-bay spatial structures and produces a predominantly along-bay circulation. The imaginary parts of EOF 1 and 2 are large from the 12/12 to 25/12 and 27/12 to 4/01 and negatively correlated. The cross-bay components of each EOFs are similar once rotated by $\pi/2$ (EOF 1) and $-\pi/2$ (EOF 2) and represent a current toward the closed end of BC at the surface and in the opposite direction at depth.

For deployment, I computed a least squares regression of the EOF time series by the lagged wind stress along with the semi-diurnal tidal envelope of the sea level. The tidal envelope is estimated as the absolute value of the sum of the tidal sea level with semi-diurnal constituents only and the tidal sea level with semi-diurnal constituents phase shifted by 90° times i. The diurnal tidal envelope does not significantly improve the regression and is therefore discarded from the explanatory variables. The skill of the regression indicates that a significant amount of variance of EOF 1 and 2 real time series is explained by the regression at lags lower than 30 h (Figure 3.4). The skill peaks at 12 h lag for both EOF 1 and 2. Based on its low p-values, the wind stress is responsible for the explained variance. The regression does not explain the EOF 1 and 2 imaginary time series at a significant level. The related low-frequency currents from the 12/12 to 25/12

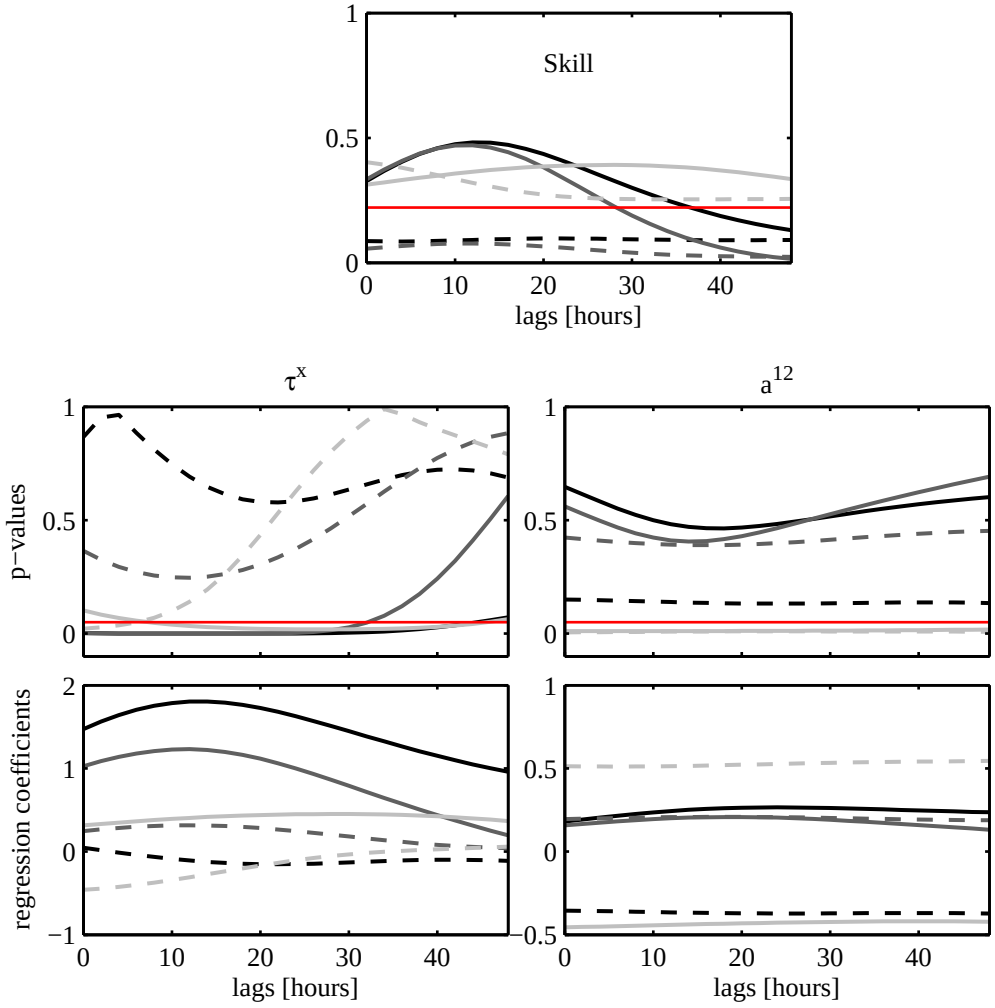

Figure 3.4: Significance of a least squares regression between the lagged wind stress (τ^x) and semi-diurnal tidal envelope (a^{12}) and the first three EOFs (1 black, 2 dark gray, 3 light gray) real (solid) and imaginary (dashed) time series. The skill of the regression is shown on the top figure. The red line shows the critical skill (95% level). The p-values of wind stress (right) and semi-diurnal tide envelope (left) are at the center. The red line is at the 5% level. The associated regression coefficients are on the bottom figures.

and 27/12 to 4/01 are thus most likely due to an independent mechanism not present in our choice of explanatory variables. A likely candidate would be related to horizontal density gradients. The semi-diurnal tide significantly explains EOF 3, both real and imaginary parts. At spring tides, the resulting current is toward the mouth of BC at the surface and toward the western side of BC at depth. The wind does explain some of the variance of EOF 3's real part at large lags, around 30 h.

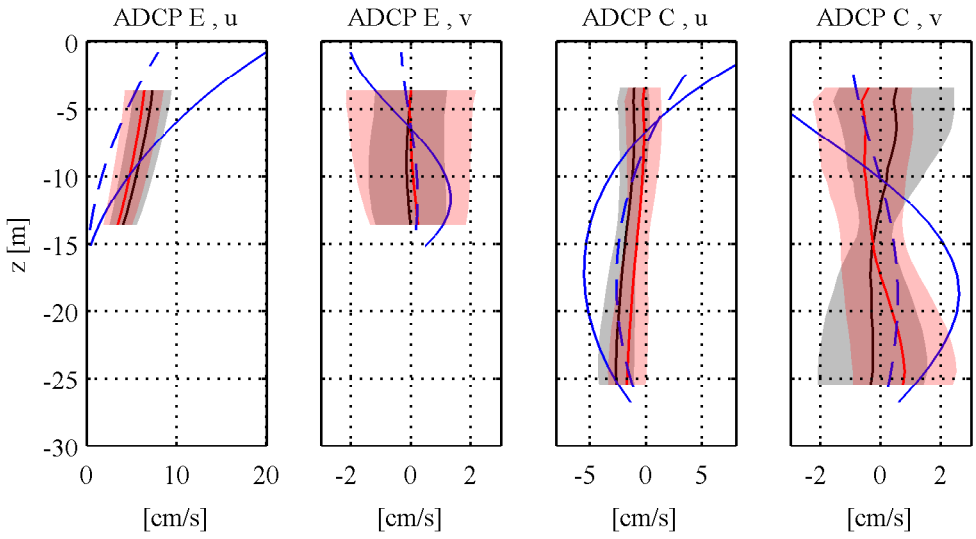

Figure 3.5: Observed wind driven current ($\tau^x = 0.1$ Pa) for 12 h lag (black, gray shading) and 30h lags (red, red shading). The shading indicates bootstrap 10% confidence intervals. The blue curves are the theoretical currents with turbulent eddy viscosity $K_1 = 10^{-2}$ m^2/s (dashed) and $K_2 = 4.10^{-3}$ m^2/s (full).

Given the significance of these regressions, we choose to focus on the wind driven flow at 12 h and 30 h lags. For both lags, the EOFs with wind stress p-values below the 10% level, are multiplied by their associated regression coefficient and summed. The result is multiplied by a wind stress value of 0.1Pa and shown on Figure 3.5. It is compared with the theoretical predictions of chapter 2 for a steady along-bay wind stress of 0.1 Pa and turbulent eddy viscosities $K_1 = 10^{-2}$

and $K_2 = 4.10^{-3}$ m^2/s.

At location E, the observed wind driven current is downwind, intensified toward the surface, with values of 6 cm/s at 12 h lag. The vertical structure is similar at 30 h lag but the flow is weaker by roughly 2 cm/s. The amplitude of the observed currents is within the theoretical values for K_1 (lower bound) and K_2 (upper bound). The vertical shear is higher in the theoretical case, with low values of the current at depth imposed by the no slip boundary condition. In the cross-bay direction, the observed current is weak and similar to K_1. K_2's weak value enables a larger cross-wind circulation, which barely fall inside the observation confidence interval.

At location C, the observed along-bay current is downwind, intensified at depth for 12 h lag. At 30 h lag, the along-bay current is weaker, such that the direction of the current is not significantly different from zero. The deep upwind current is consistent with the theoretical predictions, even though the theoretical currents are larger. The high value of K_1 and the resulting decreased along-bay flow is within the confidence intervals of the observed current at 12 h lag, which is not the case for K_2. The surface downwind current predicted from the theoretical model is not observed. The observed sense of the cross-bay circulation is opposite at 12 h lag and similar at 30 h lag to the theoretical one. The confidence intervals are large, however, such that the theoretical prediction with K_1 is at their edge at lag 12 h and within them at 30 h lag. K_1 predicts a cross-bay circulation which seems too large in view of the observations.

3.3.2 Deployment 3

The EOF analysis for currents at ADCP 1 to 7 captures 92.1% of the variance in the first three EOFs during deployment 3 (82.7%, 5.7%, and 4.1% respectively).

The first EOF, which largely dominates, is sheared horizontally with an

opposite sense of circulation between ADCP 1/2/3 and ADCP 5/6 (Figure 3.6). It is more strongly surface intensified along the western shore than on the eastern one. The associated time series is predominantly real, positive at all times, representing a cyclonic horizontal circulation aligned with the along basin direction. The second EOF represents a much smaller percentage of the total kinetic energy (5.8%). The associated time series' real and imaginary parts have alternating sign. The circulation is stronger at the three central ADCPs, in the cross-basin direction and in the upper 20m of the water column. The third mode represents a similar amount of the total kinetic energy (4.4%). The amplitude of the spatial structure is largest at all ADCPs with depth greater than 20m. The flow is sheared vertically there, such that mass is balanced at individual ADCP locations. There is no clear sense of rotation with depth.

As for deployment 1, a linear regression between the EOF time series and the lagged wind stress and tidal envelopes (semi-diurnal *and* diurnal this time) has been computed. The dominant flow pattern, which corresponds to the real part of EOF 1's time series, is to some extent explained by the regression, with a peak skill of 0.19, right at the 95% critical level, at 0 lag (Figure 3.7). The corresponding p-value of the wind stress indicates the wind stress explains the real part of EOF 1's time series. The imaginary part of EOF 1's time series is significantly explained by a combination of wind and semi-diurnal tide. Its skill peaks at a lag of 8 h. The real part of EOF 2 is well explained by the tidal envelopes. The correlation translates into an eastward flow at the center of the channel during spring tides, which remains to be understood. The real part of EOF 3 is well explained by the wind stress with a peak skill at lag 2 h.

The observed wind driven currents are again obtained from the EOF-wind stress significant regression coefficients. These currents do not change qualitatively for choices of lags between 0 and 10 h. A lag of 0 h is chosen here because there is a maximum of skill for EOF 1 and 3's real part for this lag. As for deployment 1, the EOFs with wind stress p-value less than 10% are multiplied by the associated

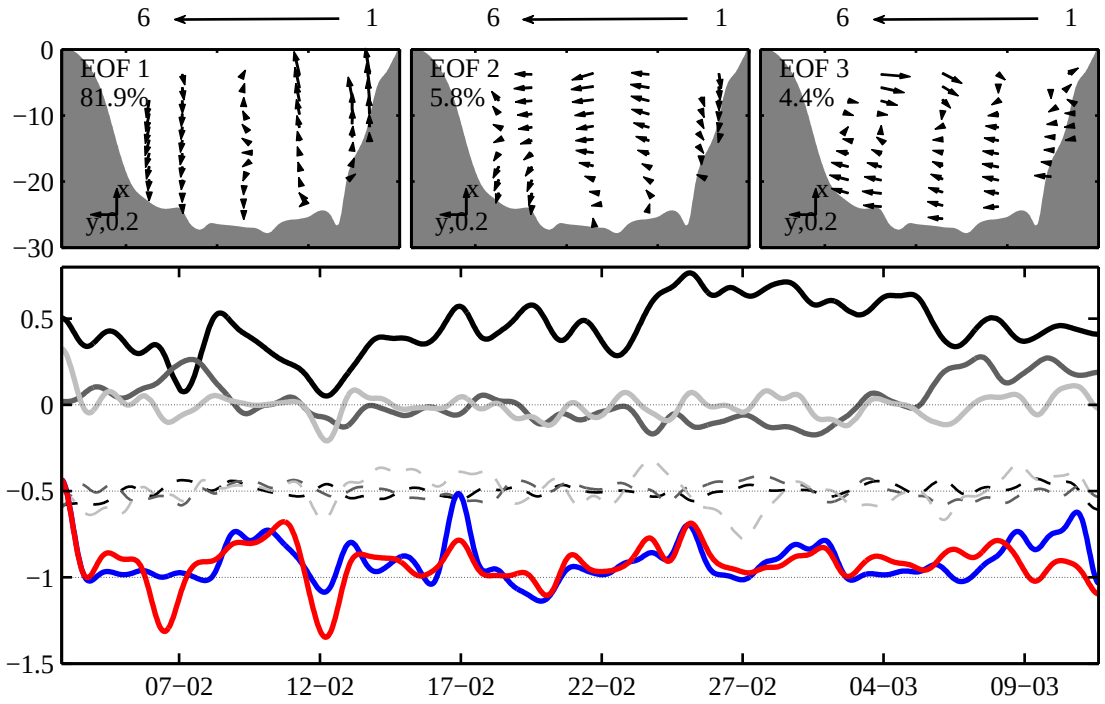

Figure 3.6: Top figures show the spatial structure of the first three EOFs of the low-passed current. The reader is looking toward the closed end of BC. Note that upward arrows are in the x direction, positive toward the closed end of BC. The bottom axes show the associated time series: black is EOF1, dark gray EOF2, and light gray EOF3. The full thick line is the real part, dashed lines the imaginary part centered around -0.5. Centered around -1 is the low passed along-bay wind stress (times 10) at the north (red) and south (blue) meteorological stations.

regression coefficient and summed. The result is multiplied by wind stress value of 0.1 Pa and shown in Figure 3.8. This is compared with the wind driven current from the theoretical model of chapter 2 for an turbulent eddy viscosity $K_2 = 4.10^{-3}$ and $K_3 = 2.10^{-3}$ m^2/s, lower than those used for deployments 1.

In the across-bay direction, the theoretical lateral circulation is to the right of the wind at the surface and in the opposite direction at depth. It is remarkably well reproduced by the observations at ADCPs 3-6. The observed wind

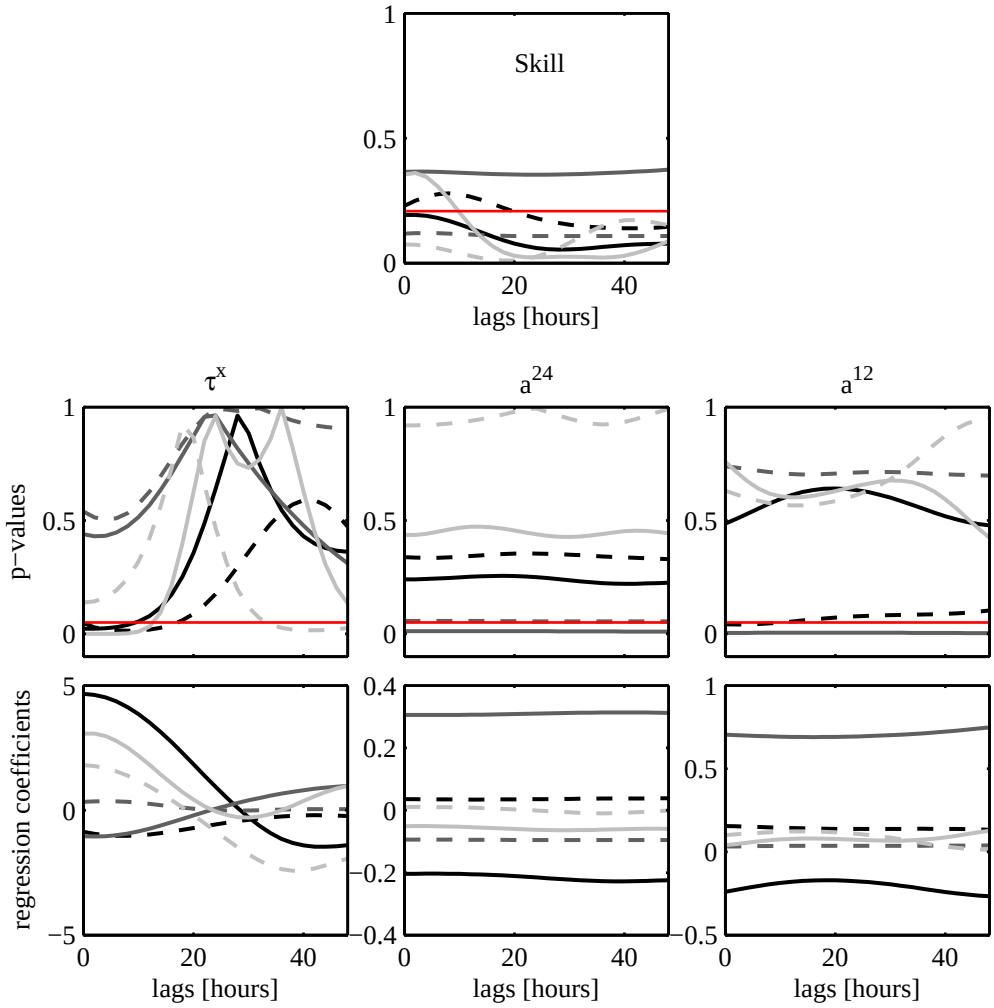

Figure 3.7: Significance of a linear regression between the wind stress (τ^x), the semi-diurnal (a^{12}) and diurnal (a^{24}) tidal envelopes and the first three EOFs (1 black, 2 dark gray, 3 light gray) real (full) and imaginary (dashed) time series. The skill of the regression is shown on the top figure. The red line shows the critical skill (95% level). The p-values of wind stress (left), diurnal tide envelope (center), and semi-diurnal tide envelope (right) are at the center. The red line is at the 5% level. The associated regression coefficients are on the bottom figures.

driven current is bounded by the theoretical predictions for both choices of eddy viscosity. At ADCP 1-2, the lateral circulation is overestimated by the theoretical model. Deployment 3 thus suggests lower values of the turbulent eddy viscosity with enhanced cross-wind circulation. One possible explanation for this decreased level of turbulence is a larger vertical stratification during deployment 3 compared to deployment 1. The water column is stratifying over the course of deployment 3 with buoyancy frequencies varying from 1 to 10 radian per seconds. In comparison, a series of CTD casts showed vertical stratifications below 1 rps during deployment 1. The wind events during deployment 1 are larger and associated with low air temperature, which would favor unstratified conditions and larger turbulence. There is unfortunately no continuous monitoring of the water column stratification during deployment 1 and no further comparisons can be made. Another possible explanation is that the turbulent eddy viscosity depends directly on the value of the wind stress. In a deep unstratified case, the eddy viscosity scales for example as $(u^*)^2/f$ ($u^* = \sqrt{\tau^x/\rho}$) and larger wind stress leads to larger eddy viscosities (Zikanov et al., 2003; Madsen, 1977). This dependence is however considered to be of lesser importance compared to that of stratification (Price and Sundermeyer, 1999).

The observed along-bay wind driven flow closely follows the structure of EOF 1 with a well-defined horizontal counter-clockwise circulation. It is downwind on the western side (ADCP 1 to 3),weak at the center (ADCP 4) and upwind at ADCP 5-6. The theoretical flow is as expected downwind on the shallow sides and upwind around the center of the section. Except for ADCP 1-2-5, the agreement between observations and theory is poor in the along-bay direction. Two possibilities arise from this analysis. The first possibility is that this well-defined horizontal counter-clockwise circulation is indeed related to the wind stress but that the theoretical model misses important dynamical ingredients. The build up of horizontal gradients of density would be a good candidate (see section 3.4 and 3.5). The effect of advection of momentum is another and could be investigated

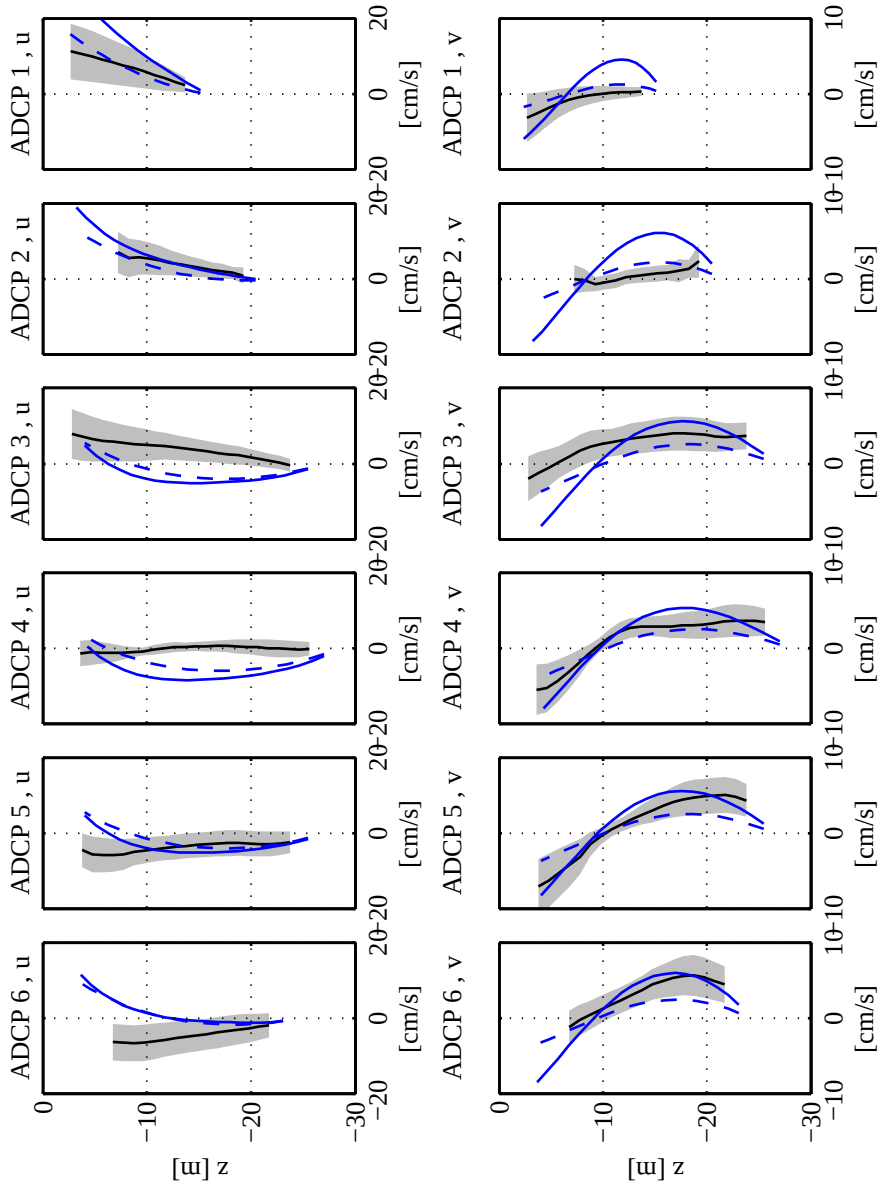

Figure 3.8: Observed wind driven current ($\tau^x = 0.1$ Pa) for 0 h lag (black, gray shading). The shading indicates bootstrap 10% confidence intervals. The blue curves are the theoretical currents with turbulent eddy viscosity $K_2 = 4.10^{-3}$ m^2/s (dashed) and $K_3 = 2.10^{-3}$ m^2/s (full).

with a numerical model such as ROMS. Other type of assumptions made by the model such as that of wind stress spatial uniformity may also not be valid. The survey on the Sproul R.V in March indicates indeed an intensification of the wind stress along the western shore of BC during Nortes events. The second possibility is that the low frequency wind stress is not related to the counter-clockwise horizontal circulations and that the correlation between wind stress and the real part of EOF 1's time series is spurious. A better understanding of this horizontal circulation would beneficial in both cases: it could explain how the low frequency wind drives the horizontal circulation in the first one, or it could permit its elimination early in the present analysis and improve the picture of currents driven by low frequency wind.

3.4 Depth-averaged momentum balances

The depth-averaged momentum equations assuming hydrostatic flow and small sea level variations compared with the water depth, are (Lentz et al., 1999):

$$\partial_t[u] + \frac{1}{h}\partial_x(h[u^2]) + \frac{1}{h}\partial_x(h[uv]) - f[v] = -\frac{1}{\rho_0}\partial_x P + \frac{\tau_s^x}{\rho_0 h} - \frac{\tau_b^x}{\rho_0 h}, \tag{3.2}$$

$$\partial_t[v] + \frac{1}{h}\partial_x(h[uv]) + \frac{1}{h}\partial_y(h[v^2]) + f[u] = -\frac{1}{\rho_0}\partial_y P + \frac{\tau_s^y}{\rho_0 h} - \frac{\tau_b^y}{\rho_0 h}, \tag{3.3}$$

where $[\cdot] = 1/h \times \int_{-h}^{0} \cdot\, dz$ is the depth averaging operator, $\tau_b^{x/y}$ and $\tau_s^{x/y}$ the bottom and surface stress, and h the local depth.

The depth-averaged pressure gradient is made of barotropic (P^s) and baroclinic contributions

$$\partial_{x/y} P = \partial_{x/y} P^s + \int_{-h}^{0} g\partial_{x/y}\rho\big(1 + z/h\big)dz; \tag{3.4}$$

P^s includes the effect of sea level slope and atmospheric pressure. The south and north pressure sensor were located in roughly 5 m water depth, 40 km apart. and winter hydrographic surveys have reported maximum density differences of 0.3 kg/m^3. This is equivalent to a baroclinic acceleration of 7.5 10^{-6} m/s^2 which we neglect. The difference of pressure between the two instruments is thus a good estimate of the basin-wide along-bay barotropic pressure difference. This difference is, however, only a proxy for the value of the pressure gradient at the center of the bay. At low frequencies, the difference of bottom pressure is well correlated with the along-bay wind stress. Based on theoretical considerations, this difference of pressure is thus scaled so as to balance the wind stress at the deepest location, (ADCP C for deployment 1 and ADCP 4 for deployment 3). This scaling ignores the importance of bottom stress which is shown to be a minor contribution in the depth-averaged momentum equations of an elongated wind driven bay (Winant 2004 and chapter 2).

The experimental design does not allow computation of the along-bay baroclinic pressure gradient. For deployment 3, the Tloggers chain provide an

estimate for the baroclinic pressure gradient in the cross-basin direction. The density is inferred assuming a constant salinity of 35.65 psu, leading to a -0.26 kg/m^3 change of density per degC. These estimates of density from temperature are 15% accurate for the hydrographic data collected during the CTD surveys of November 2004, February and March 2005.

Even though the ADCPs have a pressure sensors and could a priori be used in order to estimate pressure gradients, a 0.5 mm equivalent accuracy would be required in order to resolve cross-bay pressure gradients equivalent to acceleration of 10^{-5} m/s^2. This is much less than the expected accuracy of the sensor and prevents estimation of any pressure gradients based on the ADCP pressure sensors.

Nonlinear terms involving gradients in the cross-basin direction are computed with second order finite differences. The deployment strategy does not allow the estimation of the nonlinear terms, which involves along-bay gradients of the flow. The elongated shape of BC suggests that these terms are weak. The low pass filtering is computed after the nonlinear products of velocity, so that contributions from other frequency bands are also included.

The vertical integration of the flow is achieved by first interpolating from the flow on a 1 m spaced grid extending from the bottom to the surface, vertically averaging and multiplying by the local depth. The shear is assumed to be zero at the surface and the velocity zero at the bottom for the interpolation. This choice of bottom extrapolation leads to smaller values of the nonlinear terms. The bottom stress is assumed to follow a quadratic law formula:

$$(\tau_b^x, \tau_b^y) = -\rho_0 C_d \sqrt{u_b^2 + v_b^2}(u_b, v_b), \tag{3.5}$$

where $C_d = 2 \times 10^{-3}$, and (u_b, v_b) is the current at each ADCP bottom-most bin.

Table 3.2: Deployment 1. Depth averaged momentum balance in the x direction (10^{-5}cm/s^2)

ADCP location	$-\partial_t[u]$	$f[v]$	$-\partial_x P^s/\rho_0$	τ_s^x/h	$-\tau_b^x/h$	$-\frac{1}{h}\partial_y(h[vu])$	residual
			Mean				
C	0.0	−6.6	–	12.8	2.1	−1.0	7.3
E	−0.4	2.1	–	22.9	−0.7	−1.0	22.9
			Low frequency standard deviation				
C	2.7	10.4	16.4	18.6	1.8	2.6	12.3
E	6.4	2.7	16.4	33.2	6.3	2.6	16.2

Table 3.3: Deployment 1. Depth averaged momentum balance in the y direction (10^{-5}cm/s^2)

ADCP location	$-\partial_t[v]$	$-f[u]$	$\tau_s^y/\rho_0 h$	$-\tau_b^y/\rho_0 h$	$-\frac{1}{h}\partial_y(h[v^2])$	residual
			Mean			
C	−0.0	7.5	1.4	−0.1	4.1	12.8
E	0.0	−9.1	2.5	−0.0	4.1	−2.6
			Low frequency standard deviation			
C	2.2	10.0	2.9	1.1	4.1	9.4
E	1.1	28.9	5.3	0.6	4.1	29.5

3.4.1 Deployment 1

Along-bay direction

During deployment 1, the mean along-bay momentum balance is dominated by the wind stress, which predominantly blows toward the closed end of BC at this time of the year (Table 3.2). In light of the good correlation between sub-inertial along-bay wind stress and pressure gradient and the similar standard deviation of both terms, the mean along-bay pressure gradient is expected to be in balance with the mean wind stress.

The wind stress has the largest standard deviation. At location C, the axial pressure gradient standard deviation is by choice of similar amplitude than the wind stress. The good correlation between wind stress and pressure gradient leads to a residual of reduced amplitude, about 2/3 of both terms' standard deviations. The Coriolis acceleration due to a depth-averaged cross-bay flow is smaller. At

location E, the wind stress term has a larger standard deviation because of the shallower depth. An increase of the bottom stress term partly counterbalances the wind stress. The acceleration has similar amplitude to the bottom stress.

Cross-bay direction

In the cross-bay direction, the mean momentum balance involves terms of similar amplitude compared to the along-bay direction (Table 3.3). The Coriolis acceleration dominates at location E. The contribution of the lateral advection of momentum is significant at location C.

The Coriolis acceleration associated with the along-bay depth-averaged flow has its largest standard deviation at location E and C. This term is probably balanced by a barotropic or baroclinic pressure gradient, which we have no way of estimating here.

3.4.2 Deployment 3

Along-bay direction

The mean along-bay momentum balance is dominated by a mean wind stress toward the closed end of the bay (Table 3.4). The mean bottom stress opposes the mean horizontal counter-clockwise circulation and the nonlinear term is negative on the eastern side of BC, positive on the western one. The Coriolis acceleration is significant and positive along the section, corresponding to a flow to the left of the ADCP base orientation.

The momentum balance fluctuations are dominated by nonlinear terms on the western side of the bay. A decomposition of these terms into contributions from the low- and high- frequency flow shows that the low-frequency flow is the dominant contribution. The wind stress, barotropic pressure gradients, acceleration and Coriolis acceleration have similar standard deviations. The acceleration standard deviations decreases toward the eastern side of the bay. The bottom stress is

smaller, largest on the shallow sides, with a minimum at the center.

Correlations between pair terms have been systematically investigated. The significant degree of correlation is 0.4 for the 22 degrees of freedom of the time series. The wind stress and the barotropic pressure gradient are, as expected from section 3.2, significantly correlated ($r = 0.92$). The slope of the correlation ranges from 1 to 1.79 at the shallowest locations. There is some correlation between the Coriolis acceleration and the nonlinear term at the following ADCP locations: 2 ($r = 0.57$, slope of 1.6) ; 4 ($r = 0.42$, slope of -0.32) ; 6 ($r = 0.58$, slope of 0.44). At ADCP 6, the bottom stress and the axial pressure gradient are correlated with $r = 0.57$ and a slope of 2.4.

Cross-bay direction

The mean momentum balance in the cross-bay directions is poorly closed and dominated by the Coriolis accelerations associated with the mean horizontal counter-clockwise circulation (Table 3.5). The lateral baroclinic pressure gradient has a similar amplitude on the western side but with the same sign, such that the mean momentum balance is largely unbalanced there. Other terms are of smaller importance.

In the cross-bay direction, the baroclinic pressure gradient has the largest overall standard deviation. The Coriolis acceleration is next. The large residual standard deviation indicates that the momentum balance is poorly closed. Term by term correlation computations are, for the most part, not significant or if so, the sign of the regression slope is inconsistent with the momentum balance.

The most likely explanation for the poor closure of the cross-bay momentum balance is the lack of knowledge of the lateral barotropic pressure gradient. In some situations, as for a buoyant river plume propagating along the coast or for strait flows, the situation is in fact similar to what is observed here (Fong and Geyer, 2002; Munchow and Garvine, 1993; Garrett and Petrie, 1981). A cross-plume depth-averaged momentum balance involves a Coriolis acceleration due to

the along-plume velocity and a cross-plume baroclinic pressure gradient of the same sign. The sum of both is balanced by an increase of sea level toward the coast. In order to test this, the momentum balance can be differentiated vertically in order to get rid of the barotropic pressure gradient. This is the thermal balance described in the next section.

Table 3.4: Deployment 3. Depth averaged momentum balance in the x direction (10^{-5}cm/s^2)

ADCP location	$-\partial_t[u]$	$f[v]$	$-\partial_x P^s/\rho_0$	τ_s^x/h	$-\tau_b^x/h$	$-\frac{1}{h}\partial_y(h[vu])$	residual
				Mean			
1	−0.0	4.6	–	4.3	−2.3	0.8	4.7
2	−0.2	2.0	–	3.2	−0.7	−0.8	0.8
3	0.0	7.0	–	2.6	−0.1	0.8	7.7
4	−0.1	1.6	–	2.4	0.0	3.2	4.5
5	0.0	0.9	–	2.6	1.1	4.5	6.5
6	−0.1	6.0	–	2.9	1.4	−1.0	6.5
				Low frequency standard deviation			
1	4.9	2.9	4.9	7.6	1.5	13.5	15.9
2	3.8	2.6	4.9	5.7	1.0	7.2	7.9
3	2.5	7.9	4.9	4.6	0.8	2.1	7.4
4	2.3	8.1	4.9	4.3	0.6	3.6	11.4
5	1.9	7.0	4.9	4.6	0.9	3.8	7.3
6	2.4	4.8	4.9	5.1	1.0	3.6	5.3

Table 3.5: Deployment 3. Depth averaged momentum balance in the y direction (10^{-5}cm/s^2)

ADCP position	$-\partial_t[v]$	$-f[u]$	$\tau_s^y/\rho_0 h$	$-\tau_b^y/\rho_0 h$	$-\int_{-h}^{0} g\partial_y\rho/\rho_0(1+z/h)dz$	$-\frac{1}{h}\partial_y(h[v^2])$	residual
				Mean			
1	0.0	−38.9	−2.3	−0.0	−44.1	−0.1	−85.4
2	−0.0	−29.8	−1.7	0.9	−62.4	−1.9	−94.9
3	0.1	−25.1	−1.4	−0.1	−4.1	−2.6	−33.2
4	−0.0	−1.7	−1.3	−0.0	−1.0	0.8	−3.2
5	−0.1	23.0	−1.4	0.2	−4.8	1.9	18.9
6	−0.0	30.8	−1.5	0.0	−1.1	4.9	33.1
				Low frequency standard deviation			
1	0.9	18.0	3.1	0.4	66.7	6.4	71.4
2	0.6	12.3	2.3	2.5	90.8	3.5	93.9
3	2.1	8.8	1.9	0.4	6.5	2.4	11.9
4	1.6	6.8	1.7	0.4	12.7	2.2	16.5
5	1.6	9.8	1.9	0.5	5.8	2.6	9.5
6	1.5	12.2	2.1	0.7	11.0	3.1	15.9

3.5 Thermal wind balance

Thermal wind balance is obtained by differentiating vertically the cross-bay momentum balance, while ignoring nonlinear, viscous and acceleration terms (Gill, 1982):

$$f\partial_z u = g\partial_y \rho/\rho_0. \tag{3.6}$$

Thermal balances have been shown to hold down to depths as shallow as 10 m (Yankovsky, 2006; Lentz et al., 1999). In this section terms we compare on each sides of Equation 3.6 with a least squares fit of the vertical shear by the horizontal density gradient. The vertical shear is computed with a centered second order scheme and the horizontal density gradient is computed at the temperature logger depths first and then interpolated onto ADCP bin levels. This is done for ADCP deployment 3, which is the only winter time deployment when ADCP and density information are present simultaneously. The correlation coefficient, slope and intercept of the fit are shown on Figure 3.9 as function of depth and ADCP location.

The thermal wind balance holds most successfully at ADCP 6 over nearly all available depths (-20 m $< z <$ −7 m). The corresponding regression coefficients are close to unity, larger than 0.5 and smaller than 2. At ADCP 3 to 5, the correlation is significant at depths greater than 10 m, with regression coefficients between 0.25 and 1.5. Closer to the surface, the correlation and regression coefficient are overall weaker, which we explain by the presence of larger vertical gradients of temperature. The positions of these large gradients are difficult to track with fixed depth temperature loggers and degrades the quality of the horizontal density gradients estimates. Turbulent stresses related to the wind are a second explanation as they can also create departures from the thermal balance.

At ADCP 1 and 2, the correlation is not significant at all vertical levels. This is despite the large horizontal gradient of density observed through the depth-averaged momentum balances. The standard deviation of the vertical shear is in

fact five time less that of the density gradient scaled according to Equation 3.6. One explanation for this apparent failure of the thermal wind balance is that our estimate of the horizontal density gradient at ADCP locations 1 and 2 is poor. It is, for example, possible that the horizontal structure of the density field is finer that the separation between temperature logger chains. The low-frequency flow driven at ADCP location 1 and 2 could be then driven solely by the cross-bay sea level slope through geostrophy. This is a situation typical of bottom-advected buoyant plumes (Yankovsky and Chapman, 1997). The dynamical balance would then be that of a geostrophic flow, possibly modified by turbulent stresses due to the proximity of the bottom. It is also possible that other dynamical terms (e.g. advection of momentum and turbulent stresses) are important. Adding the across-bay acceleration term $\partial_{zt}v$ on the left hand side of Equation 3.6 does not however improve these results.

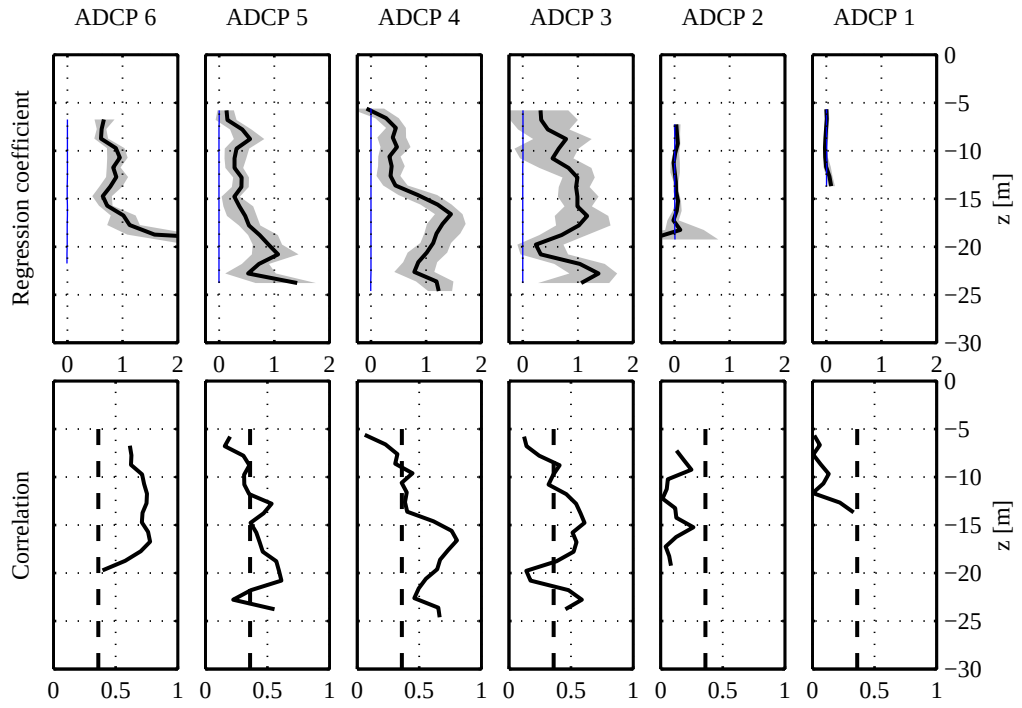

Figure 3.9: Thermal wind balance, deployment 3. In the top figures, the slope (thick black, 95% bootstrap confidence interval is the gray shading) and intercept (thin blue) of a least squares regression of the vertical along-bay shear $\partial_z u$ on the scaled cross-bay density gradient ($g\partial_y \rho/\rho_0 f$). In the bottom figures, the corresponding correlation (black full line) is shown as well as the critical correlation at a 95% levels (dashed line).

3.6 Evolution of the density field

In the past section, it was shown that part of the low frequency along-bay circulation is in thermal wind balance. This section describes the spatial structure and evolution of the density field along the ADCP cross section. The method employed here is to compute an EOF decomposition of the density field. Prior to the EOF decomposition, the horizontally averaged density anomaly is subtracted at any given instant in time from the density anomaly at each thermistor chain location. This removes the overall warming and increase of stratification which does not affect the computation of the horizontal density gradients but would otherwise be the dominant modes of variability. This warming and increase of stratification is illustrated by the evolution of the horizontally averaged density anomaly shown on the top left plot of Figure 3.10. Differences of density range from 10^{-2} to 0.3 kg/m^3 over 20 m depth. Assuming a linear profile of density, this corresponds to mode 1 phase speeds of 2 and 11 cm/s and baroclinic Rossby radii of deformation of 0.3 km and 1.8 km, respectively.

The first EOF of the density anomaly represents 59% of the total variance and represents a decrease of density on the western side of the bay (ADCP location 1 to 3) and a increase of density on the eastern side (ADCP location 5 to 7). The amplitude of these variations decreases toward the deeper central ADCP locations. The time series associated with this first EOF is weak and slowly increasing during the first half of deployment 1. As the vertical stratification increases, there are three large oscillations with typical periods of 2 days of the first EOF time series on top of positive trend. The time series is always positive, meaning that the density increases from west to east, consistent with depth-averaged momentum balances. This is consistent with the mean southward direction of the wind, which is downwelling favorable on the western shore and upwelling favorable on the eastern one. The period of the first EOF oscillations also happen to be consistent with the time it would take for a water parcel to be advected around the closed of BC

at a pace of 5 cm/s, which roughly scales as a typical value of the mean horizontal counter-clockwise circulation.

The second EOF accounts for 23.2% of the variance. Its spatial structure is similar to EOF 1 except for location 1, where it is of opposite sign. The time series of the second EOF is similar to the first one: weak during the first half of the deployment and larger with three oscillations with typical periods of 2 days during the second half. Each extremum precedes an extremum of the first EOF during the second half of the deployment. The combination of EOF 1 and 2 suggests that the fluctuations of temperature are propagating from the center of the cross-section to its western side.

During the second half of the deployment, differences of density are typically of the order of 0.2 kg/m^3 between the western and eastern side of BC. One possible explanation for this horizontal difference of density is that the cross-bay wind driven circulation advects relatively warmer water to the west at the surface and colder water to the east at the bottom of the water column. For a vertical density difference of 0.1 kg/m^3, a vertical difference of velocity of 3 cm/s per second is required to produce an horizontal change of density of 0.2 kg/m^3 in 2 days. The low frequency wind driven cross-bay circulation could therefore produce this horizontal density difference.

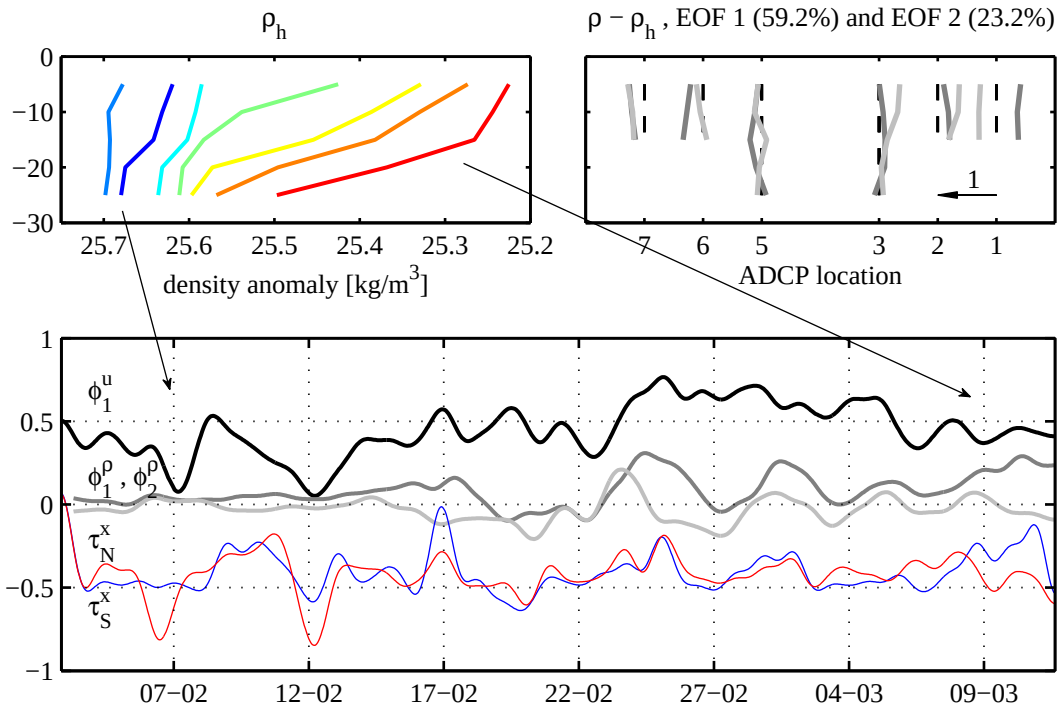

Figure 3.10: Deployment 1. Top left plot shows the horizontally averaged density anomaly ρ_h as a function of depth. Colors represent time, dark blue being the deployment start and red the deployment end. Each curve is separated by 5 days. Top right plot shows the first (heavy gray) and second (light gray) EOF spatial structure function of the density anomaly minus its horizontal average as a function of depth (vertical) and location (horizontal). The dashed lines represent 0, positive values are toward the left. Bottom plot shows the time series of the first current EOF (ϕ_1^u) in thick black, of the density EOF shown on top right axes in dark and light gray, and of the along-bay wind stress at the North (red) and South (blue) meteorological station times 10.

3.7 Summary and conclusions

In this chapter the low-frequency dynamics inside BC is described for fall and winter deployments and the response to low frequency winds is extracted. The sea level response to wind stress is, as expected, an increase of sea level in the downwind direction. In fall (deployment 1), the wind driven current is downwind on shallow sides. At depth, the cross-wind circulation predicted by theoretical models is not observed, which is attributed to elevated values of the turbulent stresses (K$\sim 10^{-2}$m^2/s) and dynamics similar to shallow embayments. In winter (deployment 3), the lateral circulation is well defined, with typical values of the order of 5 cm/s for a wind stress of 0.1 Pa. This is explained by the presence of a larger vertical stratification and a decreased level of turbulence (K$\sim 3\times 10^{-3}$m^2/s). The wind driven along-bay flow differs however from theoretical predictions, with a large counter-clockwise circulation in the horizontal plane. The origin of this horizontal circulation and its potential relationship to wind forcing are as yet undetermined. Inspection of the momentum balance indicates that lateral pressure gradients are large and in thermal balance with part of the along-bay flow. One possible explanation is that density driven features are propagating in the along-bay direction and driving currents as buoyant plumes would. The combination of the observed wind driven lateral circulation and the vertical stratification is sufficient to create a lateral baroclinic pressure gradient.

Other explanations for the presence of the horizontal circulation are related to the large values of the Rossby number ($u/fW > 0.15$, where $u \sim 5$ cm/s, f is the Coriolis acceleration and $W \sim 5$ km is the width of the bay). Nonlinearities are not included in the theoretical model used here. As shown by independent numerical simulations, including nonlinearities breaks the symmetry of the along-bay circulation and increases the downwind flow along the shore to the right of the wind, in the same sense as the observations. Further quantification of this would be required in order to have more conclusive results. As shown in chapter 4, the

diurnal wind component drives a response as large as the low frequency response and rectification of this response, i.e. generation of low frequency currents by high frequency ones via nonlinearities, is possible as confirmed by preliminary numerical work. Overall it seems that great insight could be gained from a set of numerical simulations with configurations similar to the present one.

3.8 Appendix

This appendix describes the method employed in order to extract wind driven currents. First a complex EOF decomposition is computed (Emery and Thomson, 2001). The current at bin i, called u_i, is represented by

$$u_i(t) = \sum_j \phi_j(t) u_i^j, \tag{3.7}$$

where u_i^j is the spatial structure of EOF j at bin i and $\phi_j(t)$ is the time series associated with EOF j. $\phi_j(t)$ is a complex time series, whose amplitude scales the magnitude of EOF j and whose phase represent the angle by which EOF j is rotated at one given instant in time.

A least squares regression is then computed between the real or imaginary part $\phi(t)$ of $\phi_j(t)$ and the lagged along-bay wind stress $\tau^x(t-t_0)$ (lag t_0), the tidal envelope of the semi-diurnal a^{12} and diurnal tide a^{24}:

$$\hat{\phi}(t) = b_0 + b_1\tau^x(t-t_0) + b_2 a^{12}(t) + b_3 a^{24}(t). \tag{3.8}$$

The skill S of the linear regression is given by:

$$S = 1 - < e^2 > / < \phi^2 >, \tag{3.9}$$

where $< \cdot >$ is a time average and $e = \phi - \hat{\phi}$ is the prediction error.

The significance of one of the explanatory variable ($\tau^x(t-t_0)$,a^{12},a^{24}) is estimated by comparing the sum of squared error with ($< e^2 >$) or without the

explanatory variable of interest (e_r^2):

$$f = \frac{(< e^2 > - < e_r^2 >)/M}{< e^2 > /(N_{dof} - N_v)}, \tag{3.10}$$

where N_v is the total number of explanatory variables (4 with the constant term), N_{dof} is the number of degrees of freedom, M is the number of variable tested (1 if only the wind is tested, for example, see von Storch and Zwiers (1999); Emery and Thomson (2001)). Under classical assumptions of independence, normality, no mean and constant variance for the prediction error, f follows an F distribution with $(M, N_{dof} - N_v)$ degrees of freedom.

The p value of the explanatory variable estimates whether a significant amount of variance is explained by the use of the tested predictor variable:

$$p = 1 - \int_0^f F_{M,N_{dof}-N_v}(x)dx \tag{3.11}$$

where F is the probability density function of the F distribution with $(M, N_{dof} - N_v)$ degrees of freedom.

4

Observed response to diurnal winds

4.1 Introduction

BC is located around 26.7°N where the inertial period of 26.7 h is close to the diurnal period. The winds inside BC are modulated at the diurnal frequency (chapter 1) and can possibly drive a resonant response as shown in chapter 2. This chapter described the wind driven inertial response observed inside BC.

Wind driven near-inertial oscillations (NIOs) are ubiquitous features of the upper ocean. They have been observed and modeled for a long time (Webster, 1968; Pollard and Millard, 1970; Kundu, 1976). NIOs are excited by rapid changes in wind stress intensity or direction, by storms for example, and are only one component of the ocean response to wind stress, the low frequency Ekman response being another (Ekman, 1905). These NIOs are free once the storm has passed. They are energetic ($u_i \sim \tau/\rho f h_m$, u_i being the typical inertial current amplitude, τ the wind stress, f the Coriolis frequency, h_m the mixed layer depth), nearly uniform over the mixed layer depth and thus well-modeled by slab-layer models (Pollard, 1970; D'Asaro et al., 1995). NIOs decay over time scales ranging from

4 to 20 days by dissipating energy via shear-driven turbulence at the base of the mixed layer and radiation to the ocean interior. In theory, their spatial coherence is large according to the large spatial scales of storms and the near-inertial dispersion relation, but limited in practice by the existence of a background vorticity field (e.g. mesoscale eddies). This background vorticity field is recognized to shift the inertial frequency and enhance the radiation to the ocean interior (Kunze, 1985; Young and Ben Jelloul, 1997).

Over the continental shelf, wind driven NIOs have also been frequently reported(MacKinnon and Gregg, 2005; Shearman, 2005; Simpson, 2002; Rippeth et al., 2002; Chant, 2001; Lerczak et al., 2001). The presence of a physical boundary is a direct source of divergence of flow in the upper layer, which quickly generates NIOs at depth. NIOs usually have thus a low modal structure close to coasts (MacKinnon and Gregg, 2005; Shearman, 2005; Jacobs et al., 2001; Millot and Crepon, 1981; Kundu et al., 1983). NIOs typical of the open ocean (surface intensified with downward propagation of energy) have also been observed however(Kundu, 1976; Lerczak et al., 2001). MacKinnon and Gregg (2005) decomposed the ocean response from observations in 70 m depth into vertical modes and showed transfer between modes due to the nonlinearities introduced by the bottom stress and the evolution of stratification. Shearman (2005) observed in the same area shelf-wide (100 km scales) coherent NIOs, which decreased in magnitude onshore and were stronger in stratified summer conditions. The occurrence of NIOs under stratified conditions is also noted by Jacobs et al. (2001).

In an enclosed or semi-enclosed basin, most studies focus on the wind driven internal wave activity (Antenucci et al., 2000; Stevens and Lawrence, 1997; Orlic, 1987). In lakes, the vertical thermal stratification is large, e.g. because of the lack of tidal mixing. Baroclinic wave phase speeds are fast (Antenucci et al. (2000) report up to 35 cm/s for a mode 1), and the baroclinic Rossby radius of deformation is large. Lakes can be sites of significant diurnal sea breezes. This continuous forcing is a departure from the ideal case of an ocean ringing after the

passage of a storm. Antenucci et al. (2000) reports on the difficulty of using a "free wave" formalism in such a case even when well defined spatial modes of oscillations can be identified.

This chapter starts by investigating the sea level response inferred from observations of bottom pressure to wind as a function of frequency. This is compared with the theoretical predictions of chapter 2. The wind driven current response is then extracted after band pass filtering and with a least squares fit. It is also compared with results from chapter 2. The dynamics in the diurnal band are finally investigated.

4.2 Sea level response to wind

This chapter investigates the relationship between the along-bay difference of sea level and the wind stress in the frequency domain. A similar study is done in the time domain at sub-inertial frequencies in chapter 2 (Figure 3.2). BC is open to the ocean and wind driven fluctuations of sea level can be produced in two ways. First the wind can drive a local response, which is similar to the response of a basin where sea level is clamped at its mouth. Second, the wind can produce a response inside the Gulf of California (GC). The associated sea level oscillations at the mouth of BC can then propagate through BC. This would be similar to the response to sea level fluctuations described in the chapter 5. The response at the mouth and closed end of BC is at a given frequency:

$$N_n = H_{\eta_n,\tau} \times \tau \tag{4.1}$$

$$N_s = H_{BC,\tau} \times \tau + H_\eta \times H_{\eta_n,\tau} \times \tau \tag{4.2}$$

The Fourier transforms of the wind stress, sea level at the north and south are given by τ, N_n and N_s respectively. $H_{\eta_n,\tau}$ is the transfer function between the wind stress and sea level at the mouth of BC. This is the response that would be created inside the GC if the mouth of BC were closed. I assume that the wind

stress is the same inside the GC and BC, and that the sea level at the mouth of BC is imposed by the response inside the GC, which is reasonable as the GC is much deeper than BC (Garrett, 1975). The difference of sea level complex amplitude between the closed end and mouth is then

$$N_s - N_n = \left(H_{BC,\tau} + (H_\eta - 1) \times H_{\eta_n,\tau}\right) \times \tau \tag{4.3}$$

$$= H_{\eta_s - \eta_n,\tau} \times \tau. \tag{4.4}$$

In the following analysis, the sea level is detided and compared with the wind stress at the mouth with a cross-spectral analysis. This provides estimates for $H_{\eta_s-\eta_n,\tau}$ and H_{τ,η_n}. The GC sea level response to wind is for example given by H_{τ,η_n}:

$$H_{\eta_n,\tau}(f) = \frac{< \tau^\dagger N_n >}{< \tau^\dagger \tau >}, \tag{4.5}$$

$$C^2_{\eta_n,\tau}(f) = \frac{| < \tau^\dagger N_n > |^2}{< \tau^\dagger \tau >< N_n^\dagger N_n >} \tag{4.6}$$

where $< \cdot >$ is an average over fft blocks, † the complex conjugate operator, f the frequency, N_n the Fourier transform of the sea level at the mouth, and $C^2_{\eta_n,\tau}(f)$ the square coherence. The gain $|H_{\eta_n,\tau}|$ of the transfer function is its absolute value and quantifies the amplitude of the sea level response at the mouth compared to the wind stress magnitude at a given frequency.

The along-bay difference of sea level and the wind stress are significantly coherent up to 4-5 cpd frequencies (Figure 4.1, upper panel). The coherence square maximum forms a broad peak between 0.1 and 0.5 cpd. The decrease of coherence between sea level difference and wind follows the decrease of coherence between wind stress at each end of the bay (blue on the same axis). The coherence between the sea level at the mouth and the wind stress is below the significance level at most frequencies, favoring the idea that the wind explains little of the sea level fluctuations inside of the GC, see section 3.2 andMerrifield and Winant (1989).

The amplitude of $H_{\eta_s-\eta_n,\tau}$ is nearly constant up to 3 cpd with values between 1 and 2 cm/0.1 Pa. At peak coherence (0.1-0.5 cpd), it has a value of 2 cm/0.1 Pa. The corresponding phase is weak between -15 and 15°. Between

3 and 6 cpd, there is an increase of amplitude (3 to 10 cm/0.1 Pa) along with a 180° phase jump. This occurs with low values of coherence and larger confidence intervals.

The GC contribution to along BC sea level difference ($(H_\eta - 1) \times H_{\eta_n,\tau}$, dashed red on Figure 4.1) is computed with the observed $H_{\eta_n,\tau}$, and with a theoretical estimate of sea level transfer function H_η presented in Appendix 5.5. This sea level transfer function is shown to correctly reproduce the observations in section 5.2.1. The same theoretical model forced with wind stress and with a mouth sea level clamped to 0 provides an estimate for $H_{\tau,BC}$, the local response to wind stress. The sum of both contributions is a semi-theoretical prediction of the wind-sea level transfer function labelled $H^{sth}_{\eta_s-\eta_n,\tau}$ (full red curve on Figure 4.1). An eddy viscosity of 2×10^{-2} m^2/s has been chosen in order to match the peak near 5 cpd approximately. The choice of eddy viscosity doesn't modify the low frequency response.

At low frequencies ($<$ 8 cpd), there is a good agreement in phase and amplitude between the semi-theoretical estimate and the observed $H_{\eta_s-\eta_n,\tau}$. Close to the diurnal frequency, the amplitude of the transfer function decreases and becomes significantly different from the semi-theoretical estimate. This feature is unexplained, especially given the observed increase of diurnal wind stress amplitude toward the closed end of BC (section 1.2.3). For frequencies lower than 3 cpd, the contribution of the GC to the along-bay sea level is negligible. This is because a sea level fluctuation at the mouth instantly propagates to the closed end at these low frequencies and the associated sea level difference $(H_\eta - 1)$ is small. Around 5 cpd, the semi-theoretical and observed $H_{\eta_s-\eta_n,\tau}$ both exhibit a maximum with a 180° phase shift. The contribution of GC response to the semi-theoretical estimate is more significant then and contributes to the along-sea level difference as much as the local response does. This contribution is noisy, however, owing to the low coherence between the sea level at the mouth and the wind stress and these results have to be taken with care.

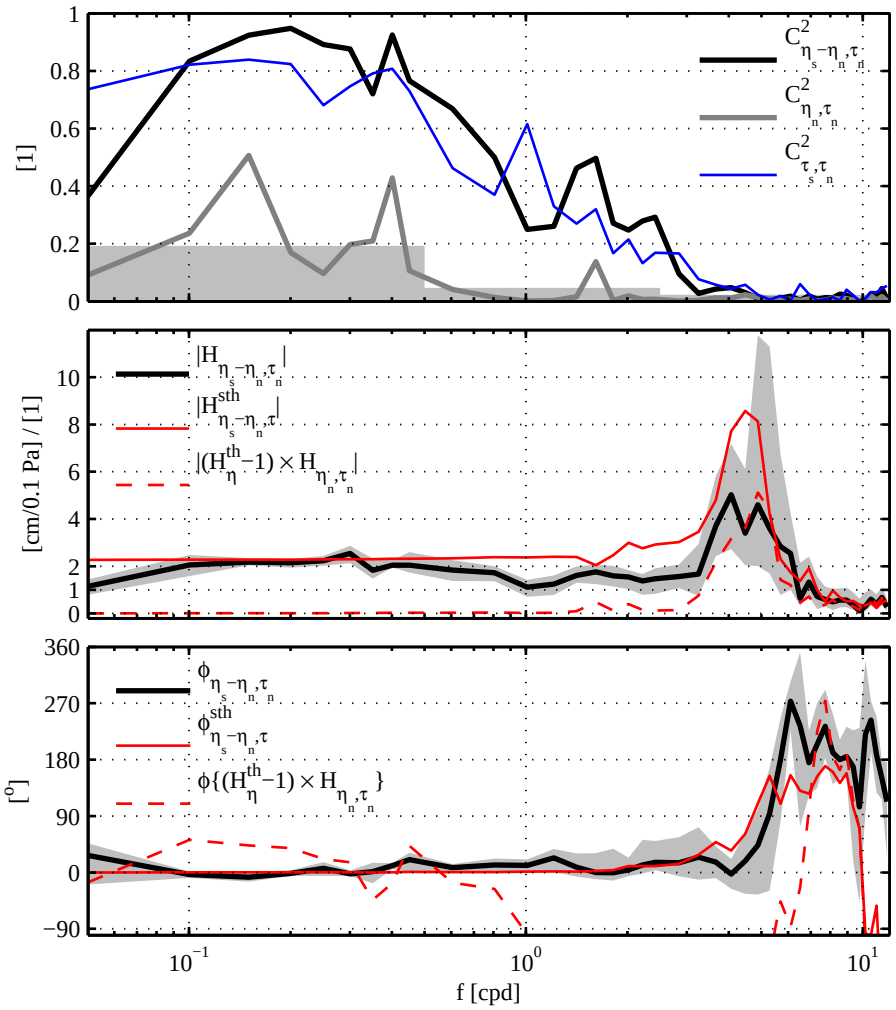

Figure 4.1: Top panel is the coherence squared between the along-bay sea level difference (black)/ mouth sea level (gray) and the wind stress at the north station, the wind stress at the north and south stations (blue). The central panel shows the transfer function amplitude between the along-bay sea level difference and the wind stress (black). Full red is the semi-theoretical estimate of the same transfer function and dashed the GC contribution to the semi-theoretical estimate. The phase of the same variables is shown on the bottom panel. Gray shading represents 95% confidence interval or significance levels.

4.3 Current response to diurnal winds

4.3.1 Overview

The nature of current fluctutations near the diurnal-inertial frequency is partly revealed by the spectra of the barotropic and baroclinic contributions to the flow at the center of BC (Figure 4.2). The barotropic contribution has well-defined peaks at tidal frequencies during deployment 1 and 3. There is a 2.5 times decrease of diurnal band barotropic energy from deployment 1 to 3 (Table 4.1). Because the tidal energy is similar between both deployments, processes other than tides must be present and drive diurnal barotropic currents. An alternative explanation for this decrease is an increase in the baroclinicity of tidally driven currents during deployment 3. The baroclinic currents are overall peaked around the diurnal frequency with a dominant clockwise (CW) contribution. During deployment 1, the CW peak is as narrow as the diurnal barotropic one. During deployment 3, it is broad and extends up to the semi-diurnal frequency and there is no significant counter-clockwise signal. Integrated over the 0.73 to 1.33 cpd frequency band, there is a 1.5 times increase of baroclinic CW kinetic energy between both deployments (Table 4.1). Comparatively, the diurnal band wind stress decreases by a factor of 2. We must conclude that the wind is either not driving baroclinic currents alone or that if it is, the wind is less effective at doing so during deployment 1. The remaining of this chapter thus focuses on deployment 3, when the strongest CW baroclinic response is observed.

4.3.2 Method

The strategy employed in order to extract diurnal wind driven currents during deployment 3 first consists in filtering currents, wind stress and tidal sea level in the diurnal band (0.73 to 1.33 cpd, filter shown on Figure 1.5). The wind stress at the south station along its major axis is used here. Using the wind

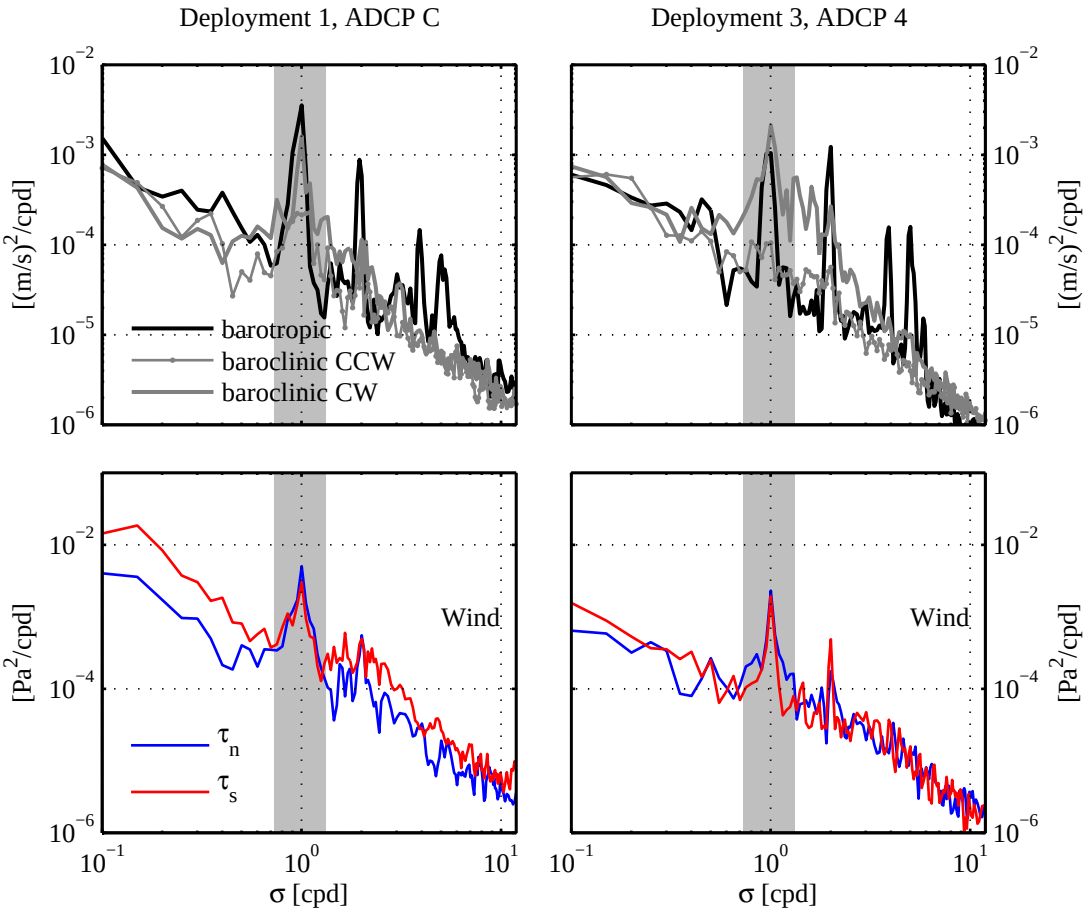

Figure 4.2: Top panels show the depth-averaged current and baroclinic current clockwise (CW) and counter-clockwise (CCW) spectral densities for deployment 1, ADCP C (left) and deployment 3 ADCP 4 (right). The wind stress spectra are shown below for the meteorological stations at the south (τ_s) and north (τ_n) of BC. The CW/CCW decomposition is not shown for the wind because the wind is nearly rectilinear and both CW and CCW contributions are equal. The gray shading indicates what is defined as the diurnal-inertial band.

stress at the north station instead gives similar results. The tidal sea level used is from a tidal analysis of the year long sea level bottom pressure measurements (section 1.2.3). A linear regression is then computed between the current and, as explanatory variables, the wind stress (τ) and sea level (ζ_{24}). 90° phase shifted

Table 4.1: Kinetic energy partition during deployment 1 and 3 at ADCP locations C and 4. The inertial contributions are expressed in percentages of the total inertial band kinetic energy.

	Kinetic energy	Subinertial	Inertial band			
	$[cm^2/s^2]$	$[cm^2/s^2]$	total $[cm^2/s^2]$	barotropic	baroclinic CW	baroclinic CCW
Deployment 1 ADCP C	29.0	23.5	7.1	55.4%	33.0%	11.6%
Deployment 3 ADCP 4	20.3	7.3	5.8	26.8%	66.2%	7.1%

wind stress (τ_{24}^{90}) and sea level (ζ_{24}^{90}) are also included as explanatory variables in order to allow phase differences between forcing and current response. These time series are computed with Hilbert transforms (Bendat and Piersol, 2000; Emery and Thomson, 2001). The regression is simultaneously done with the sea level in order to compare wind and tidal currents. A linear regression between the tide and the wind stress shows that there is a weak correlation (0.4) between both which does not affect the linear regression. Computing the linear regression of currents with tide and wind separately does not indeed modify the present results qualitatively. The significance of the regression is computed with standard methods (similar to appendix 3.8), assuming a number of degrees of freedom N_{dof} of 23, which is the number of points within the frequency diurnal band ($N_{dof} \sim T\Delta\sigma$, where T=36.8 days is the record length and $\Delta\sigma = 0.6$ cpd is the diurnal bandwidth). The linear regression on along- (u) and cross- (v) bay currents is finally expressed as:

$$u = u_1\zeta_{24} + u_2\zeta_{24}^{90} + u_3\tau_{24} + u_4\tau_{24}^{90} \tag{4.7}$$

$$v = v_1\zeta_{24} + v_2\zeta_{24}^{90} + v_3\tau_{24} + v_4\tau_{24}^{90} \tag{4.8}$$

The model is overall successful at capturing the diurnal variability of the currents (Figure 4.3). In the along-bay direction, both tides and winds explain between 30 and 90% of the diurnal band kinetic energy. The skill is lowest close to the surface at ADCP location 3 and 4. The tide significantly explains part of

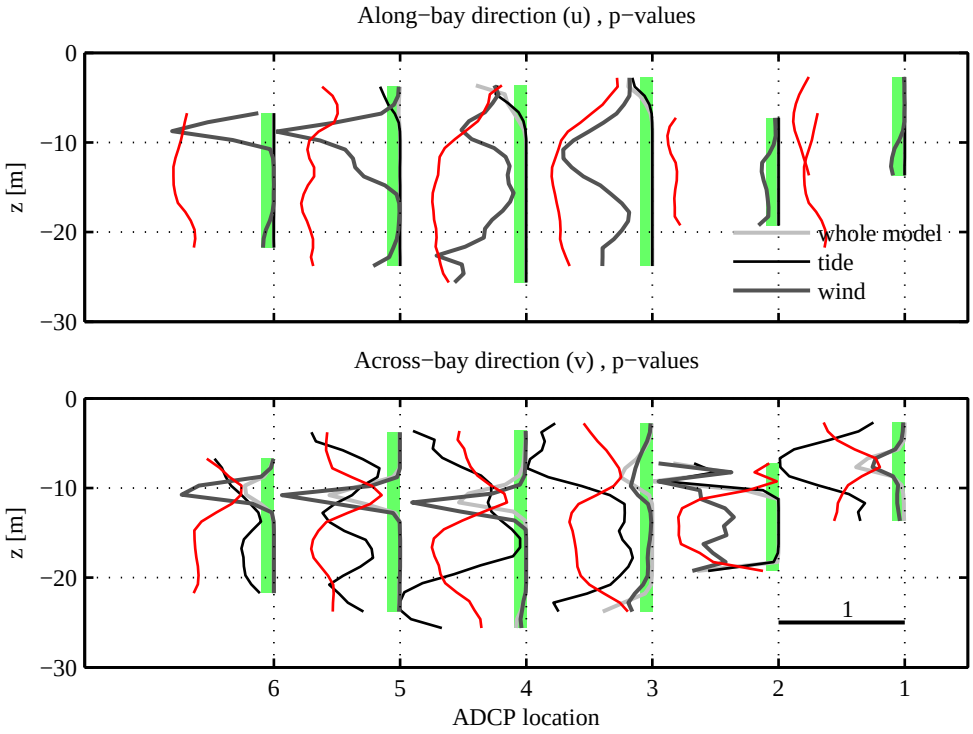

Figure 4.3: Significance levels of diurnal along-bay (top) and across-bay (bottom) currents with respect to the wind and tide (Equations 4.7- 4.8). p-values are increasing to the right. Gray shading indicates significant p-values to a 10% level of confidence. The skill of the regression is in red.

the diurnal current fluctuations nearly everywhere. This is true to a lesser extent for the wind stress. The wind does not significantly improve the regression around 10 m depth at ADCP location 5 and 6 and over the whole depth at ADCP location 3 and 4. In the across-bay direction, the regression captures up to 80% percent of the kinetic energy but less on average than in the along-bay direction. The wind significantly explains cross-bay diurnal currents at all ADCP locations but 2 and between 10 and 15 m depth where an increase of wind p-value is mirrored by a dip of skill. The tide does not improve the regression except at depth of ADCP location 2,3 and 4.

4.3.3 Theoretical model configuration

The observed diurnal wind and tidal currents are compared with predictions of idealized theoretical models. These models are the ones of Winant (2007) and chapter 2. The idealized basin is 7km wide by 40km long by 30m deep and open on one side. The bathymetry is along basin uniform, with a cubic power law shape in the cross-basin direction. The model assumes that the basin is well-mixed and that the turbulent eddy viscosity is constant ($K = 3.10^{-3}\mathrm{m}^2/\mathrm{s}$). This model is different from the model used in section 4.2 in that there is only one basin instead of two connected basins. The reason is that the two basins were required in order to properly reproduce quarter-wavelength resonances. At diurnal frequency, both models lead to the same result and the simpler models is chosen.

4.3.4 Diurnal wind driven currents

The elliptical hodographs of the current forced by a 0.5 m amplitude diurnal sea level oscillations or an 0.05 Pa amplitude diurnal wind stress are computed by assuming respectively $(\zeta_{24}, \zeta_{24}^{90}) = 0.5 \times (\cos(\omega_{24}t), \sin(\omega_{24}t))$ or $(\tau_{24}, \tau_{24}^{90}) = 0.05 \times (\cos(\omega_{24}t), \sin(\omega_{24}t))$ in Equations 4.7- 4.8. The theoretical and observed hodographs are shown on Figure 4.4.

The amplitude of inertial theoretical current response is sensitive to the choice of turbulent eddy viscosity. For $K = 3 \times 10^{-3}\mathrm{m}^2/\mathrm{s}$, the amplitude of the theoretical ellipse is similar to the observed ones. This value of friction is intermediate, i.e. with an Ekman depth of 10 m, a third of the full depth and the wind driven response is expected to be affected by the rotation of the Earth. The current driven by a wind stress oscillating at the inertial frequency is near resonant, oscillating in the clockwise direction in time (chapter 2). This theoretical current is the result of a balance between the large barotropic inertial responses to wind stress and the axial pressure gradient. The axial pressure gradient arises from the presence lateral boundaries that cannot be crossed by the flow.

The observed wind driven ellipses have large ellipticity, with a predominant cyclonic sense of rotation, consistent with theoretical predictions. The current is also sheared along the vertical, with a reversal of the flow around 10m. The orientation of the ellipses is more to the right of the along-bay direction than in the theoretical model. This discrepancy is attributed to the partial failure of the regression to capture the along-bay wind driven currents. The linear regression probably does not distinguish tidal and wind driven along-bay currents successfully. At the bottom, the observed flow is damped but not as much as in the theoretical prediction, where the no slip boundary condition is a strong constraint. At ADCP 1 and 2, the wind driven current is aligned with the bathymetry and in phase with the wind, i.e. maximum downwind when the wind is strongest, and compares well with the theoretical model.

The tidal currents are very different from the wind driven currents. The ellipses are flatter and aligned with the along-bay direction. The phases are such that the tidal currents flow toward the closed end of BC at floods with a nearly uniform depth profile. The maximum values of the flow are found at mid-depth. The flow sense of rotation is predominantly clockwise with reversal at depth. This picture largely agrees with the theoretical predictions (orientation, phase, sense of rotation, flattened ellipses). The fact that the theoretical flow is intensified at the

surface and not at mid-depth is the only notable discrepancy.

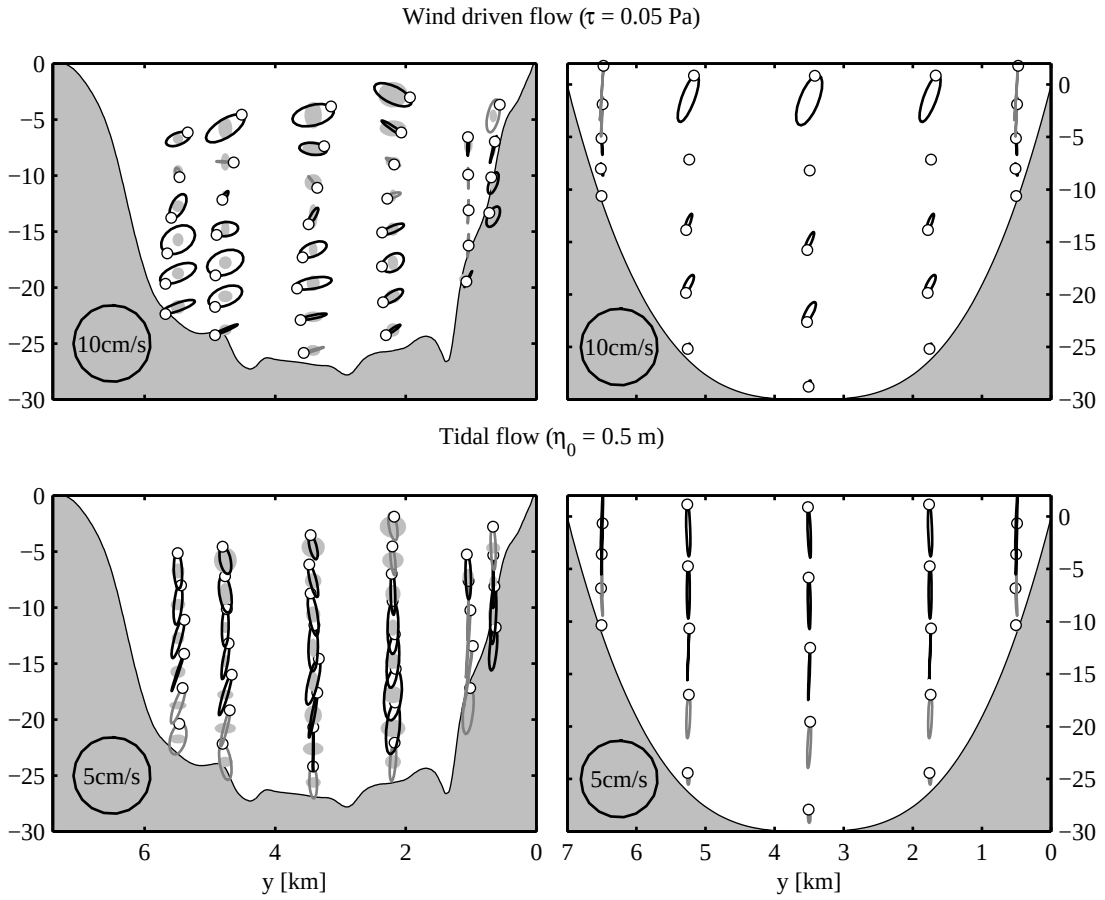

Figure 4.4: Comparison between observed (left) and theoretical (right) hodographs of current forced by a 0.5m amplitude diurnal sea level oscillation (top) and a 0.05Pa amplitude diurnal wind stress (bottom). Each cross-section is looking toward the closed end. The ellipse conventions are that up and left are x and y directions. Gray ellipses are counter-clockwise rotating currents, black clockwise rotating ones. White circles show the phase at flood or when the wind is maximum toward the closed end.

4.4 Dynamics

4.4.1 Depth-averaged momentum balances

As in section 3.4, along- and across-bay momentum balances are computed. The only two differences are that the wind stress at the south station instead of the north station is used and that the along-bay bottom pressure term is treated differently. The difference of bottom pressure between the closed and open end of the bay is only a proxy for the value of the pressure gradient at the center of the bay. In the diurnal band, the difference of bottom pressure is well correlated with the along-bay acceleration and it is scaled so that a linear regression between both leads to a slope of 1 at ADCP location 4. This correlation is a signature of the tidal signal that propagates as a surface gravity wave inside BC.

Along-bay direction

In the along-bay direction, acceleration and lateral advection of along-bay momentum are the largest terms on the western side of the bay (Table 4.2). They do not totally balance each other as indicated by the large residual standard deviation. A decomposition in frequency band shows that most of the momentum advection is due to a correlation between diurnal cross-bay currents and super-inertial along-bay currents. The wind stress is the next largest term. Close to the center, the accelerations' standard deviation is about half of its value on the western side. The Coriolis acceleration, wind stress and the lateral advection of momentum are smaller with similar standard deviations. Close to the eastern side, the acceleration and wind stress have the largest standard deviation. Acceleration and barotropic pressure gradient are significantly correlated at all ADCP locations. The slope of the correlation is by choice 1 at ADCP 4 and such that the acceleration overwhelms the pressure gradient on the shallow sides (slope of 6.4 on the western side). The wind stress and acceleration are significantly correlated at:

ADCP 1 with $r = 0.72$ and slope of 1.3; ADCP 2 with $r = 0.67$ and slope of 1.3; ADCP 3 with $r = 0.52$ and slope of 0.9; ADCP 6 with $r = 0.53$ and slope of 0.78. Along the western side, there is some correlation between the wind stress and the lateral advection of momentum (ADCP 1 with $r = 0.6$ and slope of 0.84; ADCP 2 with $r = 0.52$ and slope of 0.56).

Table 4.2: Diurnal band. Depth averaged momentum balance in the along-bay direction, $(10^{-5} cm/s^2)$

ADCP position	$-\partial_t[u]$	$f[v]$	$-\partial_x p/\rho_0$	τ_s^x/h	$-\tau_b^x/h$	$-\frac{1}{h}\partial_y(h[vu])$	residual
1	17.4	2.5	3.4	9.5	2.7	13.4	21.4
2	12.6	2.6	3.4	7.1	1.6	7.7	10.9
3	8.7	3.5	3.4	5.7	0.8	3.4	9.2
4	5.8	1.8	3.4	5.3	0.5	3.7	8.2
5	6.3	2.2	3.4	5.7	0.8	3.9	6.7
6	8.1	3.1	3.4	6.3	0.8	4.1	5.4

Across-bay direction

In the across-bay direction the baroclinic pressure gradient and the Coriolis acceleration are large and do not balance each other on the western side of the bay (Table 4.3). Both are expected to be balanced by independent cross-bay sea level slope fluctuations. This is similar to the sub-inertial case (section 3.4) and suggests that baroclinic pressure gradients need to be considered. Close to the center of the cross-section, the Coriolis acceleration and baroclinic pressure gradient terms are smaller while the acceleration becomes larger and dominant. The residual indicates that the momentum balance is better closed than in the other cases. On the eastern side, the Coriolis acceleration dominates. There is no significant one on one correlation between the terms that we can estimate from these observations. Overall knowledge of the lateral sea level slope would allow better closure the across-bay depth-averaged momentum balance.

Table 4.3: Diurnal band. Depth averaged momentum balance in the across-bay direction, standard deviations ($10^{-5} cm/s^2$)

ADCP position	$-\partial_t[v]$	$-f[u]$	$\tau_s^y/\rho_0 h$	$-\tau_b^y/\rho_0 h$	$-h[g\partial_y\rho/\rho_0(1+z/h)]$	$-\frac{1}{h}\partial_y(h[v^2])$	residual
1	3.0	17.7	3.4	0.7	14.3	6.7	24.4
2	2.8	14.2	2.5	1.0	12.0	4.4	17.5
3	3.8	10.0	2.1	0.4	1.1	2.9	11.6
4	2.4	7.3	1.9	0.5	3.9	2.7	9.7
5	2.4	8.1	2.1	0.6	2.6	3.5	10.3
6	3.4	8.9	2.3	0.8	5.8	4.1	11.5

4.4.2 3D momentum balances

As shown in section 4.3, the wind driven response is mostly baroclinic. Its signature on the depth-averaged momentum balance is therefore weak. Three dimensional momentum balance are thus computed next. Our attention is restricted to the central ADCP location (ADCP 4) where the residual standard deviation of the depth-averaged across-bay momentum balance is minimal (Table 4.3). The three dimensional momentum balance is given by

$$u\partial_x u + w\partial_z u - \frac{1}{\rho_0}\partial_z \tau^x = -\partial_t u + fv - v\partial_y u - \frac{1}{\rho_0}\partial_x p = R^x, \tag{4.9}$$

$$u\partial_x v + w\partial_z v - \frac{1}{\rho_0}\partial_z \tau^y = -\partial_t v - fu - v\partial_y v - \frac{1}{\rho_0}\partial_y p = R^y. \tag{4.10}$$

Terms on the left hand side of Equations 4.9- 4.10 cannot be evaluated with the present experimental set up. The vertical divergence of the turbulent stress could have been parametrized, e.g. as a function of the shear. This is not done here because the idea is to diagnose its amplitude as function of the terms that can be estimated. The axial advection of momentum is expected to be small in an elongated domain. Th bathymetry is flat near the center of BC and the vertical advection of momentum is neglected.

The pressure gradient is made of a barotropic and a baroclinic contribution:

$$\partial_x p(z) = \underbrace{\partial_x p_0 + \rho(z=0) g \partial_x \eta}_{\partial_x p_{bt}} + \underbrace{\int_z^0 g\partial_x \rho dz}_{\partial_x p_{bc}}, \tag{4.11}$$

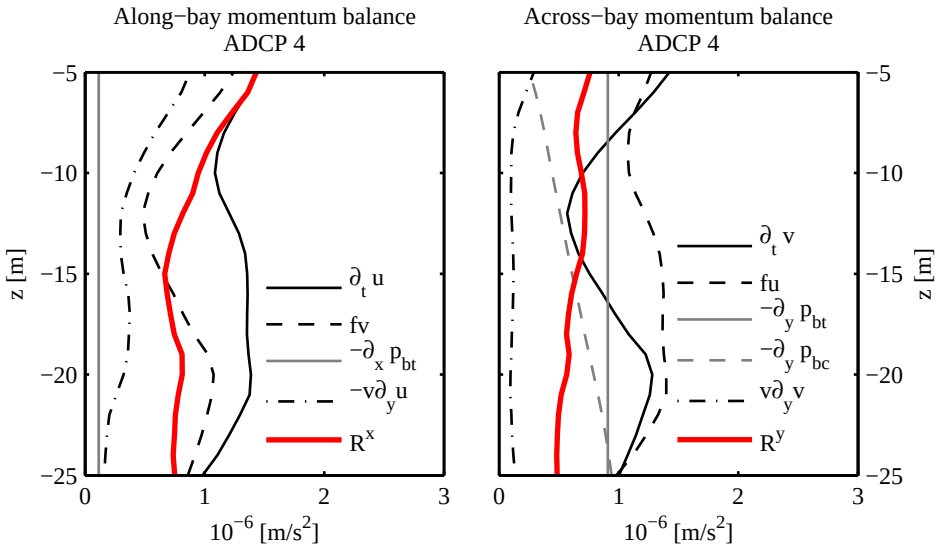

Figure 4.5: Standard deviations some of the terms involved in the along-bay (left) and across-bay (right) three dimensional momentum balance, ADCP position 4. The depth coordinate runs along the vertical axis.

with a similar expression in the cross-bay direction. As for the depth-averaged momentum balances, the along-bay baroclinic pressure gradient is unknown. In the across-bay direction, the barotropic pressure gradient is set as the residual of the depth-averaged momentum balance.

In the along-bay direction, the standard deviations of momentum acceleration and Coriolis acceleration are dominant at all depths (Figure 4.5). Both have one maximum at the surface and one at depth around 20 m deep. The acceleration of momentum has a somewhat larger amplitude with a flatter depth profile. The standard deviation of the residual R^x is similar to that of the two dominant terms which suggests a good correlation between both. The residual is maximal at the surface and monotonically decrease with depth. The lateral advection of along-bay momentum is significant and is predominantly due to an advection of the along-bay sub-inertial horizontal counter-clockwise circulation by the diurnal oscillations. The along-bay pressure gradient is of minor importance, which suggests that the

tide accounts for a small fraction of the picture just described.

In the across-bay direction, momentum acceleration, Coriolis acceleration and barotropic pressure gradient have the largest standard deviations. The maximal standard deviations are of similar size in the along- and across-bay directions ($\sim 10^{-6}\mathrm{m/s^2}$). There is again some vertical structure to both accelerative terms with maxima close to the surface and at depth. The baroclinic pressure gradient and residual terms have similar standard deviations. The amplitude of the baroclinic pressure gradient at the bottom is equivalent to a depth uniform horizontal density difference of $8\times10^{-3}\mathrm{kg/m^3}$ over a 2 km horizontal separation. Advection of momentum is the weakest term.

The direct effect of the wind is expected to appear as a divergence of the turbulence stress, for which we have no estimate. Instead, I use the wind stress normalized by the total depth ($\tau_s^x/30$ m) and compare it to the residual of the along-bay momentum balance with a least squares fit (Figure 4.6). The fit is significant in the upper 10 m of the water column with slopes increasing from 1 to 2. This strongly suggests that the along-bay dynamics are well captured there and demonstrates how momentum is spun up by the wind.

In the across-bay direction, the right hand side of the across-bay momentum balance ($\partial_t v - fu + v\partial_y v$) and the pressure gradient ($-\partial_y p/\rho 0$) are compared in a similar fashion (Figure 4.6). The skill of the fit is significant at all depth and the slope close to unity. This strongly suggests that the cross-bay dynamics are controlled by the combination of the barotropic and baroclinic pressure gradients.

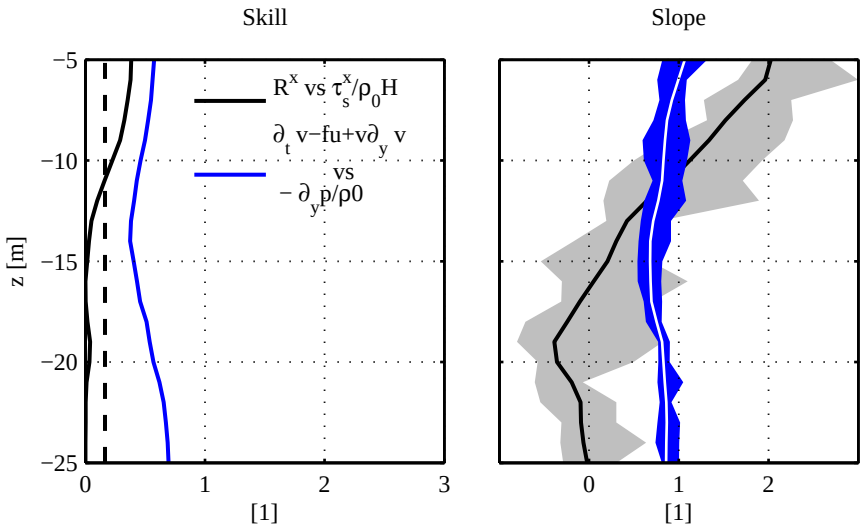

Figure 4.6: 3D Momentum balance, deployment 3, ADCP 4. Black and grey shading shows the skill and slope of a least squares fit of the along-bay momentum balance residual R^x against the normalized wind stress ($\tau_s^x/\rho_0 H$, H=30 m). Blue indicate for a least squares fit between left hand side of the across-by momentum balance ($\partial_t v - fu + v\partial_y v$) and the pressure gradient ($-\partial_y p/\rho 0$). The depth coordinate runs along the vertical axis, and the 95% confidence intervals are shaded.

4.4.3 Estimation of the turbulent stress

Vertical integration of Equations 4.9- 4.10 from a reference level, e.g. the bottom or the surface, to a level z leads to an estimate of the turbulent stress in the along- and across-bay directions, provided the turbulent stress is known at the reference level. It is then possible to relate turbulent stress and shear via a linear regression (Geyer et al., 2000). This was tried in the across-bay direction with an integration of the momentum balance from the surface down. A least squares fit between the subsequent stress estimate and the vertical shear is not significant, except between 5 and 10 m (Fig. 4.7). The corresponding turbulent eddy viscosity is between 1×10^{-3} and 3×10^{-3} m^2/s, which is consistent with the choices made in section 4.3.

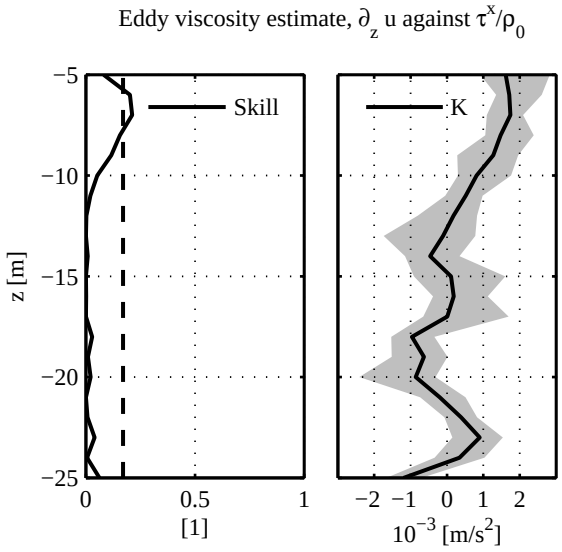

Figure 4.7: Regression between shear and turbulent stress inferred from reconstructed momentum balance in the cross-bay direction. The skill is on the left and the eddy viscosity, i.e. the slope of the regression, on the right.

4.4.4 Role of the variations of density

In the past section, we gained insight into the dynamics which take in the diurnal band. The direct forcing of the wind was quantified in the near-surface area. Barotropic and baroclinic pressure gradients are the main drivers. The next step toward a thorough understanding of the wind driven response is to understand how these pressure gradients are set up.

An EOF decomposition of the inertial plus super-inertial cross-bay flow at ADCP location 2 to 6 contains 48.5% of the kinetic energy in its first mode. This mode is intensified at the surface and sheared vertically with a reversal around 10 m depth (Figure 4.8). Its associated time series is diurnal and typical currents are of the order of 5 cm/s. This mode is characteristic of the wind driven response extracted in section 4.3.

An EOF decomposition of the inertial plus super-inertial density at the ADCP locations 2, 3, 5 and 6 captures 31.1% of the variance. As in section 3.6, we have subtracted first a horizontal average of the density at each vertical level and time. This eliminates the diurnal cycle of warming and cooling, which is expected to be horizontally uniform. The first EOF is a decrease of density on the western side of BC, largest around 10 and 15 m depth, and an increase of density along the eastern side. Typical density differences are 2×10^{-2} kg/m^3, which is more than what is required in order to account for the standard deviations of Figure 4.5.

Both EOF time series are well correlated, the first current EOF leading the density one by 3 h (based on a peak cross-correlation). The sense of the correlation is such that the density decreases in the direction of the surface flow. This makes sense if the water column is vertically stratified, so that a vertically sheared and mass balanced flow produces a loss of buoyancy in the direction of the surface flow. The good correlation between both EOFs is true in a lesser extent from 13-02 to 18-02, when diurnal current oscillations are present without much signal on the density EOF. The dynamics are then expected to be similar to the

well-mixed case developed theoretically in chapter 2.

After 22-02, the top to bottom density difference is of the order of $\Delta_z\rho$=0.25 kg/m^3. A vertically sheared flow similar to the cross-bay current first EOF has maximum velocities of the order of u_0=5 cm/s. Assuming linear profiles for both, the change of average density in half of a $W = 5$ km wide rectangular box is

$$\partial_t\rho = u_0\Delta_z\rho/3W. \tag{4.12}$$

The corresponding horizontal density difference is of the order of

$$\partial_t\Delta_y\rho = u_0\Delta_z\rho/3W \sim 0.14 \text{ kg/m}^3\text{/day}. \tag{4.13}$$

According to the preceding estimate, it takes 3.5 hours for a 0.02 kg/m^3 horizontal density difference to build up, which is close to the lag observed between the first EOFs of cross-bay currents and horizontal anomalies of density.

Assuming a linear vertical profile of density, the internal wave phase speed averages around c_ϕ=10 cm/s after 22-02. The corresponding mode 1 baroclinic Rossby radius is 1.5 km. BC is thus large enough to support inertial gravity waves with near-inertial waves with wave numbers of the order of BCs horizontal dimension. For a λ=10 km cross-bay wavelength and an along-bay uniform wave, the frequency of such a wave would thus be:

$$\omega = \sqrt{f^2 + (2\pi c_\phi/\lambda)^2} = 1.23 \text{ cpd}. \tag{4.14}$$

This frequency is well inside the broad bump of the baroclinic current spectrum on Figure 4.2. In the present case, the flow is continuously forced by the diurnal sea breeze and it is unclear wether the response is typical of a free wave. Comparison with a theoretical model of the type developed by MacKinnon and Gregg (2005) or Lerczak et al. (2001) would be useful at that point. Such models compute the time evolution of a baroclinic mode decomposition of the flow. A model/observation comparison of the currents, but most importantly of the dynamics, would be most beneficial.

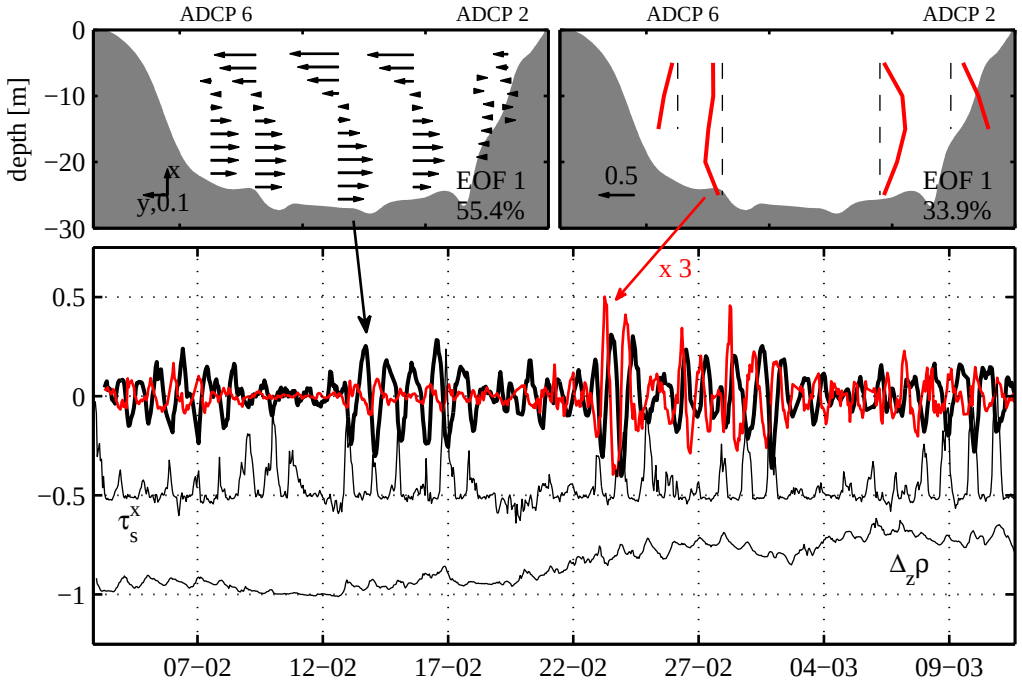

Figure 4.8: First EOF of high passed diurnal plus super-inertial cross-bay currents (top left) and density horizontal anomaly (top right). Corresponding time series are shown in the bottom panel along with wind stress at the south meteorological station and bottom-to-top difference of the horizontally averaged density. Note that the density EOF time series is scaled by a factor of 3.

4.5 Summary and conclusions

In this chapter, the along-bay sea level response of BC was first analyzed in the frequency domain. The necessity to distinguish between local and remote responses was explained. The local response is a set up in the downwind direction for frequencies up to BC quarter wavelength resonance frequency where the response is amplified. This compares well with theoretical predictions from the model developed in chapter 2.

There is a diurnal sea breeze inside BC and the associated wind driven current were then extracted for ADCP deployment 3. These currents are sheared vertically with maximum amplitude of 5 cm/s and rotate in the clockwise direction with time. This type of response is radically different from the tidal currents. It compares well with the theoretical model predictions of chapter 2, but for the fact that the observed cross-bay currents are larger relatively to along-bay currents. An analysis of the dynamics reveals that stratification is an important part of the dynamics. Cross-bay oscillations of density are well correlated with diurnal oscillations of cross-bay current, in particular during the second half of the deployment, when stratification inside the bay increased. Comparison between a process study with a theoretical or numerical model of the wind driven circulation under stratified conditions would be beneficial in the future. The role of nonlinear advection of momentum has not been addressed by this chapter. It was shown to be important along the western side of BC (Table 4.2- 4.3). A process study of its impact on the diurnal-inertial fluctuations, but also potentially sub-inertial ones, is of great interest. Similar studies were recently carried out in the tidal-estuarine case (Scully et al., 2009).

5

Observed response to sea level fluctuations

5.1 Introduction

The response of a semi-enclosed basin to sea level fluctuations at its mouth can be quite large and has motivated numerous studies (Taylor, 1921; Defant, 1961b; Hendershott and Speranza, 1971; Garrett, 1975; Miles, 1985). These imposed sea level fluctuations are usually of tidal origin, in which case the basin response is called the co-oscillating tide. This co-oscillating tide is distinct from and often larger than the basin direct response to astronomical forcing. The imposed sea level at the mouth is less frequently due to remote winds (Wong and Moses-Hall, 1998; Janzen and Wong, 2002), atmospheric pressure change (Vennell, 2007; Rabinovich and Monserrat, 1996), or seismic activity (Van Dorn, 1987; Satake and Shimazaki, 1988). BC is elongated with an average depth of 20 m giving a 193 km Rossby radius of deformation ($\sqrt{gh}/f$), which is much larger than its width. In such a basin, sea level fluctuations are expected to propagate as an irrotational shallow gravity wave in the along-bay direction. The effect of the rotation of the Earth is limited to a small sea level tilt in the cross-bay direction in

geostrophic balance with the along-bay flow (Gill, 1982). The sea level fluctuation eventually reflects against the head of the embayment and the response is typical of a standing wave, with out of phase current and sea level oscillations. At low frequencies, the gravity wavelength is long compared to basin length and the sea level oscillates quasi-uniformly. The associated currents are weak and can be estimated with tidal prism computations, i.e. a mass balance over the whole bay. With increasing frequency, the gravity wavelength shortens, more horizontal structure of the sea level is allowed and resonances eventually occur (Mei, 1989). In a rectangular basin with flat bathymetry, the gravest mode of resonance occurs when the bay is a quarter of the gravity wavelength. If BC is assumed to be rectangular with a depth of 20 m and a length of 40 km, this should happen at 7.6 cpd. For larger frequencies, the standing wave has a series of nodes and anti-nodes whose number increase with frequency. Friction smears out nodes and antinodes of the standing wave and decreases the amplitude of the response (Winant, 2007). The resonances are damped by friction.

The investigation of three dimensional structure of the sea level forced response started later (Ianniello, 1977). At the time, the emphasis was on explaining the tidal residual circulations. An important aspect of the three dimensional response is the existence of secondary (cross-channel or transverse) currents (Buijsman and Ridderinkhof, 2008; Lerczak and Geyer, 2004). These currents arise from several mechanisms: transverse density gradients, channel curvature and Coriolis forcing. They are weak and mass balanced vertically, but may be relevant for the mixing and dispersion of momentum and tracers (Fischer, 1973; Chant, 2002).

As explained in chapter 1, little is know about the physics inside BC. An exception is Obeso-Nieblas et al. (1996) who studied the tide inside BC numerically and observationally with pressure sensors and current meters. The observations were short, less than 3 days each, and no tidal analysis was therefore possible. The numerical model grid was coarse, 1.5 km, and used an approximate bathymetry. The most valuable information from this work is the values of the tidal current at

the mouth, around 20 cm.s^{-1}, much larger than what we observed further inside the bay as will be shown in the present analysis.

This chapter investigates BC response to sea level fluctuations at its mouth. These sea level fluctuations are predominantly of tidal origin. Sea level and current responses are studied separately. The analysis of the sea level response is based on a comparison between the sea level at both ends of the bay. The current response consists of a comparison between depth-averaged and three dimensional currents and the sea level at the mouth of BC. Observational results are compared with theoretical models. This analysis is limited to the winter time period as in earlier chapters.

5.2 Sea level response

5.2.1 Sea level forcing

Sea level is inferred from bottom pressure measurements assuming a constant density of 1025 kg/m^3. Winter time maximal fluctuations of density are of the order of 0.2 kg/m^3, roughly equivalent to 1°C. Over the instruments' depth range, this leads to a 1 mm difference, which is neglected in this chapter. The spectra of sea level and detided sea level indicate that the diurnal and semi-diurnal tidal harmonics are well captured by the harmonic analysis (Figure 5.1, upper panel). All spectra exhibit a broad bump between 3 and 7 cpd peaked at integer frequencies harmonics of the principal tidal constituents. The bump is larger at the closed end relative to the mouth. Some energy is captured by the tidal analysis at 3 and 4 cpd. The tidal analysis is unable to explain fluctuations at higher frequencies, as peaks of the full sea level and detided sea level spectra overlap.

In order to assess the relationship between sea level fluctuations at BC's mouth (η_n) and closed end (η_s), I computed the coherence and transfer function

between both time series (Emery and Thomson, 2001):

$$C_\eta^2(f) = \frac{| < N_n^\dagger N_s > |^2}{< N_n^\dagger N_n >< N_s^\dagger N_s >}, \tag{5.1}$$

$$H_\eta(f) = \frac{< N_n^\dagger N_s >}{< N_n^\dagger N_n >}, \tag{5.2}$$

where $< \cdot >$ is an average over fft blocks, † the complex conjugate operator, f the frequency, N the Fourier transform of the sea level η, $C^2(f)$ the square coherence and H_η the transfer function. The gain G_η of the transfer function is its absolute value, its phase lag ϕ_η is its complex phase ($H_\eta = G_\eta e^{i\phi_\eta}$).

The detided sea levels at the south and mouth of BC are significantly coherent over a broad range of frequencies (Figure 5.1). Coherence minima are associated with dips of the sea level spectra. The transfer function gain and phase are typical of a standing wave in a semi-enclosed basin (Mei, 1989). At low frequencies, the basin is short compared to the shallow water gravity wavelength and the sea level at the closed end and mouth oscillates with similar amplitude ($G_\eta = 1$) and in phase ($\phi_\eta = 0$). For larger frequencies, there is an amplification of the sea level at BC's closed end ($G_\eta > 1$). The phase is weak and slowly increasing. The tidal constituents' amplitude ratios and phase differences follow a similar trend (blue crosses on Figure 5.1). Around 5 cpd, there is a peak of gain ($G_\eta \sim 8$) associated with a 180° phase shift. This is expected to be the quarter wavelength resonance of BC. Between 6 and 20 cpd, the gain is less than unity, meaning that the sea level is damped at the closed end. The phase varies abruptly owing to the lower coherence. Around 20 cpd, there is a peak of coherence and gain with a 180° phase shift. At higher frequencies, there are peaks of coherence but the gain remains less than unity.

The observed response is compared next with theoretical predictions from idealized modes described in Appendix 5.5. The first theoretical model ($H_{\eta,1}$) predicts the frictionless sea level response inside a narrow 40 km long by 20 m deep rectangular flat bay. The gain and phase of $H_{\eta,1}$ are represented by the full red line on Figure 5.1. The two other models ($H_{\eta,2/3}$) predict the response inside a

basin with a more realistic geometry and friction ($K = 4.10^{-3}$ and 1.6×10^{-2} m^2/s).

At low frequencies ($f < 2$ cpd), all models are successful at reproducing the uniform fluctuations of sea level inside the bay. Near the quarter wavelength, the increase of gain is reproduced by all three models, while the phase increase is only predicted by model 2 and 3. The peak of gain is infinite for model 1 due to lack of friction. It is shifted to 7.6 cpd, which we explain by the non-rectangular shape of BC. In order to reproduce a quarter wavelength resonance at 5 cpd, model 1 requires a depth of 9 m for a length of 40 km and a length of 60 km for depth of 20 m.

Introducing width variations as done with model 2 and 3 is a more efficient way to reconcile the observed and predicted gravest frequency of resonance. The dimensions of the sub-basins (2.5 km by 13 km and 6 km by 27 km) for models 2 and 3 were chosen to roughly match BC's dimensions and lead to resonance at 5 cpd. The sensitivity of this choice is not addressed here. The values of turbulent eddy viscosity have been chosen such that the gain of model 2 and 3 are respectively upper and lower bounds for the observed gain. The choice of eddy viscosity does not significantly offset the frequency of resonance. Past resonance, the observed damping of the sea level at the closed end ($G_\eta < 1$) is reproduced by models 2 and 3 but not my model 1. At 20 cpd and 40 cpd, the observed 180° phase shifts are again reproduced by the three theoretical models. The modeled gain overpredicts the amplification of the sea level at the closed end at these frequencies. This might indicate a stronger increase of friction with increasing frequency than that modeled with a constant eddy viscosity model. Among the four peaks of coherence between 20 and 50 cpd, the theoretical models explain only two of them. We speculate that the remaining two others are due to the shape and bathymetry of BC and could be modeled with a more realistic numerical model.

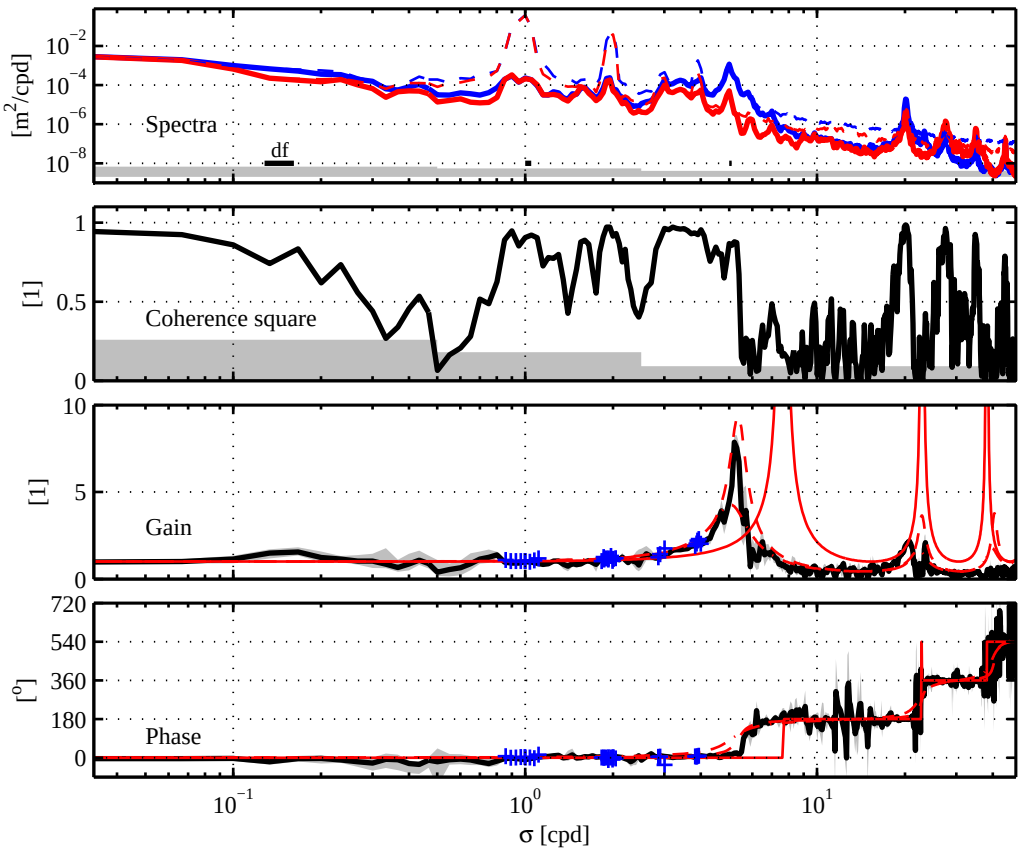

Figure 5.1: Top panel: spectra of sea level at the north (red) and south (blue) stations. The spectra of the raw sea level are dashed and the spectra of the detided sea level is full. Second panel: squared coherence between detided sea level at the south and north of BC. Third panel: gain of the detided sea level between south and north stations. A gain larger than 1 corresponds to an amplified sea level signal at the south. The blue crosses are the ratio of tidal constituents amplitudes at the south with respect to the north. Bottom panel: phase of detided sea level between south and north station. A positive phase is a delay at the south station with respect to the north. Blue crosses are the phase difference between tidal harmonics. On all four axes, the gray shading represents a 95% confidence interval or significance level. The full red lines are the theoretical prediction for a rectangular basin; dashed and dotted dashed lines are the theoretical predictions for a theoretical model with two interconnected basins with an eddy viscosity of 4×10^{-3} and 1.6×10^{-2} respectively.

5.3 Current response

5.3.1 Deployment 1

Depth averaged currents

Along-bay depth-averaged currents at location C and E are coherent with sea level fluctuations at BC's mouth around principal tidal frequencies as well as harmonic frequencies (Figure 5.2). There is a broad bump of coherence from 3 to 6 cpd. Around 20, 28, 35 and 44 cpd, there are isolated peaks of coherence. This picture is overall similar to the coherence between sea level at the closed end and mouth (Figure 5.1), except for lower coherence values. The coherence is similar at both ADCP locations but for the diurnal and semi-diurnal frequency bands. The coherence at ADCP E is lower than at C, which shows that contributions from other forcings, e.g. winds, may be more important there. In the across-bay direction coherences are much lower. Significant but weak (<0.6) peaks of coherence are observed at diurnal and semi-diurnal frequencies. The sea level driven current fluctuations finally account on average for 60% of the kinetic energy in the along-shore direction (current standard deviations vary between 2 and 3 cm/s). They account on average only for 11% of the kinetic energy in the across-bay direction (1 to 2 cm/s standard deviations).

At low frequencies, far enough from the quarter-wavelength resonance, the sea level is oscillating up and down nearly uniformly over BC. A mass balance between mass flux and BC's volume time rate of change leads to a scaling inversely proportional to the frequency. The theoretical response reproduces well this scaling (Figure 5.2). As far as observations are concerned, only diurnal and semi-diurnal frequencies are outside the quarter wavelength cone of influence of the resonance. There are few points with significant coherence at such low frequencies, which are consistent with theoretical predictions but not enough to reproduce the linear dependence on frequency. Sea level and current is expected to be in quadrature

advance (phase of -90°) with the sea level. This phase relationship is well matched by the theoretical model and within 30° for the observations.

Around the quarter wavelength resonance (5 cpd), the gain peaks with maximum value around 2 m/s for 1 m amplitude fluctuations at the mouth. The peak is bounded by theoretical predictions of Appendix 5.5 with eddy viscosities of 10^{-3} and 10^{-2} m^2/s. The phase between sea level and current undergoes a 180° phase shift at resonance, which is theoretically predicted and reproduced by the observations. Past this first resonance, there is little coherent signal except for three peaks. The first occurs at 20 cpd and is a maximum of the gain. It is the second resonance when BC's length is 3/4 of the surface gravity wave wavelength. The observed amplitude of the resonance is similar to the first one and bounded again by theoretical predictions if for a frequency offset. A 180° phase shift is again observed. Other peaks of coherence and associated gain and phase are difficult to make interpret. Lateral resonances are expected to show up around 700 cpd, equivalent to 12 min oscillations, which is lower than the sampling interval.

3D currents

The squared coherence between 3D currents and sea level fluctuations at BC's mouth is similar to the coherence between depth-averaged currents and sea level fluctuations (Fig 5.3). For along-bay currents, it is significant at principal tidal frequencies and their multiples as well as around 20, 28 and 44 cpd. The diurnal squared coherence is lower than in other frequency bands. Across-bay currents are barely significantly coherent with sea level fluctuations inside diurnal and semi-diurnal frequency bands.

The sea level driven along-bay currents are scaled by $u_0(\sigma) = g\eta_x/\sigma$, where η_x is the along-bay sea level gradient calculated from the theoretical model and σ the forcing frequency. This follows an idealized along-bay momentum balance between acceleration and pressure gradient. The currents have been averaged in each frequency band and are shown on Figure 5.4, along with theoretical pre-

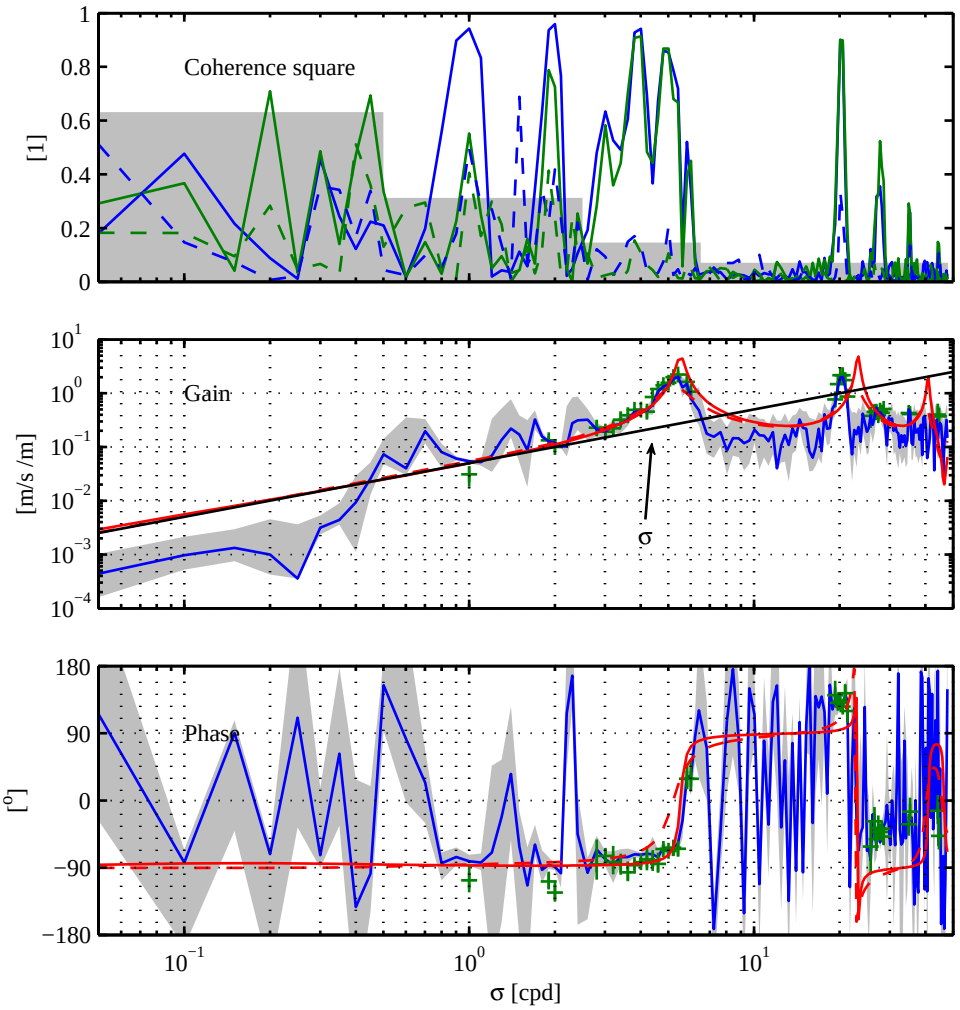

Figure 5.2: Sea level forced depth-averaged currents, deployment 1, ADCP location C (blue) and E (green). Top panel is coherence squared between along- (full) and across- (dashed) depth-averaged current and sea level at the mouth of BC. Central and bottom panel are gain and phase of the along-bay depth-averaged current transfer function. Green crosses are for location E when the coherence is larger than 1.5 times the critical level of coherence. Red lines are predictions from the theoretical model for K=10^{-3} m^2/s (full) and K=10^{-2} m^2/s (dashed). 95% confidence intervals are indicated by the shading for location C and the length of the vertical length of the crosses for location E.

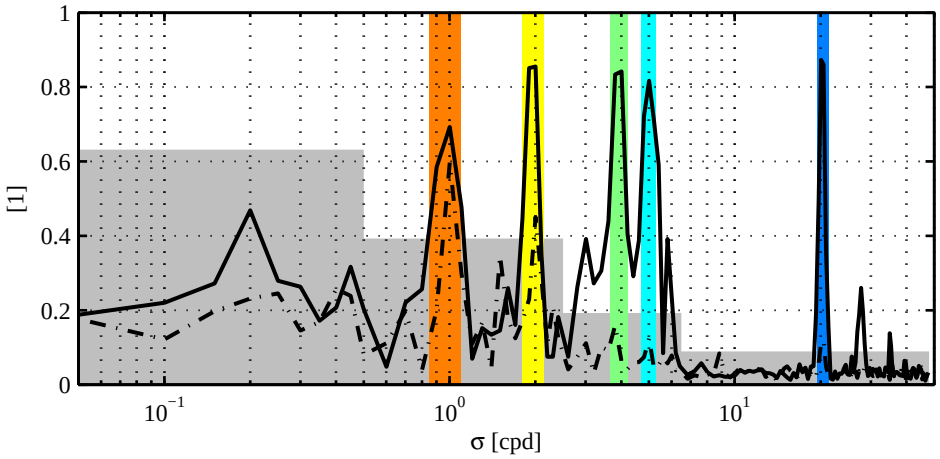

Figure 5.3: Deployment 1, squared coherence between sea level and current fluctuations averaged over depth and ADCP locations C and E. Along shore currents are full black, cross-bay currents dashed black. 95% significance level is grey. Color shading defines frequency bands used on Figures 5.4- 5.5.

dictions (Appendix 5.5, K=10^{-3} m^2/s).

In all selected frequency bands, the observed amplitudes of sea level driven currents are within 50% of u_0. Agreement with the amplitude of theoretical currents is similar. Observed phases agree within 30° with theoretical predictions in the 4, 5 and 20 cpd frequency bands. In the diurnal and semi-diurnal bands, the predicted phases are within 50°. Confidence intervals of both amplitude and phase are larger at diurnal and semi-diurnal frequencies, in particular at location E. This indicates higher noise levels in these bands or departure from stationarity or linearity of the sea level response.

The theoretical vertical structure consists of a bottom boundary layer whose thickness decreases with frequency ($\delta = \sqrt{K/\sigma}$) and a core with nearly depth-uniform currents. In the 4, 5 and 20 cpd frequency bands, the boundary layer is too small to be resolved by the bottom most ADCP bins. The core of the current profile is instead well reproduced by observations. At location C, the amplitude of diurnal currents shows a bottom boundary layer. An hint of bottom

boundary layer is also observed in the semi-diurnal band even though confidence intervals are large. At location E, the large confidence intervals prevent discussion of the vertical profiles.

Across-bay currents driven by sea level fluctuations are scaled by $v_0 = u_0 f/\sigma$ according to a non-dimensionalization of the along-bay momentum balance. The current amplitude is in general larger than the theoretical amplitude, by a factor of 2 for diurnal frequencies and a factor of 10 for semi-diurnal frequencies (Figure 5.5). The vertical structure is similar with a minimum at mid-depth. Confidence intervals are large, in particular in the semi-diurnal band. Observed and theoretical phases largely differ from one another. Confidence intervals of observed phases are large, around 90°. The theoretical vertical structure of the phase consists of an increase of phase upward with flattening near the surface, which we do not observe in the observations. Characteristics of the across-bay currents strongly depend on the defined orientation of the along- and across-bay directions. I have not managed to choose an orientation leading to better agreement between theory and observations.

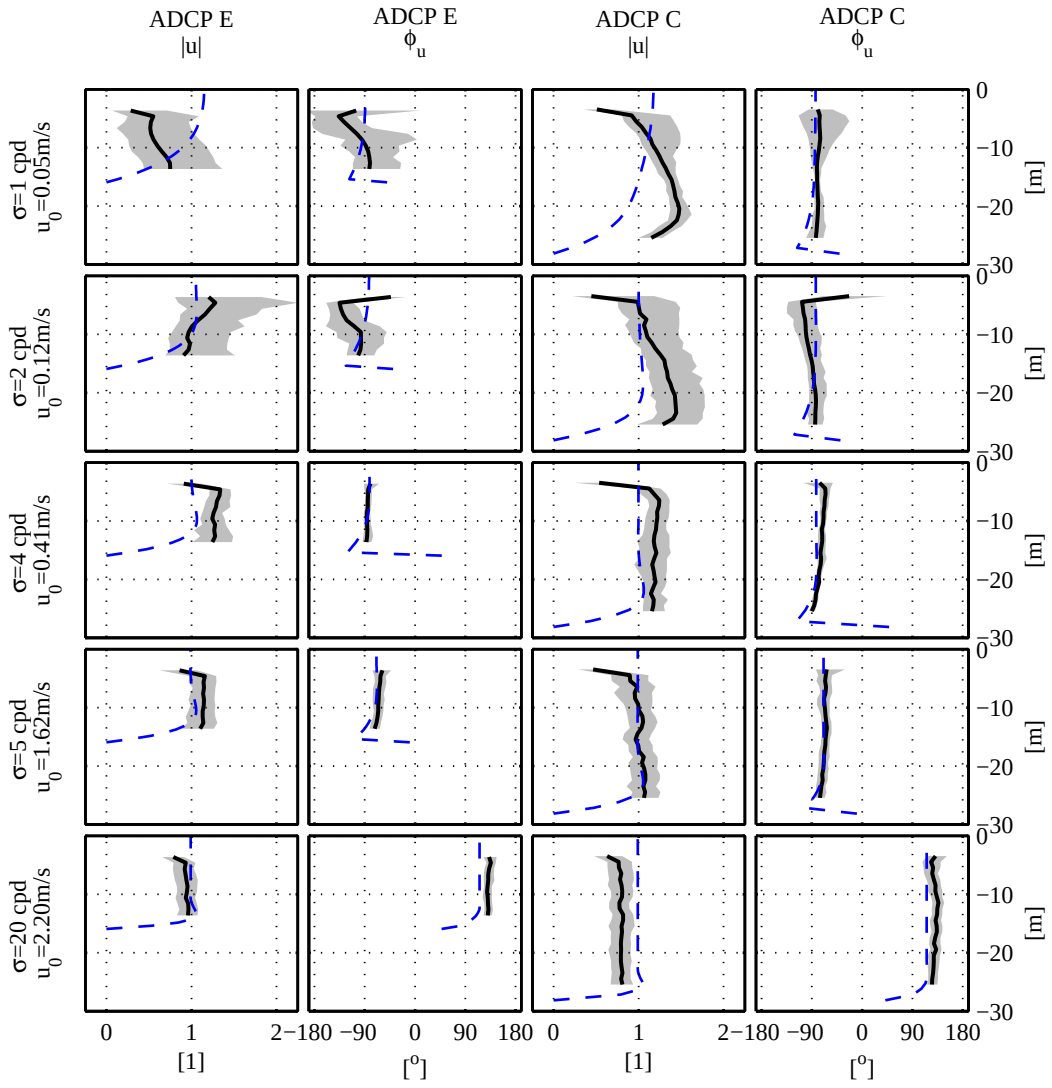

Figure 5.4: Deployment 1, along-bay currents forced by a 1 m fluctuation of sea level at BC mouth as a function of depth (vertical coordinate). The current response is averaged in frequency bands. The currents are described by their amplitude $|u|$, scaled by $u_0 = g\eta_x/\sigma$, and phase in degrees. Gray shadings are 95% confidence intervals. Blue dashed line is the theoretical prediction for $K = 10^{-3}$ m^2/s.

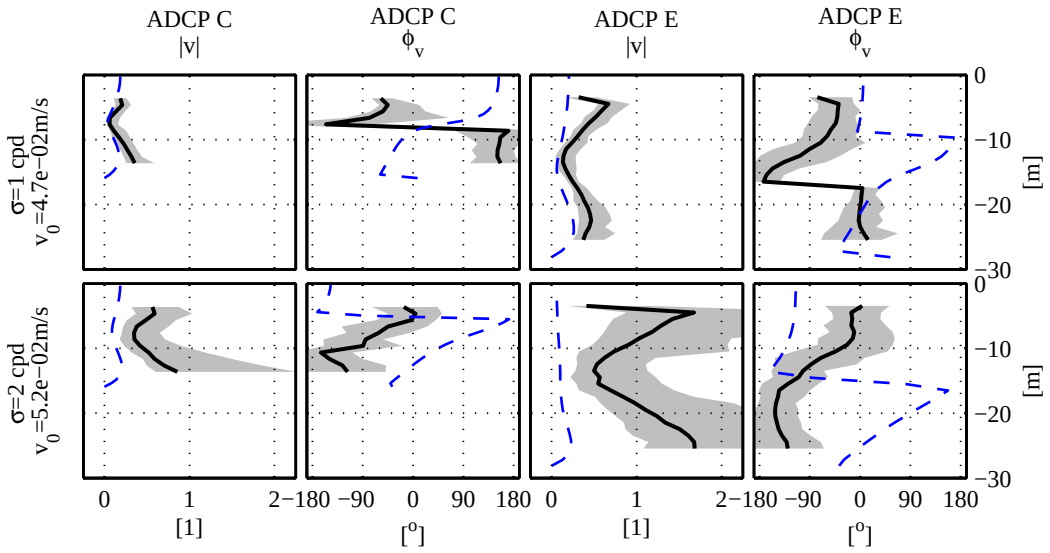

Figure 5.5: Deployment 1, across-bay currents forced by a 1 m fluctuation of sea level at BC mouth as a function of depth (vertical coordinate). The current response is averaged in frequency bands. The currents are described by their amplitude $|v|$ scaled by $v_0 = g\eta_x f/\sigma^2$ and phase in degrees. Gray shadings are 95% confidence intervals. Blue dashed line is the theoretical prediction for $K = 10^{-3}$ m^2/s.

5.3.2 Deployment 3

Depth averaged currents

During deployment 3, the coherence squared between fluctuations of depth-averaged current and sea level is shown on Figure 5.6. It is nearly identical to that during deployment 1. For along-bay currents, significant peaks of squared coherence are found at multiples of the principal tidal frequencies, with a broader bump around 5 cpd, as well as at 20, 28, 35 and 44 cpd. Across-bay currents are not significantly coherent except around the second resonance at 20 cpd.

The gain and phase of the transfer function between along-bay currents and sea level have been averaged within 5 frequency bands where high squared coherence are found. These frequency bands are color coded in Figure 5.6. Gain and phase are shown as a function of ADCP location and compared with band averaged theoretical predictions (Appendix 5.5, K=10^{-3} m^2/s). Observed gain increases with frequency and matches reasonably the theoretical predictions. The theoretical predictions fail however to reproduce a westward increase of gain. This gain increase is in between frequency bands. The ratios of gain between ADCP 1 and 6 are, from low to high frequencies, 1.62, 1.24, 1.42, 1.40 and 1.39. This amplification of the current along the western side is most likely driven by the shape of the western coastal boundary. The phase between sea level fluctuations is as expected around $-90°$ and increases with frequency. Agreement with theoretical predictions is within confidence intervals (20° wide on average). No significant spatial trends are observed.

3D currents

The squared coherence between currents and sea level fluctuations is similar to that during deployment 1 (Figure 5.3) and thus not shown. Significant coherences for along-bay currents are observed at principal tidal frequencies as well as their multiples and 20, 28 and 44 cpd. Across-bay currents exhibit weak

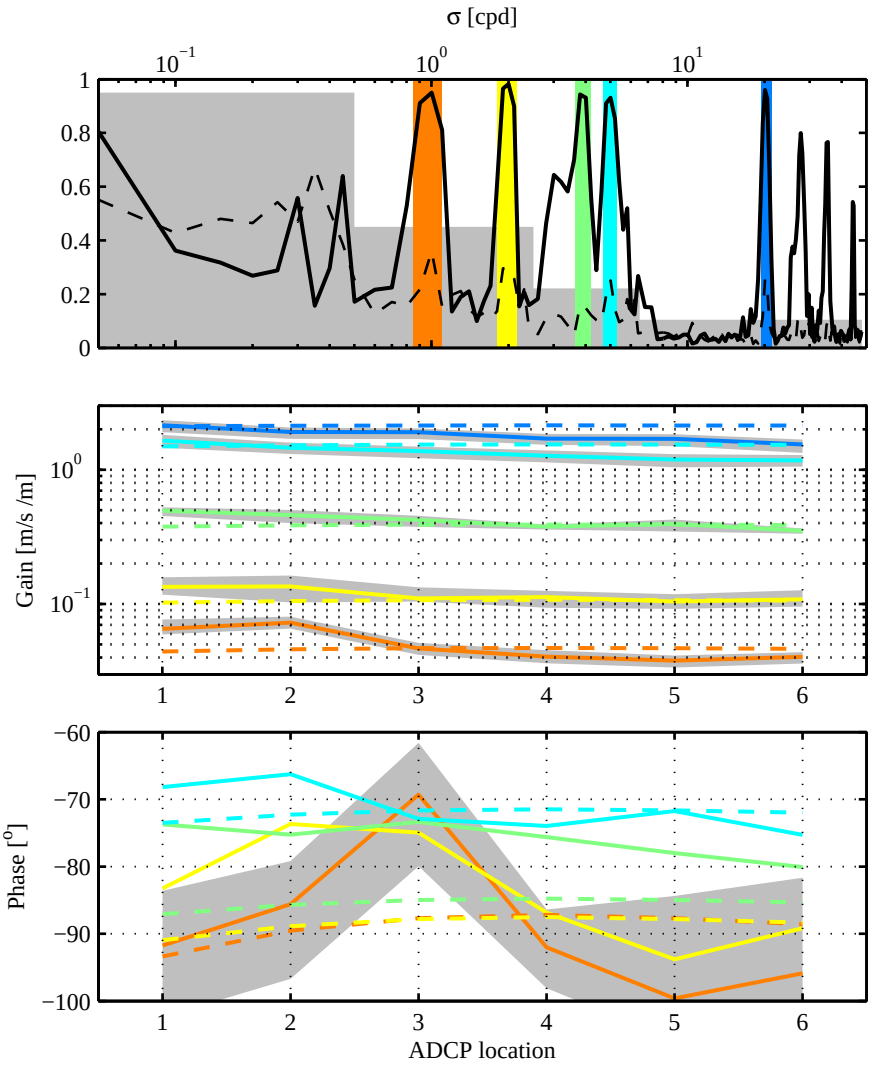

Figure 5.6: Sea level forced depth-averaged currents, deployment 3, ADCP location 1 to 6. Top is coherence squared between sea level at BC mouth and along-(full) and across-(dashed) depth-averaged current, averaged over ADCPs 1 to 6. Grey shading indiacte 95% level of significance and color shading indicates frequency bands selected for lower axes. Central and bottom plots show gain and phase of the current response to sea level as a function of ADCP location. Dashed lines are theoretical estimates with an eddy viscosity of $K = 10^{-3}$ m^2/s. Gray shadings are 95% confidence intervals.

but significant squared coherence with sea level fluctuations in the diurnal and semi-diurnal frequency bands.

The amplitude of along-bay currents is normalized by u_0 as for deployment 1. In the diurnal frequency band, the currents observed at ADCP 4 to 6 are consistent with theoretical predictions and with u_0 (Figure 5.7). At ADCP 1 to 3, the magnitude of currents is within u_0 by a factor of 2, which is a significant difference given the calculated confidence intervals. The current vertical structure shows a bottom boundary layer at ADCP 1 to 4 with a thickness comparable to the theoretical one. At ADCP 1 to 3 there is however a decrease of the current toward the surface and the current is maximum between 10 and 15 m depth. Along with the intensification of the flow already observed from depth-averaged currents, these are the two most important departure from theoretical predictions.

The agreement between currents and u_0 and theory improves with increasing frequency. The vertical structure of currents is flatter compared to the diurnal case, which is consistent with theory. Bottom boundary layers are barely observed along the western side (ADCP 1 and 2). Confidence intervals are larger in the semi-diurnal band than in any other frequency bands. They are thinnest in the 4 cpd band where the amplification of currents along the western side is slight but significant.

Phases between along-bay currents and sea level have not been shown. The agreement with theory is similar than for deployment 1 and increases with frequency as for the amplitudes just described. The width of phase confidence intervals also decreases with frequency.

Across-bay currents are difficult to make sense of as for deployment 1. The amplitude of observed currents scales as v_0, larger than what is predicted by theory (Figure 5.8) At diurnal frequencies, there are two maxima along the water column. The phase is noisy along the depth coordinate and bears little resemblance with theory. Confidence intervals of amplitude and phase are large, in particular at semi-diurnal frequency.

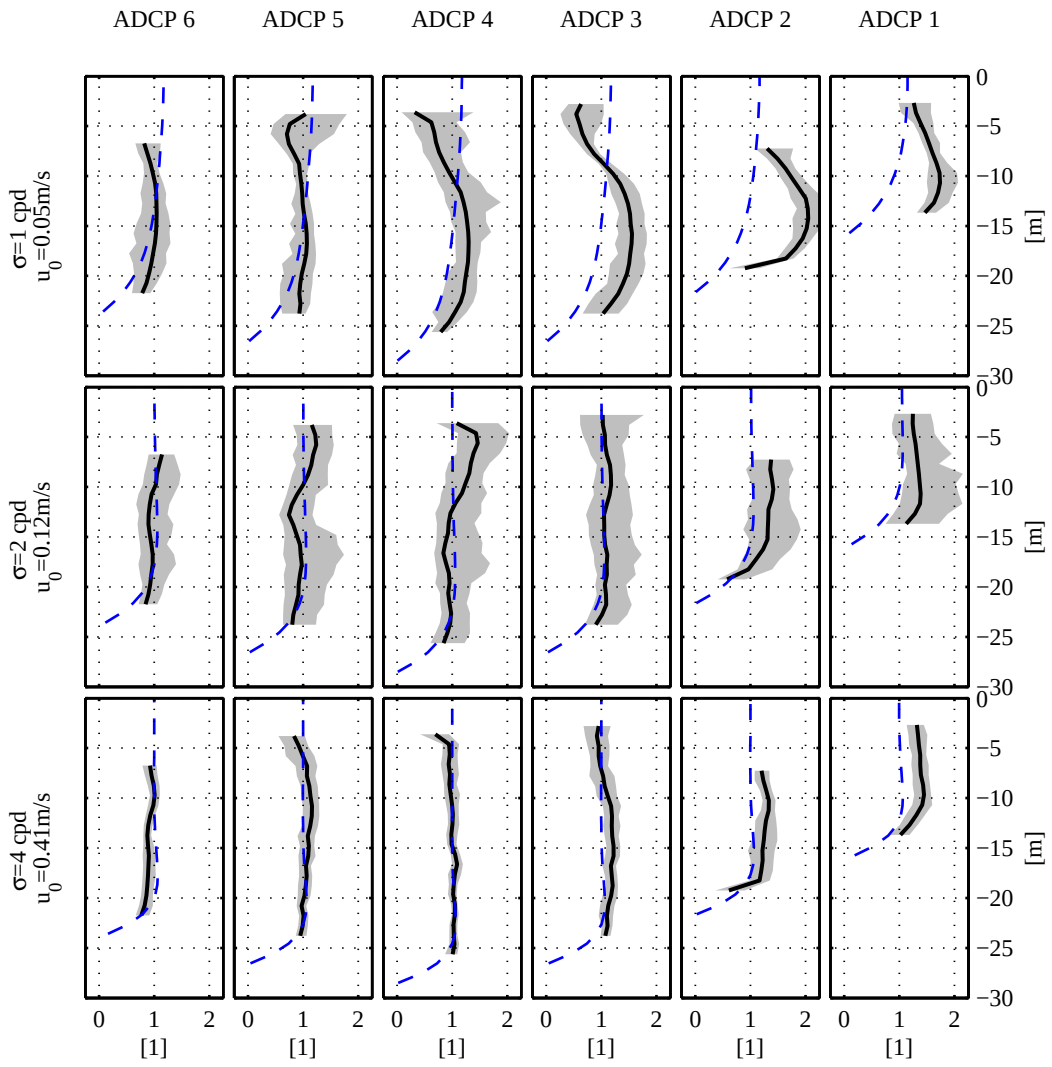

Figure 5.7: Deployment 3, along-bay current amplitude forced by a 1 m fluctuation of sea level at BC mouth as a function of depth (vertical coordinate). The current response is averaged in frequency bands (vertical axes position, frequency increasing downward). The current amplitude $|u|$ is scaled by $u_0 = g\eta_x/\sigma$. Gray shadings are 95% confidence intervals. Blue dashed line is the theoretical prediction for $K = 10^{-3}$ m^2/s.

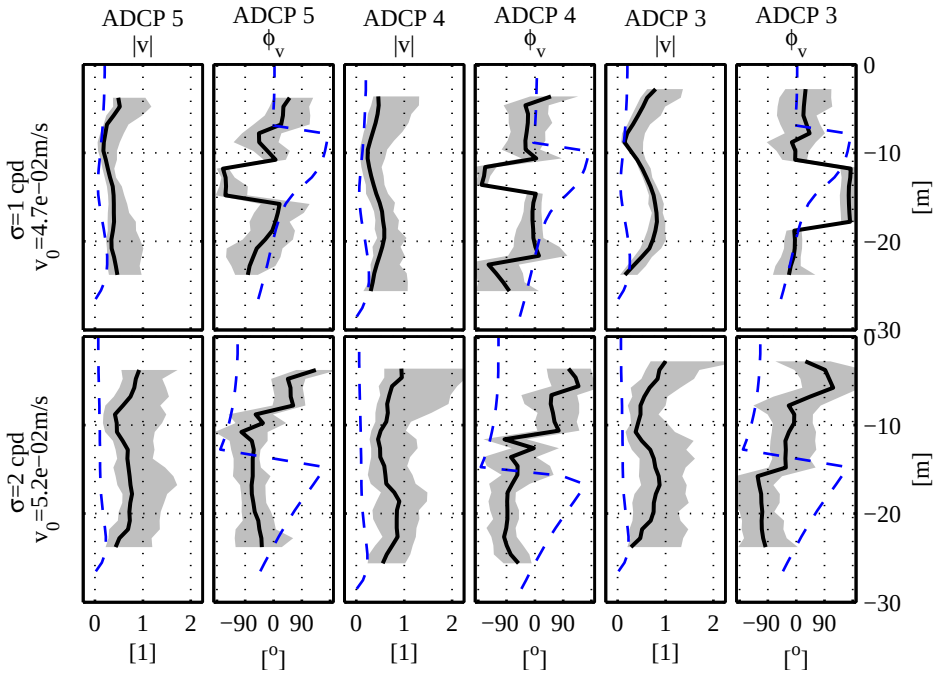

Figure 5.8: Deployment 3, across-bay current amplitude forced by a 1 m fluctuation of sea level at BC mouth as a function of depth (vertical coordinate). The current response is averaged in frequency bands (vertical axes position, frequency increasing downward). The current amplitude $|v|$ is scaled by $v_0 = g\eta_x f/\sigma^2$. Gray shadings are 95% confidence intervals. Blue dashed line is the theoretical prediction for $K = 10^{-3}$ m^2/s.

5.4 Conclusions

In this chapter, sea level fluctuations at the north and south bottom pressure stations were first compared as function of frequency. The agreement is good from the lowest resolved frequencies to 6 cpd and at isolated frequencies between 20 and 50 cpd. A quarter wavelength resonance has been identified around 5 cpd, with strong amplification of the sea level at the closed end compared to the mouth. A theoretical model with two interconnected basins was successful at reproducing the observed current response.

Current and sea level fluctuations were next compared as a function of frequency during deployments 1 and 3. Along-bay currents are coherent with sea level fluctuations over the same frequency bands as just mentioned. The amplitude and phase of the current closely followed theoretical predictions. The poorest agreement occurred in the diurnal and semi-diurnal bands. The signal-to-noise ratio is decreased in these bands by other mechanisms. An amplification of the along-bay current along the western side of BC was observed. Across-bay currents were weakly coherent with sea level fluctuations in the diurnal and semi-diurnal bands. The associated current amplitude was larger than predicted with similar vertical structure. No sense could be made of the phases.

The questions of how and where the high frequency (>4 cpd) fluctuations are created are still open. A numerical simulation of the tidal response of BC could determine whether the generation is local (e.g. funneling of the flow at the mouth, reflection at BC's closed end). The amplification of the flow along the western side of BC could also be addressed by such a model.

5.5 Appendix: theoretical model

The simplest theoretical model of the sea level response to sea level forcing at the mouth assumes BC is rectangular and 40 km long by 20 m deep. No further assumptions are required on BC's width except for its being much smaller than the Rossby radius of deformation. This model is used on Figure 5.1. The transfer function between the closed end (S) and mouth (N) of BC is then:

$$H_{\eta,1}(f) = \frac{\eta_S(f)}{\eta_N(f)} = \frac{1}{\cos\left(fL/\sqrt{gH}\right)} \tag{5.3}$$

where L and H are the length and depth of BC.

A better match between the first resonant frequencies was found by using a more realistic representation of BC geometry (Figure 5.9). Two basins of parabolic cross-section are connected. The basin closer to the mouth has width of 2.5 km and long as a third of 40 km. The second basin is wider (6.5 km) and long as two thirds of 40 km.

The theoretical model used includes friction and is similar to Winant (2007) and that of chapter 2. We include in this appendix the effect of wind stress because the same model is used with wind in chapters 3 and 4. The friction enables matching the amplitude of the resonance of the gravest resonance. Within the classical assumption of this model (small width compared to length, periodic forcing), the complex amplitude of the vertically integrated flow is:

$$[U] = M^N \partial_x N + M^{T^x} T^x + M^{T^y} T^y, \tag{5.4}$$

$$[V] = 0. \tag{5.5}$$

(M^N,M^{T^x},M^{T^y}) are given by Equations 2.27- 2.29. N is the complex amplitude of sea level and (T^x,T^y) are the complex amplitudes of the wind stress (set to zero in the case of sea level forcing). The vertically integrated continuity equation is averaged along the width of the bay ($< \cdot >$) and N satisfies:

$$< M^N > \partial_{xx} N + (\kappa\mu)^2 N = -\partial_x \big(< M^{T^x} > T^x + < M^{T^y} > T^y \big) \tag{5.6}$$

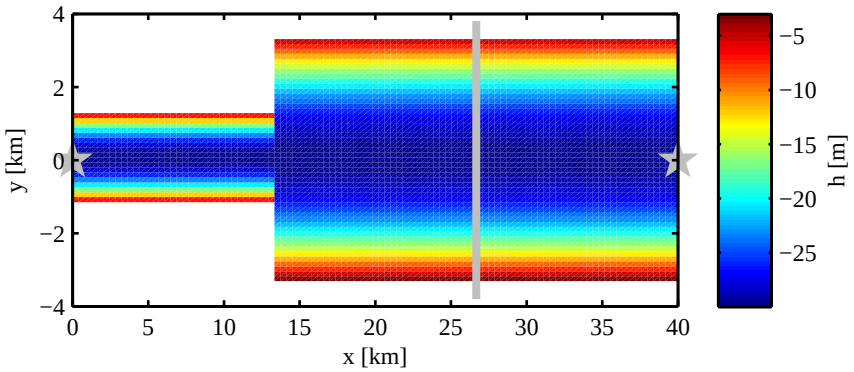

Figure 5.9: Bathymetry used for the interconnected basin configuration. The stations used in order to compare sea level responses on Figure 5.1 are represented by the pentagrams. The vertical gray line represent the location of the ADCP transect where theoretical current estimates are made.

μ is given by Eq. 2.26. Equation 5.6 is solved analytically inside each sub-basin. Boundary conditions are no transport through the closed end ($< [U] >= 0$), continuity of transport between each basin ($< [U] >_1 = < [U] >_2$), and imposed sea level at the mouth ($N = 0$ for wind driven cases, $N = 1$ for sea level forced ones).

The sea level transfer function is then expressed as:

$$H_{\eta,2/3} = N(x = L) \tag{5.7}$$

Indices 2 and 3 designate the two possible values of the eddy viscosity used in section 5.2.1: $K_2 = 4 \times 10^{-3}$ m^2/s and $K_3 = 1.6 \times 10^{-2}$ m^2/s. Three dimensional velocities are obtained from Equations 2.16 and 2.17.

6

Conclusion

In the second chapter of this thesis, I investigate the theoretical response of an elongated bay to periodic wind stress. I assume that the water is well-mixed and that the eddy viscosity is constant. The wind is spatially uniform and blows in the along-bay direction. Assuming the bay is deeper than the Ekman depth, I describe the dependence of the solution on one of the non-dimensional numbers of this problem, namely the ratio of the wind forcing frequency to the Coriolis frequency. At low frequencies, the response is quasi-steady, modulated in time by the oscillations of wind stress. The cross-bay/cross-wind currents are to the right of the wind at the surface and in the opposite direction at depth, driven by a downwind increase of sea level. Along-bay currents are downwind on the shallow sides and upwind at depth. The decrease of this along-bay circulation for frequencies larger than the non-dimensional Ekman depth δ_E defines the domain of validity of the quasi-steady response. Around the inertial frequency, currents are amplified, two layer like and rotate in the clockwise direction with time. The wind driven response decreases at super-inertial frequencies and the direct effect of the wind stress is confined to a thin near-surface layer.

Chapter 3 deals with BC winter time observations in the sub-inertial frequency band. The primary goal is to extract the wind driven response. The

along-bay difference of sea level is well-correlated with the wind stress. On shallow sides, downwind currents are observed in all deployments. In deeper locations, the along-bay current response predicted by theory is never observed. Possible explanations are larger values of the eddy viscosity, low signal-to-noise ratios, or short length of the wind stress events compared to the spin up time of the along-bay circulation. Wind driven across-bay currents are successfully observed during deployment 3, a restratifying period of time. I speculate that the failure to observe such currents during deployment 1 is due to larger values of mixing by cold and strong winds at that time. In both deployments, the bulk of the observed sub-inertial currents is poorly understood. Depth averaged momentum balances are computed for both time periods in order to remediate this issue. This reveals the importance of baroclinic pressure gradients and nonlinearities. During deployment 3, the sub-inertial currents are largely dominated by a counter-clockwise horizontal circulation. An east-to-west mean decrease of density is sometimes observed and shown to be in thermal balance with the sub-inertial flow along the eastern side of the bay.

Winds are diurnally modulated inside BC. Because the Coriolis frequency is close to the diurnal one, an inertial response of the type described in chapter 2 is possible. Chapter 4 demonstrates that this is the case. During deployment 3, the currents are two-layer like with maximum values of 5 cm/s, and rotate in the clockwise direction with time. Hodographs of the wind driven current compare well with theoretical predictions. Depth averaged and local momentum balances are computed and shed light on the importance of lateral baroclinic pressure gradients. Across-bay oscillations of density are extracted with an EOF analysis. They are significantly correlated with diurnal oscillations of across-bay currents during the second part of the deployment 3 time period, when the bay is most stratified. During the first half of deployment 3, these oscillations of density are weaker and I conclude that the response is similar to the predictions of the theoretical model at that time.

BC's response to sea level fluctuations at its mouth is the subject of chapter 5. The sea levels at each end of the bay are compared in the frequency domain. Around 5 cpd, an amplification of the sea level at BC's closed end is identified as the quarter wavelength resonance of the bay. The peak frequency of the amplification is well modeled theoretically by assuming BC is made of two interconnected basins. Along-bay currents driven by sea level fluctuations at the mouth are extracted and fit theoretical predictions. Across-bay currents are weakly coherent with sea level fluctuations in the diurnal and semi-diurnal bands. Comparison with theory fails in the across-bay direction. In both along- and across-bay directions, diurnal and semi-diurnal band signals are contaminated by larger noise levels, presumably due to the effect of the wind.

References

Allen, J. S., and Newberger, P. A., 1996: Downwelling circulation on the Oregon continental shelf. Part I: Response to idealized forcing. *J. Phys. Oceanogr.*, **26**, 2011–2035.

Allen, J. S., Newberger, P. A., and Federiuk, J., 1995: Upwelling circulation on the Oregon continental shelf. Part I: Response to idealized forcing. *J. Phys. Oceanogr.*, **25**, 1843–1866.

Antenucci, J. P., Imberger, J., and Saggio, A., 2000: Seasonal evolution of the basin-scale internal wave field in a large stratified lake. *Limnol. Oceanogr.*, **45**(7), 1621–1638.

Austin, J. A., and Lentz, S. J., 2002: The inner shelf response to wind-driven upwelling and downwelling. *J. Phys. Oceanogr.*, **32**, 2171–2193.

Badan-Dangon, A., Dorman, C. D., Merrifield, M. A., and Winant, C. D., 1991: The lower atmosphere over the Gulf of California. *J. Geophys. Res.*, **96**(C9), 16,877–16,896.

Ball, F., 1965: Second-class motions of a shallow liquid. *Journal of Fluid Mechanics*, **23**(3), 545–561.

Bendat, J. S., and Piersol, A. G., 2000: *Random Data: Analysis and Measurement Procedures*. Wiley series in probability and statistics. Wiley-Interscience, 3rd edition.

Birchfield, G. E., 1969: Response of a circular model great lake to a suddenly imposed wind stress. *J. Geophys. Res.*, **74**(23), 5547–5554.

Birchfield, G. E., and Hickie, B. P., 1977: The time-dependent response of a circular basin of variable depth to a wind stress. *J. Phys. Oceanogr.*, **7**(5), 691–701.

Bowen, A. J., Inman, D. L., and Simmons, V. P., 1968: Wave "set-down" and set-up. *J. Geophys. Res.*, **73**(8), 2569–2577.

Buijsman, M. C., and Ridderinkhof, H., 2008: Variability of secondary currents in a weakly stratified tidal inlet with low curvature. *Cont. Shelf Res.*, **28**, 1711–1723.

Caliskan, H., and Valle-Levinson, A., 2008: Wind-wave transformations in an elongated bay. *Cont. Shelf Res.*, **28**, 1702–1710.

Canar, N., Margarita, A., Garcia, P., and Ricardo, J., 2008: Grazing by microzooplankton in Concepcion Bay, Gulf of California, Mexico. *Hidrobiologica*, **18**(1), 141–151.

Chant, R., 2002: Secondary circulation in a region of flow curvature: Relationship with tidal forcing and river discharge. *J. Geophys. Res.*, **107**(C9).

Chant, R. J., 2001: Evolution of near-inertial waves during an upwelling event on the new jersey inner shelf. *J. Phys. Oceanogr.*, **31**, 746–764.

Cheng, P., Valle-Levinson, A., Winant, C. D., Ponte, A. L. S., Gutiérrez de Velasco, G., and Winters, K. B., 2010: Upwelling-enhanced seasonal stratification in a semiarid bay. *J. Geophys. Res.*, **in preparation**.

Chereskin, T. C., 1995: Direct evidence for an Ekman balance in the California Current. *J. Geophys. Res.*, **100**(C9), 18261–18269.

Craig, P. D., 1989a: Constant-eddy-viscosity models of vertical structure forced by periodic winds. *Cont. Shelf Res.*, **9**(4), 343–358.

Craig, P. D., 1989b: A model of diurnally forced vertical current structure near 30^o latitude. *Cont. Shelf Res.*, **9**(11), 965–980.

Csanady, G. T., 1968a: Motions in a model great lake due to a suddenly imposed wind. *J. Geophys. Res.*, **73**, 6435–6447.

Csanady, G. T., 1968b: Wind-driven summer circulation in the great lakes. *J. Geophys. Res.*, **73**, 2579–2589.

Csanady, G. T., 1973: Wind-induced barotropic motions in long lakes. *J. Phys. Oceanogr.*, **3**, 429–438.

Csanady, G. T., 1982: *Circulation In The Coastal Ocean*. Environmental fluid mechanics. D. Reidel.

D'Asaro, E. A., Eriksen, C. C., Levine, M. D., Niiler, P., Paulson, C. A., and Meurs, P. V., 1995: Upper-ocean inertial currents forced by a strong storm. Part I: Data and comparisons with linear theory. *J. Phys. Oceanogr.*, **25**, 2909–2936.

Davis, R. E., 1985: Drifter observations of coastal surface currents during CODE: The method and descriptive view. *J. Geophys. Res.*, **90(C3)**, 4741–4755.

Davis, R. E., de Szoeke, R., Halpern, D., and Niiler, P., 1981a: Variability in the upper ocean during MILE. Part I: The heat and momentum balances. *Deep-Sea Research*, **28**, 1427–1452.

Davis, R. E., de Szoeke, R., Halpern, D., and Niiler, P., 1981b: Variability in the upper ocean during MILE. Part II: Modelling the mixed layer response. *Deep-Sea Research*, **28**, 1453–1475.

Defant, A., 1961a: *Physical Oceanography*, volume 2. Pergamon, Tarrytown, N.Y.

Defant, A., 1961b: *Physical Oceanography*, volume 1. Pergamon, Tarrytown, N.Y.

Ekman, V., 1905: On the influence of the earth's rotation on ocean-currents. *Arkiv For Matematik, Astronomi Och Fysik*, **2**, 1–52.

Emery, W. J., and Thomson, R. E., 2001: *Data analysis methods in physical oceanography*. Elsevier, Amsterdam, 2nd edition.

Fewings, M., Lentz, S. J., and Fredericks, J., 2008: Observations of cross-shelf flow driven by cross-shelf winds on the inner continental shelf. *J. Phys. Oceanogr.*, **38**, 2358–2378.

Filloux, J. H., 1973: Tidal patterns and energy balance in the Gulf of California. *Nature*, **243**, 217–221.

Fischer, H. B., 1973: Longitudinal dispersion and turbulent mixing in open-channel flow. *Annual Review of Fluid Mechanics*, **5**, 59–78.

Fong, D. A., and Geyer, W. R., 2002: The alongshore transport of freshwater in a surface-trapped river plume. *J. Phys. Oceanogr.*, **32**, 957–972.

Garrett, C., 1975: Tides in gulfs. *Deep Sea Research*, **22**(1), 23–35.

Garrett, C., and Petrie, B., 1981: Dynamical aspects of the flow through the Strait of Belle Isle. *J. Phys. Oceanogr.*, **11**, 376–393.

Garvine, R. W., 2004: The vertical structure and subtidal dynamics of the inner shelf off new jersey. *Journal of Marine Research*, **62**, 337–371.

Geyer, W. R., Trowbridge, J. H., and Bowen, M. M., 2000: The dynamics of a partially mixed estuary. *J. Phys. Oceanogr.*, **30**, 2035–2048.

Gill, A. E., 1982: *Atmosphere-Ocean Dynamics*. Academic Press, San Diego.

Godin, G., 1993: On tidal resonance. *Cont. Shelf Res.*, **13**(1), 89–107.

Greenspan, H. P., and Horward, L. N., 1963: On a time-dependent motion of a rotating fluid. *Journal of Fluid Mechanics*, **17**(3), 385–404.

Gutiérrez de Velasco, G., and Winant, C. D., 2004: Wind- and density-driven circulation in a well-mixed inverse estuary. *J. Phys. Oceanogr.*, **34**, 1103–1116.

Hendershott, M. C., and Speranza, A., 1971: Co-oscillating tides in long, narrow bays; the Taylor problem revisited. *Deep Sea Research*, **18**, 959–980.

Hickey, B. M., 1998: *Coastal oceanography of western North America from the tip of Baja California to Vancouver Island*, volume 11 of *The Sea*. John Wiley.

Huang, J. C. K., and Saylor, J. H., 1982: Vorticity waves in a shallow basin. *Dynamics of Atmospheres and Oceans*, **6**, 177–196.

Hunter, J. R., and Hearn, C. J., 1987: Lateral and vertical variations in the wind-driven circulation in long, shallow lakes. *J. Geophys. Res.*, **92**(C12), 13,106–13,114.

Ianniello, J. P., 1977: Tidally induced residual currents in estuaries of constant breadth and depth. *J. Mar. Res.*, **35**, 755–786.

Jacobs, G. A., Book, J. W., Perkins, H. T., and Teague, W. J., 2001: Inertial oscillations in the Korea Strait. *J. Geophys. Res.*, **106**(C11), 26943–26957.

Janzen, C. D., and Wong, K. C., 2002: Wind-forced dynamics at the estuary-shelf interface of a large coastal plain estuary. *J. Geophys. Res.*, **107**(C10), 3138.

Johnson, M., and Ledesma-Vásquez, J., 2001: Pliocene-Pleistocene rocky shorelines trace coastal development of Bahía Concepción, gulf coast of Baja California Sur (Mexico). *Palaeogeogr., Palaeoclimateol., Palaeoecol.*, **166**, 65–88.

Kirincich, A. R., and Barth, J. A., 2009: Time-varying across-shelf ekman transport and vertical eddy viscosity on the inner shelf. *J. Phys. Oceanogr.*, **39**, 602–620.

Kirincich, A. R., Barth, J. A., Grantham, B. A., Menge, B. A., and Lubchenco, J., 2005: Wind-driven inner-shelf circulation off central oregon during summer. *J. Geophys. Res.*, **110**.

Kundu, P. K., 1976: An analysis of inertial oscillations observed near Oregon coast. *J. Phys. Oceanogr.*, **6**, 879–893.

Kundu, P. K., Chao, S., and McCreary, J. P., 1983: Transient coastal currents and inertio-gravity waves. *Deep-Sea Research*, **30**(10A), 1059–1082.

Kunze, E., 1985: Near-inertial wave propagation in geostrophic shear. *J. Phys. Oceanogr.*, **15**, 544–565.

Lamb, H., 1932: *Hydrodynamics*. Cambridge Univ. Press, New York, N.Y., 6th edition.

Large, W. G., and Pond, S., 1981: Open ocean momentum flux measurements in moderate to strong winds. *J. Phys. Oceanogr.*, **11**, 324–336.

Lechuga-Deveze, C., Reyes-Salinas, A., and Morquecho-Escamilla, M., 2001: Anoxia in a coastal bay: case study of a seasonal event. *Rev. biol. trop.*, **49**(2), 525–534.

Lentz, S., Guza, R., Elgar, S., Feddersen, F., and Herbers, T., 1999: Momentum balances on the North Carolina inner shelf. *J. Geophys. Res.*, **104**(C8), 18,205–18,226.

Lentz, S. J., 1994: Current dynamics over the northern California inner shelf. *J. Phys. Oceanogr.*, **24**, 2461–2478.

Lentz, S. J., 2001: The influence of stratification on the wind-driven cross-shelf circulation over the North Carolina shelf. *J. Phys. Oceanogr.*, **31**, 2749–2760.

Lerczak, J. A., and Geyer, W. R., 2004: Modeling the lateral circulation in straight stratified estuaries. *J. Phys. Oceanogr.*, **34**, 1410–1428.

Lerczak, J. A., Hendershott, M. C., and Winant, C. D., 2001: Observations and modeling of coastal internal waves driven by a diurnal sea breeze. *J. Geophys. Res.*, **106**(C9), 19715–19729.

Lopez-Cortes, D., Garate-Lizarraga, J. B.-G. I., Hernandez-Sandoval, F., and Murillo-Murillo, I., 2003: Phytoplankton biomasses and hydrographic conditions during El Niño 1997-1998 in Bahía Concepción, Gulf of California,M'exico. *Geofísica Internacional*, **42**, 495–504.

MacKinnon, J. A., and Gregg, M. C., 2005: Near-inertial waves on the new england shelf: The role of evolving stratification, turbulent dissipation, and bottom drag. *J. Phys. Oceanogr.*, **35**, 2408–2424.

Madsen, O. S., 1977: A realistic model of the wind-induced Ekman boundary layer. *J. Phys. Oceanogr.*, **7**, 248–255.

Mathieu, P. P., Deleersnijder, E., Cushman-Roisin, B., Beckers, J. M., and Bolding, K., 2002: The role of topography in small well-mixed bays, with application to the lagoon of Mururoa. *Cont. Shelf Res.*, **22**, 1379–1395.

McFall, C., 1968: Reconnaissance geology of the Concepcion bay area, Baja California, Mexico. *Stanford University Publications, Geological Society*, **10**(5), 1–25.

McWilliams, J. C., and Huckle, E., 2006: Ekman layer rectification. *J. Phys. Oceanogr.*, **36**(1646-1659).

Mei, C. C., 1989: *The applied dynamics of ocean surface waves*, volume 1 of *Advanced Series on Ocean Engineering*. World Scientific.

Mendoza-Salgado, R., Lechuga-Deveze, C., and Ortega-Rubio, A., 2006: Influence of rainfall on a subtropical arid zone coastal system. *Journal of Arid Environments*, **66**, 247–256.

Merrifield, M. A., and Winant, C. D., 1989: Shelf circulation in the Gulf of California: A description of the variability. *J. Geophys. Res.*, **94**(C12), 18133–18160.

Miles, J., 1985: Surface waves in basins of variable depth. *Journal of Fluid Mechanics*, **152**, 379–389.

Millot, C., and Crepon, M., 1981: Inertial oscillations on the continental shelf of the Gulf of Lions - observations and theory. *J. Phys. Oceanogr.*, **11**, 639–657.

Mitchum, G. T., and Clarke, A. J., 1986: The frictional nearshore response to forcing by synoptic scale winds. *J. Phys. Oceanogr.*, **16**, 934–946.

Mohammed-Zaki, M. A., 1980: Time scales in wind-driven lake circulations. *J. Geophys. Res.*, **85**(C3), 1553–1562.

Morales, R. A., and Gutiérrez, G., 1989: Mareas en el Golfo de California. *Geofísica Internacional*, **28**(1), 25–46.

Munchow, A., and Garvine, R. W., 1993: Dynamical properties of a buoyancy-driven coastal current. *J. Geophys. Res.*, **98**(C11), 20063–20077.

Narváez, D. A., and Valle-Levinson, A., 2008: Transverse structure of wind-driven flow at the entrance to an estuary: Nansemond river. *J. Geophys. Res.*, **113**.

Nunes-Vaz, R. A., Lennon, G. W., and Bowers, D. G., 1990: Physical behaviour of a large, negative or inverse estuary. *Cont. Shelf Res.*, **10**(3), 277–304.

Obeso-Nieblas, M., Alatorre, M., and Jiménez, I., 1996: Modelación de la marea en Bahía Concepción, B.C.S. , México. *Oceánides*, **11**, 1–8.

Orlic, M., 1987: Oscillations of the inertia period on the Adriatic Sea shelf. *Cont. Shelf Res.*, **7**(6), 577–598.

Palomares-Garci, R., Bustillos-Guzman, J., and Lopez-Cortes, D., 2006: Pigment-specific rates of phytoplankton growth and microzooplankton grazing in a subtropical lagoon. *Journal of Plankton Research*, **28**(12), 1217–1232.

Pawlowicz, R., Beardsley, B., and Lentz, S., 2002: Classical tidal harmonic analysis including error estimatees in MATLAB using T_TIDE. *Computers & Geosciences*, **28**, 929–937.

Pedlosky, J., 1987: *Geophysical Fluid Dynamics*. Springer-Verlag, 2nd edition.

Phillips, O. M., 1966: On turbulent convection currents and the circulation of the red sea. *Deep-Sea Research*, **13**, 1148–1160.

Pollard, R. T., 1970: On the generation by winds of inertial waves in the ocean. *Deep-Sea Research*, **17**, 795–812.

Pollard, R. T., and Millard, R. C., 1970: Comparison between observed and simulated wind-generated inertial oscillations. *Deep-Sea Res.*, **17**, 813–821.

Polton, J. A., Lewis, D. M., and Belcher, S. E., 2005: The role of wave-induced Coriolis–Stokes forcing on the wind-driven mixed layer. *J. Phys. Oceanogr.*, **35**, 444–457.

Price, J. F., and Sundermeyer, M. A., 1999: Stratified Ekman layers. *J. Geophys. Res.*, **104**(C9), 20467–20494.

Price, J. F., Weller, R. A., and Schudlich, R. R., 1987: Wind-driven ocean currents and ekman transport. *Science*, **238**, 1534–1538.

Rabinovich, A. B., and Monserrat, S., 1996: Meteorological tsunamis near the Balearic and Kuril islands: Descriptive and statistical analysis. *Natural Hazards*, **13**, 55–90.

Rao, D. B., 1976: Two dimensional normal modes in arbitrary enclosed basins on a rotating earth: Application to lake ontario and superior. *Phil. Trans. R. Soc. (A)*, **281**, 63–96.

Rippeth, T. P., Simpson, J. H., Player, R. J., and Garcia, M., 2002: Current oscillations in the diurnal-inertial band on the catalonian shelf in spring. *Cont. Shelf Res.*, **22**, 247–265.

Rudnick, D. L., 2003: Observations of momentum transfer in the upper ocean: Did ekman get it right? In *Proceedings of the 13th 'Aha Huliko'a Hawaiian Winter Workshop*.

Sanay, R., and Valle-Levinson, A., 2005: Wind-induced circulation in semienclosed homogeneous, rotating basins. *J. Phys. Oceanogr.*, **35**, 2520–2531.

Satake, K., and Shimazaki, K., 1988: Free oscillation of the japan sea excited by earthquakes - II. Modal approach and synthetic tsunamis. *Geophysical Journal*, **93**, 457–463.

Saylor, J. H., Huang, J. C. K., and Reid, R. O., 1980: Vortex modes in southern lake Michigan. *J. Phys. Oceanogr.*, **10**, 1814–1823.

Scully, M. E., Geyer, W. R., and Lerczak, J. A., 2009: The influence of lateral advection on the residual estuarine circulation: A numerical modeling study of the Hudson river estuary. *J. Phys. Oceanogr.*, **39**, 107–124.

Shearman, R. K., 2005: Observations of near-inertial current variability on the New England shelf. *J. Geophys. Res.*, **110**.

Simpson, J. H., 2002: Forced oscillations near the critical latitude for diurnal-inertial resonance. *J. Phys. Oceanogr.*, **32**, 177–187.

Smith, R. L., 1995: *The physical processes of coastal ocean upwelling systems.* Upwelling and the Ocean: Modern Processes and Ancient Records. John Wiley.

Sobarzo, M., Shearman, R. K., and Lentz, S., 2007: Near-inertial motions over the continental shelf off Concepcón, central Chile. *Progress in Oceanography*, **75**, 348–362.

Stevens, C. L., and Lawrence, G. A., 1997: Estimation of wind-forced internal seiche amplitudes in lakes and reservoirs, with data from British Columbia, Canada. *Aquatic Sciences*, **59**, 115–134.

Stocker, T., and Hutter, K., 1987: *Topographic waves in channels and lakes on the f-plane*, volume 21. Springer-Verlag.

Taylor, G. I., 1921: Tides in gulfs and rectangular basins. *Proc. Lond. Math. Soc.*, **20**, 148–181.

Tilburg, C. E., 2003: Across-shelf transport on a continental shelf: Do across-shelf winds matter? *J. Phys. Oceanogr.*, **33**, 2675–2688.

Tragou, E., and Garrett, C., 1997: The shallow thermohaline circulation of the red sea. *Deep Sea Research I*, **44**(8), 1355–1376.

Van Dorn, W. G., 1987: Tide gage response to tsunamis. Part II: Other oceans and smaller seas. *J. Phys. Oceanogr.*, **17**, 1507–1516.

Vennell, R., 2007: Long barotropic waves generated by a storm crossing topography. *J. Phys. Oceanogr.*, **37**, 2809–2823.

von Storch, H., and Zwiers, F. W., 1999: *Statistical Analysis in Climate Research.* Cambridge Univ. Press.

Webster, F., 1968: Observations of inertial-period motions in the deep sea. *Reviews of Geophysics*, **6**(4), 473–490.

Weisberg, R. H., 1976: The nontidal flow in the Providence river of Narragansett bay: A stochastic approach to estuarine circulation. *J. Phys. Oceanogr.*, **6**, 721–734.

Weisberg, R. H., and Sturges, W., 1976: Velocity observations in the West passage of Narragansett bay: A partially mixed estuary. *J. Phys. Oceanogr.*, **6**, 345–354.

Weller, R. A., Rudnick, D. L., Eriksen, C. C., Polzin, K. L., Oakey, N. S., Toole, J. W., Schmitt, R. W., and Pollard, R. T., 1991: Forced ocean response during the frontal air-sea interaction experiment. *J. Geophys. Res.*, **96**(C5), 8611–8638.

Winant, C. D., 2004: Three dimensional wind-driven flow in a linear, constant density, rotating basin. *J. Phys. Oceanogr.*, **34**, 462–476.

Winant, C. D., 2006: Three-dimensional wind-driven coastal circulation past a headland. *J. Phys. Oceanogr.*, **36**(7), 1430–1438.

Winant, C. D., 2007: Three-dimensional tidal flow in an elongated, rotating basin. *J. Phys. Oceanogr.*, **37**, 2345–2362.

Winant, C. D., and Gutiérrez de Velasco, G., 2003: Tidal dynamics and residual circulation in a well mixed inverse estuary. *J. Phys. Oceanogr.*, **33**, 1365–1379.

Wong, K. C., 1994: On the nature of transverse variability in a coastal plain estuary. *J. Geophys. Res.*, **99**(C7), 14,209–14,222.

Wong, K. C., and Moses-Hall, J. E., 1998: On the relative importance of the remote and local wind effects to the subtidal variability in a coastal plain estuary. *J. Geophys. Res.*, **103**(C9), 18393–18404.

Yankovsky, A. E., 2006: On the validity of the thermal wind balance in alongshelf currents off the New Jersey coast. *Cont. Shelf Res.*, **26**, 1171–1183.

Yankovsky, A. E., and Chapman, D. C., 1997: A simple theory for the fate of buoyant coastal discharges. *J. Phys. Oceanogr.*, **27**, 1386–1401.

Young, W. R., and Ben Jelloul, M., 1997: Propagation of near-inertial oscillations through a geostrophic flow. *Journal of Marine Research*, **55**, 735–766.

Zikanov, O., Slinn, D. N., and Dhanak, M. R., 2003: Large-eddy simulations of the wind-induced turbulent Ekman layer. *Journal of Fluid Mechanics*, **495**, 343–368.